ADVANCED FUNCTIONAL MATERIALS
www.afm-journal.de

Challenges and Opportunities for Proton Batteries: From Electrodes, Electrolytes to Full-Cell Applications

Sicheng Wu, Haocheng Guo, and Chuan Zhao**

Proton batteries have emerged as a promising solution for grid-scale energy storage benefiting their high safety and abundant raw materials. The battery chemistry based on proton-ions is intrinsically advantageous in integrating fast diffusion kinetics and high capacities, thus offering great potential to break through the energy limit of capacitors and the power limit of traditional batteries. Significant efforts have been dedicated to advancing proton batteries, leading to successive milestones in recent years. Herein, the recent progress of proton batteries is summarized and insights into the challenges in electrodes, electrolytes and future opportunities for enhancing full-cell applications are provided. The fundamentals of electrochemical proton storage and representative faradaic electrodes are discussed, delving into their current limitations in mechanism studies and electrochemical performances. Subsequently, the classification, challenges, and strategies for improving protonic electrolytes are addressed. Finally, the state-of-the-art proton full-cells are explored, and views on the rational design of proton battery devices for achieving high-performance aqueous energy storage are offered.

1. Introduction

The development of intermittent renewable energies necessitates advanced energy storage devices with high-rate performance and energy efficiency for grid connection. Despite the current dominance of lithium-ion batteries (LIBs), aqueous batteries offer compelling advantages for grid-scale applications such as high safety, environmental friendliness, superior rate capability, and low cost. Alongside Li^+,[1] various other ion-charge-carriers (Na^+, K^+, Zn^{2+}, Mg^{2+}, Ca^{2+}, and Al^{3+}) have been explored in aqueous batteries.[2–4] Nevertheless, their increasing ionic radii and weight intrinsically impede battery kinetics and limit electrode choices. Alternatively, the potential use of proton charge carriers has been reported for co-insertion with metal cations in certain hosts.[5,6] This concept has been further validated in the recently discovered proton insertion electrodes.[7–9] Consequently, proton batteries using naked proton and/or hydronium ions as the charge carriers have recently attracted significant research attention.[10]

Proton offers distinct advantages over metal-ion charge carriers as illustrated in **Figure 1**a,b. First, hydrogen's high average elemental abundance (≈1500 ppm) in the earth's crust surpasses that of Li (≈17 ppm) and Zn (≈79 ppm), ensuring the affordability and sustainability of proton batteries.[11] Second, with the smallest ionic size (at the femtometer level), protons are theoretically better suited for insertion into host electrode materials, facilitating stable cycling with minimal structural expansion.[12] Third, the lowest atomic mass of protons (1.01 g mol^{-1}) enables more ion charge carriers in the same mass of electrolytes, alleviating mass burdens on charged electrode materials. Additionally, proton transfer in aqueous electrolytes could proceed by breaking and forming H-bonds with adjacent oxygen atoms in a network of water molecules (Grotthuss mechanism, Figure 1b), resulting in extremely high ionic conductivity (e.g. ≈ 1 S cm^{-1} for 4 M H_2SO_4[13]).

As shown in Figure 1c, the recent development of proton battery chemistry began with the prediction of faradaic electrodes in 2008.[14] This was then achieved in 2016 by electrodes of quinone molecules and a rocking-chair proton battery was showcased.[15] Shortly thereafter, broader applicability of quinones was established (2017), leading to an electrolytic proton battery.[16] Subsequent reports reveal other kinds of faradaic electrodes and surprising properties, such as hydrogen bronzes (2018)[17] and Prussian blue analogues (PBA, 2019).[18] The characteristic diffusion-free Grotthuss proton conduction was demonstrated also to apply in solid-state through percolating crystal-water channels in inorganic electrodes[18,19] or an intermolecular hydrogen-bond network in organic electrodes.[20] However, challenges related to fast cycling decay and electrochemical dissolutions in aqueous acids were often observed in most known electrodes, possibly due to the co-interaction of solvent-water molecules during the proton desolvation process.[17] A series of electrolyte innovations were accordingly initiated aiming to regulate the

S. Wu, H. Guo[+], C. Zhao
School of Chemistry
Faculty of Science
University of New South Wales
Sydney, NSW 2052, Australia
E-mail: haocheng.guo@kit.edu; chuan.zhao@unsw.edu.au

The ORCID identification number(s) for the author(s) of this article can be found under https://doi.org/10.1002/adfm.202405401

[+]Present address: Helmholtz Institut Ulm, Karlsruher Institut für Technologie, 89081 Ulm, Germany

© 2024 The Author(s). Advanced Functional Materials published by Wiley-VCH GmbH. This is an open access article under the terms of the Creative Commons Attribution-NonCommercial License, which permits use, distribution and reproduction in any medium, provided the original work is properly cited and is not used for commercial purposes.

DOI: 10.1002/adfm.202405401

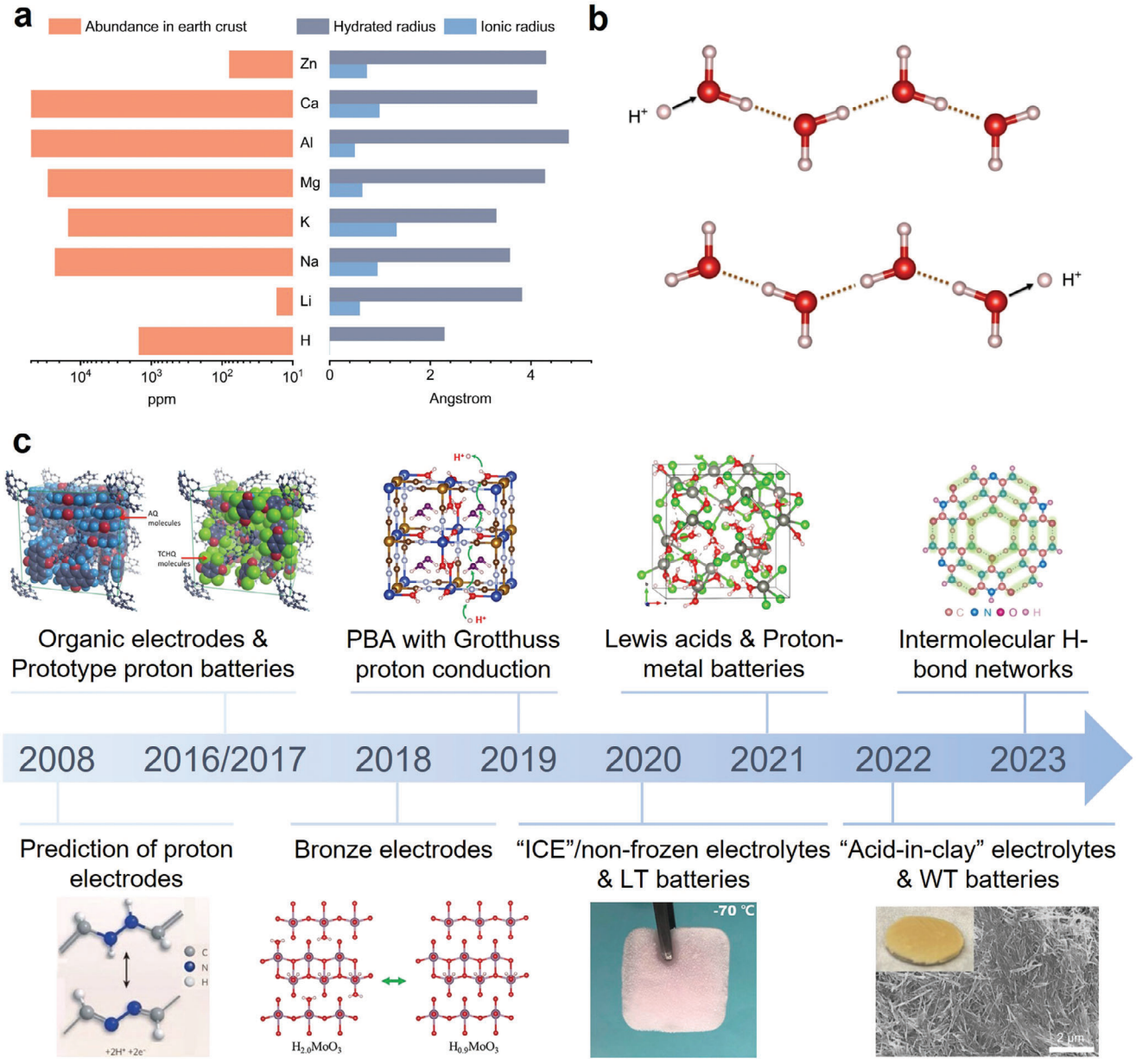

Figure 1. The characteristics of proton compared to other metal-ion charge carriers and the development route of aqueous proton batteries. a) Comparison of abundance in the crust, ionic radii and hydrated radii for typical charge carriers. b) Schematic of Grotthuss proton conduction.[18] c) A development timeline of aqueous proton batteries. Reproduced with permission.[12,14,15,20,23,25,29,30]

proton solvation and/or restrain free-water activities, e.g., introducing solvation-competing additives,[21,22] and altering electrolyte physical states.[23] Meanwhile, special electrolyte characteristics were also identified which facilitate low-temperature (LT) applications (2020), such that non-frozen concentrated H_3PO_4 electrolytes at −78 °C,[24] and solid-state ice electrolytes at −70 °C.[25] More widened temperature (WT) was further achieved via electrolyte designs, and a "acid-in-clay" electrolyte reached decent proton conductivity at −82 °C,[23] while a solvent-free protic liquid enabled battery function up to 250 °C.[26] Lewis acids (e.g., $ZnCl_2$,[27] $AlCl_3$[28]) were also introduced as electrolytes promoting new designs of proton-metal batteries. Despite the renaissance, proton batteries remain in their infancy. Further research and development are essential to advance the battery chemistry and bring proton batteries closer to real application viability.

This review aims to offer a timely overview of proton electrodes, electrolytes, and their full-cell applications by summarizing advances and highlighting the challenges and opportunities in this field. The fundamentals of electrochemical proton storage and typical faradaic electrodes are discussed with critical assessments of their limitations in mechanism studies and performances. In particular, we provide a systematic review of the protonic electrolytes and associated full-cell configurations, which are crucial toward device applications but have received less

© 2024 The Author(s). Advanced Functional Materials published by Wiley-VCH GmbH

16163028, 2024, 40, Downloaded from https://onlinelibrary.wiley.com/doi/10.1002/adfm.202405401 by Karlsruher Institut F., Wiley Online Library on [05/11/2024]. See the Terms and Conditions (https://onlinelibrary.wiley.com/terms-and-conditions) on Wiley Online Library for rules of use; OA articles are governed by the applicable Creative Commons License

attention in previous publications.[31–34] Protonic electrolytes are categorized based on their proton sources and physical status, and current challenges are analyzed leading to the propose of possible improvement strategies. Further, application opportunities of proton batteries are highlighted in terms of two types of cell designs. We also share our perspectives on the rational design of proton batteries, with the hope that the insights will pave the way for future advancements in this field.

2. Faradaic Proton Electrodes

In contrast to a non-faradaic electrode which relies on ion adsorption for charge compensation, a faradaic electrode is characterized by a faradaic process with charge transfer. This process involves the exchange of electrons between the electrode and the electrolyte ions, leading to a redox reaction associated with substantial charge storage compared to that contributed by merely ion adsorption. Developing high-performance proton electrodes and understanding their energy storage mechanisms have been considered as the main challenges for advancing proton batteries.

2.1. Testing Configuration for Electrode Evaluations

Unlike research on alkaline metal-ion batteries where coin-cells are commonly adopted, there are no standardized devices for electrode evaluation in proton batteries. Various cells inevitably deliver different electrochemical results. Stainless steel coin cells suffer from (electrochemical) corrosion in proton batteries, limiting their applicability only to mild acidic systems (e.g. the hybrid-type proton-metal batteries). Additionally, the two-electrode cell configuration can cause inaccuracies when evaluating the working electrodes. For example, the electrochemical impedance spectroscopy (EIS) results of working electrodes can be masked by the resistance of counter electrodes.[35] Therefore, to better reflect the intrinsic electrochemical properties of the electrode, it is always recommended to evaluate proton electrodes via a three-electrode cell, such as a vial/beaker cell or a Swagelok cell (**Figure 2a**).

In vial/beaker-cells, carbon-based or titanium-based substrates are often adopted to load active materials and serve as the working electrode, and an oversized counter electrode based on carbon materials (e.g., graphite, activated carbon) is recommended in acidic environments. There are normally excess amounts of electrolytes ranging from several mL to tens of mL, which avoids the potential concern of electrolyte depletion and is advantageous for long-term cycling. Furthermore, adopting beaker-cells allows direct observation of (side) reactions on both working and counter electrodes. Consequently, many interesting/important phenomena have been identified, such as material electrochemical dissolution,[17,26,36] gas evolution,[12,23] and detachments of electrolytic products and colloid formation.[37]

By contrast, Swagelok-cells enable a lean electrolyte environment (from tens of µL to several hundred µL), and offer a more compact configuration ensuring tight contact between electrodes. These features introduce several advantages. First, the tight contact can effectively reduce electrical resistance, which is particularly beneficial for evaluating electrodes with inferior electronic conductivity, such as organic electrodes. Second, the minimized electrolyte usage facilitates the exploration of novel functional electrolytes, which may contain sensitive components, such as expensive, air-sensitive or toxic agents, low-yield ionic liquids, etc. Furthermore, the physical contact between electrodes and separator can help mitigate the detachment of coated electrodes (accumulated hydrogen evolution can gradually peel-off the coating) or certain electrolytic products from the current collectors.[38]

2.2. Electrode Reaction Mechanisms

There are generally three main reaction mechanisms for various faradaic proton storage electrodes, i.e. surface redox reactions, intercalation reactions, and electrolytic reactions, which show distinctive cyclic voltammetry (CV) responses. Typical processes and corresponding CV profiles of these reactions are illustrated in Figure 2b,c. (*i*) Surface redox, also known as redox pseudocapacitance, represents a distinct charge storage mechanism that ions are electrochemically adsorbed at and bonded to the surface or near-surface lattice of materials, presenting quasi-rectangular voltammograms. The most representative electrode is the hydrous ruthenium oxides ($RuO_2{\cdot}nH_2O$).[39] Additionally, reacting with proton-ions, the 2D transition metal carbides (MXenes) are also associated with surface redox, despite there is an intercalating step. A pair of broad redox peaks is present additional to the rectangular CV profile. Thanks to the surface redox/pseudocapacitance, the amount of charge storage is increased compared to the mere ion-adsorption in double-layer capacitance but to a limited extent restricted by the reaction depth. (*ii*) Ion intercalation reaction refers to a process in which the charge carrier ions are inserted into the crystal lattice of a host material accompanied with a faradaic charge transfer. Depending on whether there is a phase transition(s), these reactions can manifest as either battery-like behavior (intercalation (B), e.g., α-MoO_3, with well-defined redox peaks) or pseudocapacitive charge storage (intercalation (P), e.g., NiFe-TBA, where the potentials of redox peaks show minimal deviations with increasing sweep rate). As the entire material lattice can participate in redox reactions, ion intercalation reactions can usually store a significant amount of charge. (*iii*) Electrolytic reaction signifies a chemical transformation occurring at the electrode under the influence of an external voltage or current. In electrolysis, one substance undergoes conversion to another through charge transfer, involving various physical states such as aqueous (aq.)/liquid (l), solid (s), and gas (g). Examples of reported electrolysis include the redox pairs of MnO_2 (s)/Mn^{2+} (aq.),[37,40] PbO_2 (s)/$PbSO_4$ (s),[16] $PbSO_4$ (s)/Pb (s),[41] H^+(aq.)/H_2 (g),[42] O_2 (g)/H_2O (l),[43] etc. As electrolysis relies mostly on electrolytes rather than solid materials, it exhibits superior overall charge storage capability compared to the other two reaction types.

2.3. Faradaic Electrodes

2.3.1. Prussian Blue/Turnbull's Blue Analogues

Prussian blue analogues (PBAs) and Turnbull's blue analogues (TBAs) belong to a cluster of open-framework metal cyanides

© 2024 The Author(s). Advanced Functional Materials published by Wiley-VCH GmbH

RIGHTSLINK

16163028, 2024, 40, Downloaded from https://onlinelibrary.wiley.com/doi/10.1002/adfm.202405401 by Karlsruher Institut F., Wiley Online Library on [05/11/2024]. See the Terms and Conditions (https://onlinelibrary.wiley.com/terms-and-conditions) on Wiley Online Library for rules of use; OA articles are governed by the applicable Creative Commons License

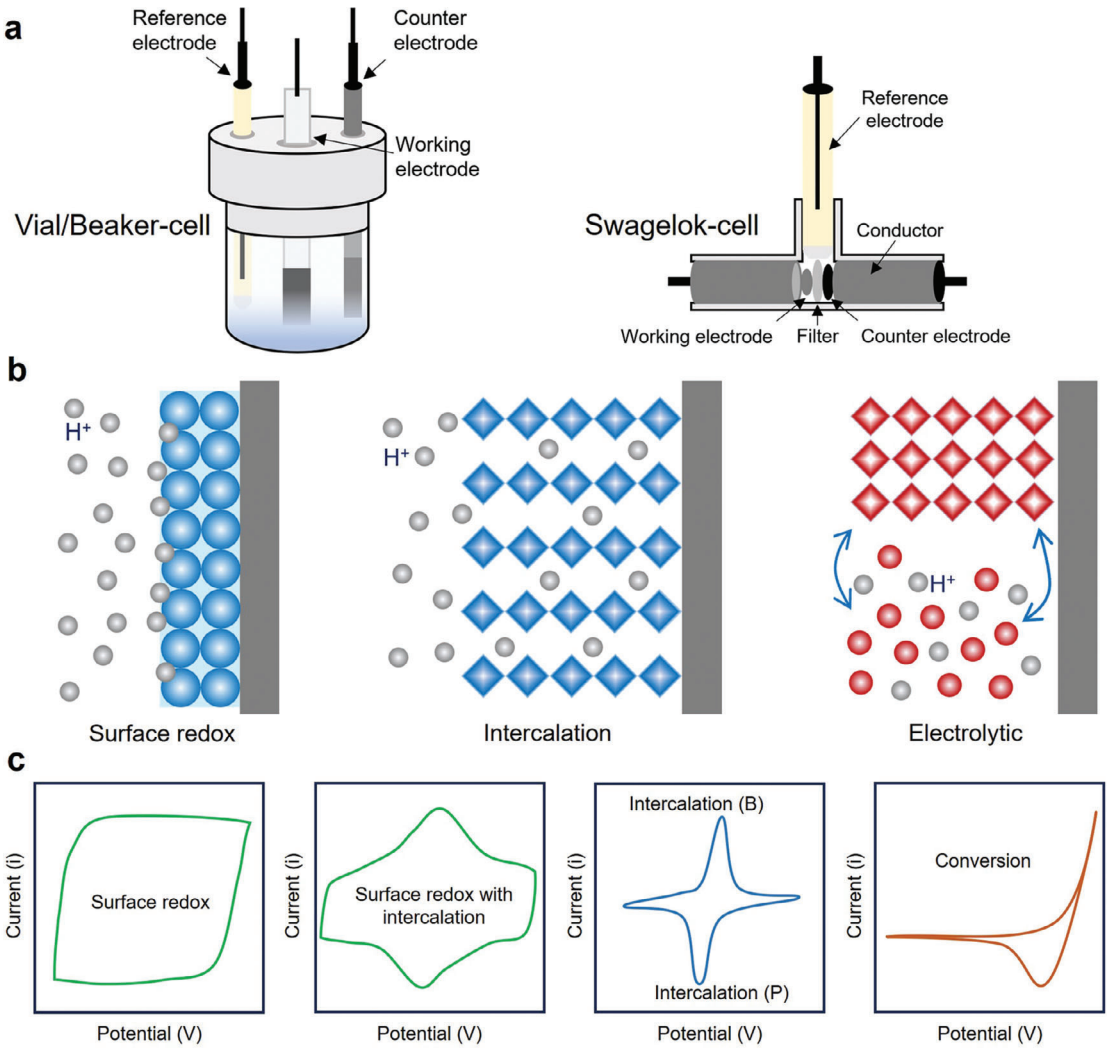

Figure 2. Schematic illustration of a) vial/beaker-cell (left) and Swagelok-cell (right), b) reaction fundaments associated in proton electrochemistry, and c) corresponding CV profiles.

with a face-centered cubic structure. The general formula of PBAs/TBAs is $A_xM[M'(CN)_6]_y{\cdot}zH_2O$, where A and M represent alkali-metal and transition-metal respectively.[44] The open framework and large void sites in the structure of PBAs/TBAs allow rapid intercalation of metal-ion charge carriers. Coupled with their facile preparation and low-cost features, PBAs/TBAs are suitable for various energy storage systems.[45,46]

Early research in 2010 has pointed out the high proton conductivity in hydrated PBAs. As shown in **Figure 3**a, the abundant lattice water and ligand water in the structure enable the rapid Grotthuss proton conduction in solid-state through contiguous H-bond networks.[47] A group of materials have been successively introduced as cathodes for aqueous proton batteries such as $Cu[Fe(CN)_6]_{0.63}{\cdot}3.4H_2O$ (CuFe-TBA)[18] and $Ni[Fe(CN)_6]_{2/3}{\cdot}3.4H_2O$ (NiFe-TBA).[29] For example, NiFe-TBA demonstrates outstanding proton storage performance. In CV measurements (Figure 3b), two pairs of highly symmetrical redox peaks with very low potential gaps were found, and the responsive currents of these peaks show almost linear relationship with increasing sweep rate ($i = av^b$), indicating predominant capacitive controlled kinetics. Accordingly, NiFe-TBA shows an excellent rate performance, achieving remarkably high rates of up to 6000 C (390 A g^{-1}) at room temperature (Figure 3c) and up to 50 C at −40 °C. When comparing with other charge carriers (Figure 3d), NiFe-TBA shows the best rate capability with proton, validating the superior kinetics resulting from the unique Grotthuss conduction. *In-situ* synchrotron XRD results in Figure 3e reveal a nearly "zero-strain" feature of NiFe-TBA, where the volume change is determined to be only 0.88% during proton (de)intercalation. Such zero-strain materials can effectively accommodate the structure variation during ion insertion/extraction and deliver impressive cycling stability.[48]

PBAs/TABs based on other skeleton metal-ion have also been successively developed as proton intercalation electrodes, including ZnFe-TBA,[36] InFe-PBA,[49] and CuCo-PBA.[50] However, most of them suffer from a limited capacity (<80 mAh^{-1}), and therefore are insufficient to match the high capacities of anode materials. To this end, a high capacity PBA based on dual redox

© 2024 The Author(s). Advanced Functional Materials published by Wiley-VCH GmbH

16163028, 2024, 40, Downloaded from https://onlinelibrary.wiley.com/doi/10.1002/adfm.202405401 by Karlsruher Institut F., Wiley Online Library on [05/11/2024]. See the Terms and Conditions (https://onlinelibrary.wiley.com/terms-and-conditions) on Wiley Online Library for rules of use; OA articles are governed by the applicable Creative Commons License

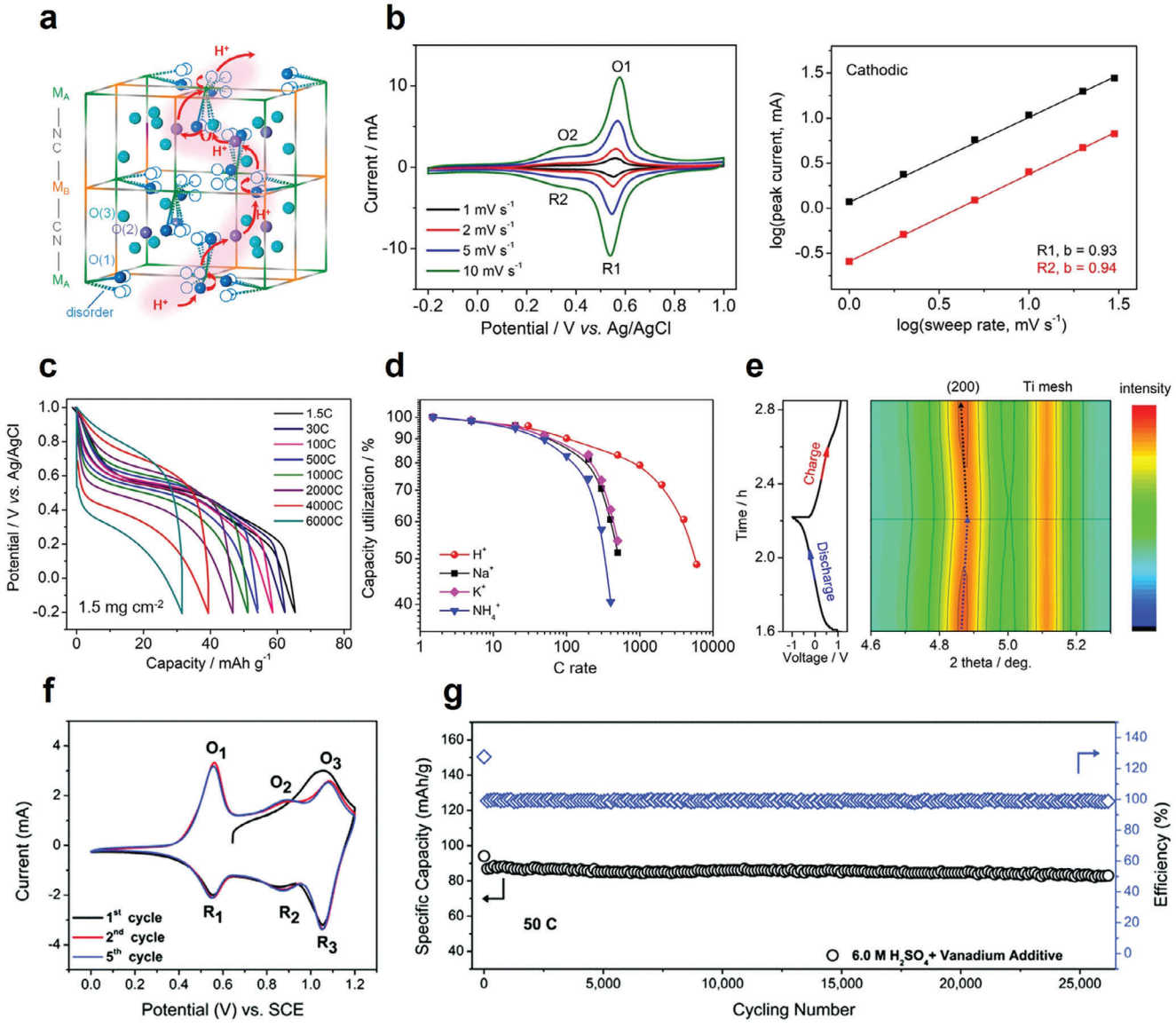

Figure 3. Electrochemical performances and characterizations for PBAs/TBAs. a) Typical crystal structure of PBA, and possible proton transfer pathway through H-bond between ligand and lattice water. Reproduced with permission.[47] b) CV profiles at various scan rates from 1 mV s^{-1} to 10 mV s^{-1} (left) and the corresponding correlations between the cathodic current and scan rate, c) rate performance from 1 C to 6000 C, d) rate comparison between various charge carriers and e) *operando* XRD patterns for NiFe-TBA electrodes in 1 M H_2SO_4. Reproduced with permission.[29] f) CV curves for initial cycles and g) cycling stability of VFe-PBA in 6 M H_2SO_4 electrolyte. Reproduced with permission.[51]

sites of "V" and "Fe" stands out, delivering a record high specific capacity of 108 mAh g^{-1}.[51] As shown in Figure 3f, VFe-PBA possesses three redox pairs between 0.4-1.2 V vs SCE which are assigned to reversible faradaic processes of V^{3+}/V^{4+} (O1/R1), Fe^{2+}/Fe^{3+} (O2/R2) and V^{4+}/V^{5+} (O3/R3), respectively. In addition, the material demonstrates sustained cycling over 25 000 cycles with 91.7% retention (Figure 3g) and excellent rate performance, maintaining 60 mAh g^{-1} at a high current density of 100 C.

Thanks to the high electrode potential, PBAs/TBAs now serve as the common intercalating cathode materials for proton batteries. However, there are certain limitations. First, some PBAs/TBAs tend to show rapid capacity degradation during cycling, which is believed to result from the material electrochemical dissolution during the intercalating step. This can be mitigated through electrolyte regulation strategies, such as adopting concentrated electrolytes with restrained water activities or introducing additives based on the common-ion effect.[51] Second, PBAs/TBAs are mainly prepared by co-precipitation method using potassium ferricyanide. This inevitably incorporates K^+ into the structure, while reducing the amount of intrinsic H^+. To make them suitable for full-cell applications, chemical reductions or electrochemical pretreatments are typically required to introduce protons into the structure. Further improvements are needed to overcome these issues.

© 2024 The Author(s). Advanced Functional Materials published by Wiley-VCH GmbH

RIGHTSLINK

16163028, 2024, 40, Downloaded from https://onlinelibrary.wiley.com/doi/10.1002/adfm.202405401 by Karlsruher Institut F., Wiley Online Library on [05/11/2024]. See the Terms and Conditions (https://onlinelibrary.wiley.com/terms-and-conditions) on Wiley Online Library for rules of use; OA articles are governed by the applicable Creative Commons License

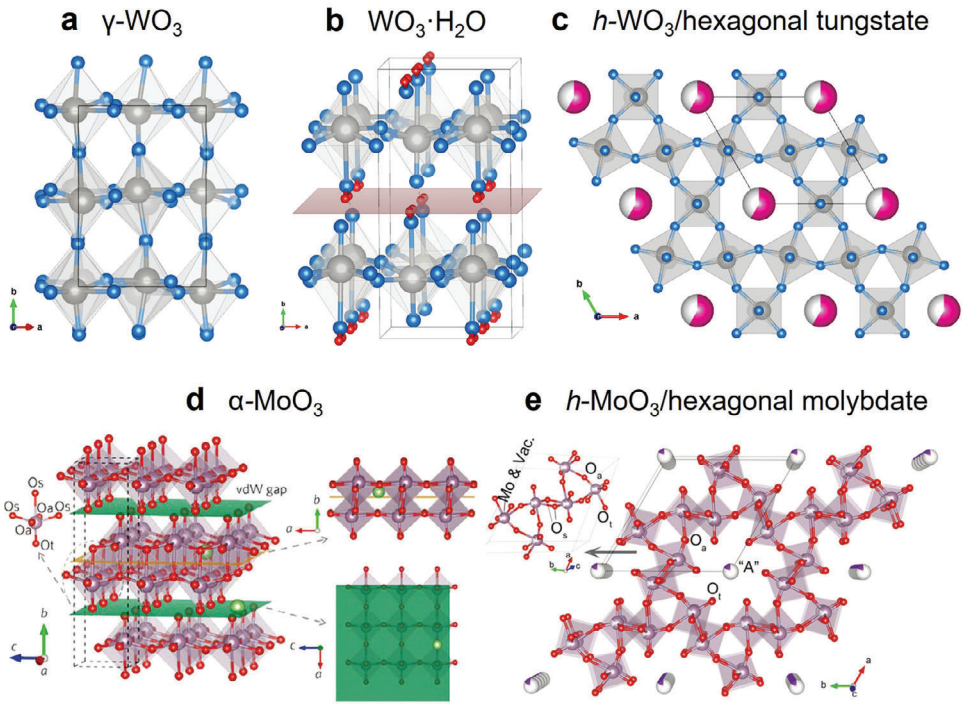

Figure 4. Structure diagram of representative hydrogen-insertion compounds, a-c) type I, d-e) type II. a) γ-WO_3, b) $WO_3 \cdot H_2O$, c) *h*-WO_3/hexagonal tungstate, d) α-MoO_3 and (e) *h*-MoO_3/hexagonal molybdate, respectively. Reproduced with permissions.[54,55]

2.3.2. Metal Oxides

Hydrogen-Insertion Compounds/Hydrogen Bronzes: Hydrogen-insertion compounds, characterized by a general formula of $H_xMO_n \cdot mH_2O$ ("M" can include tertiary metal elements), refer to a group of metal oxides and correlated hydrates capable of undergoing topotactic reaction with dissociated hydrogen (H·) at ambient temperature.[52] These compounds are also known as hydrogen bronzes, as tunable electronic properties are exhibited upon hydrogen-loading, transforming the compounds into either semiconducting or even metallic states accompanied with observable color changes. Recently, these compounds have also been found to react similarly with proton-ions through electrochemical reactions (ion intercalation reactions) and are widely studied as electrodes for proton storage.

Hydrogen-insertion compounds constitute a vast family of materials and are generally classified into two categories based on their atomic bonding features.[52] Type I includes compounds with structures composed of vertex-sharing octahedra [MO_6], exemplified by the γ-WO_3 and correlated hydrate $WO_3 \cdot H_2O$ which exhibit cubic to layered transition (**Figure** 4a,b). Type II consists of compounds formed by edge-sharing polyhedral [MO_n] units, illustrated by examples of the bilayer structured α-MoO_3 (Figure 4d). Both molybdenum oxides and tungsten oxides exhibit hexagonal isomer structures (Figure 4c,e) with bonding features identical to their most common isomers. Noteworthy is the practical presence of certain tunnel cations (metal cation or ammonium, denoted as "A") additional to crystal water in hexagonal structured compounds for charge compensation,[53] a factor often overlooked in many electrochemical studies. These compounds are thus characterized as $H_xAMO_n \cdot mH_2O$, which can also be referred to as tungstates or molybdates. Herein, several representative hydrogen bronzes dedicated to electrochemical proton storage are presented, including molybdenum oxide, tungsten oxides, vanadium oxides, and titanium oxides.

Molybdenum Oxides: So far, there are two kinds of molybdenum oxides reported as faradaic electrodes for proton storage. The first and most widely recognized case is the bilayer-structured orthorhombic oxides (i.e., α-MoO_3). The second is the recently demonstrated tunnel-structured hexagonal phase, which can be designated as *h*-MoO_3 or hexagonal molybdates.

α-MoO_3: The redox chemistry of α-MoO_3 for electrochemical proton-ion storage and the possibility of constructing correlated batteries were initially demonstrated by Wang et al. in 2018.[8] The authors reported a fast rate capability unexpectedly under diffusion-limited kinetics (typically sluggish), and showcased a maximum 0.88 electron transfer (≈164 mAh g^{-1}) and reversible 0.76 electron transfer per reaction in 1.0 M H_2SO_4. Subsequently, higher reversible capacities *c.a.* 220 mAh g^{-1} were achieved by several independent groups using similar aqueous acids (H_2SO_4, H_3PO_4) in higher concentration.[17,24] The maximum ion intercalation extent was demonstrated ≈2.05 units (382 mAh g^{-1}) corresponding well to H_2MoO_3, the known highest-content hydrogen molybdenum bronze (HMB). The high capacity and good rate of α-MoO_3 make it a popular electrode for correlated studies, and surprisingly a three-unit proton-insertion mechanism has been recently demonstrated using liquid crystal electrolytes, pushing for further increased capacities over 500 mAh g^{-1} (maximum, initial) and 350 mAh g^{-1} (reversible, subsequent).[56]

To better exploit the electrochemical potential of α-MoO_3 electrodes, it is crucial to gain a comprehensive understanding of the correlated proton storage mechanisms. One of the key

© 2024 The Author(s). Advanced Functional Materials published by Wiley-VCH GmbH

16163028, 2024, 40, Downloaded from https://onlinelibrary.wiley.com/doi/10.1002/adfm.202405401 by Karlsruher Institut F., Wiley Online Library on [05/11/2024]. See the Terms and Conditions (https://onlinelibrary.wiley.com/terms-and-conditions) on Wiley Online Library for rules of use; OA articles are governed by the applicable Creative Commons License

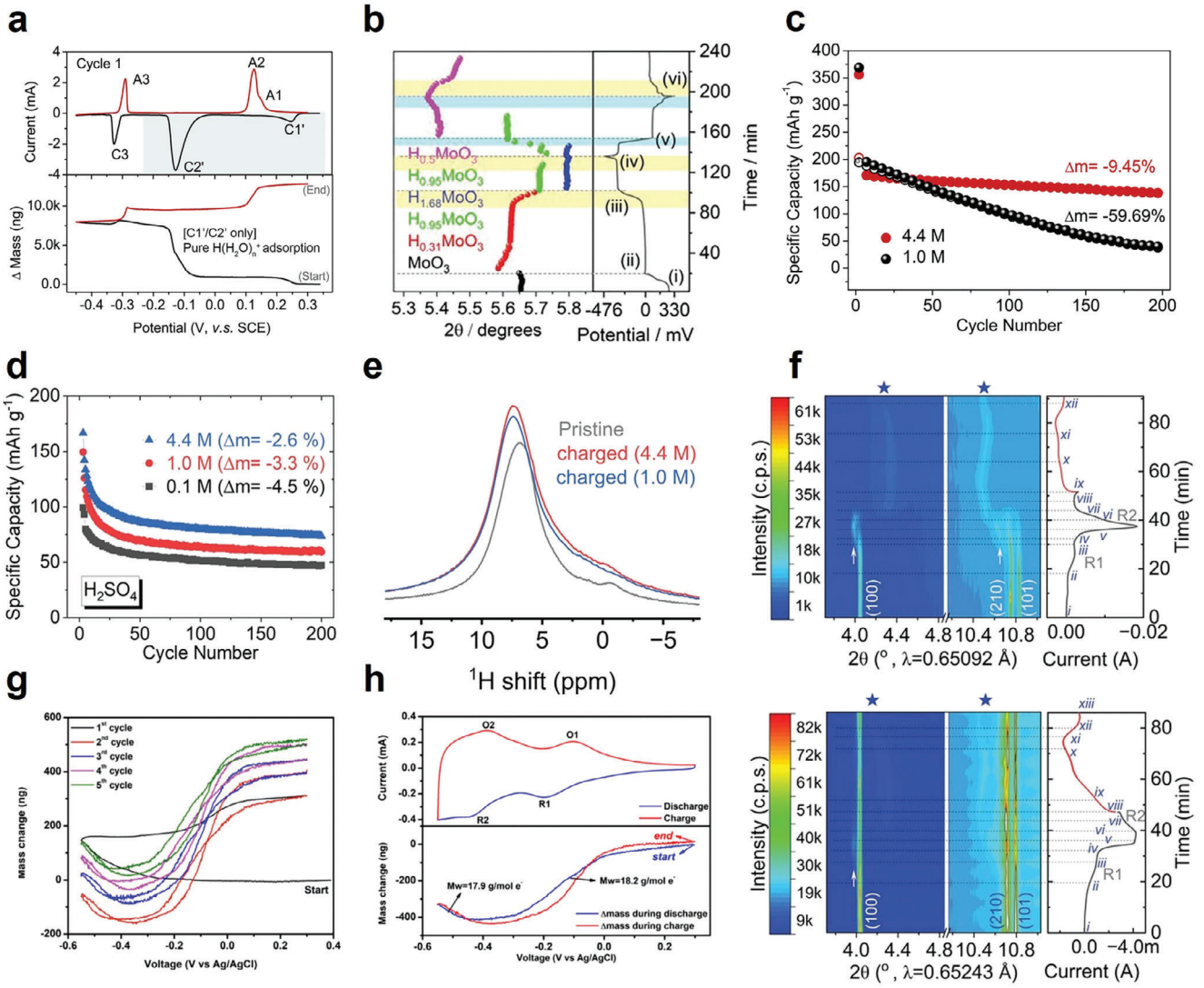

Figure 5. Mechanistic investigations on a-c) α-MoO_3, d-f) h-MoO_3, and g-h) h-WO_3 for electrochemical proton storage. a) EQCM studies on α-MoO_3 in H_2SO_4. CV test (top) at 3 mV s^{-1} and corresponding mass evolution plot (bottom). b) Single peak fitting results of *operando* XRD investigations on α-MoO_3 in H_2SO_4. c) Cycling performance and corresponding mass change of α-MoO_3 electrodes in two H_2SO_4 electrolytes. Reproduced with permission.[17] d) Cycling performance and corresponding mass change of hexagonal $(Na_2O)_{0.07}MoO_3(H_2O)_{0.26}$ in H_2SO_4 of different concentrations. e) ^{1}H ssNMR spectra of $(Na_2O)_{0.07}MoO_3(H_2O)_{0.26}$ electrodes. f) *Operando* XRD contour plots for $(Na_2O)_{0.07}MoO_3(H_2O)_{0.26}$ in 4.4 M (top) and 1.0 M (bottom) H_2SO_4. Reproduced with permission.[55] g) EQCM investigations on hexagonal $WO_3 \cdot 0.6H_2O$ during the first five CV cycles. h) CV profiles of $WO_3 \cdot 0.6H_2O$ (top) and the corresponding E-Δm plots (bottom) in a stable cycle. Reproduced with permission.[9]

challenges is clarifying the true nature of the "ion-charge-carrier". There has been a significant debate regarding whether it involves hydronium insertion,[57] water co-insertion,[24] or naked proton insertion.[17,56] To the best of our knowledge, following findings from various perspectives support the view that only naked protons insert into bulk α-MoO_3 lattices following interfacial hydronium desolvation.[17] As shown in **Figure 5a**, electrochemical quartz crystal microbalances (EQCM) results reveal a noticeable mass increase trend over C1' and C2' processes, which is contributed by the surficial adsorption of hydronium ion on MoO_3. From C3 process onwards, mass changes show inverse trends, suggesting water desorption with vehicular proton transport. After a whole process, a significant mass gap is observed indicating overall water accumulation on electrodes. Interestingly, synchrotron-based *operando* XRD detected no hydrate signal (Figure 5b), but the presence of HMBs alone matched well with the recorded patterns, providing compelling evidence for naked proton insertion. The conclusion is further substantiated by solid-state NMR (ssNMR) where no crystal water signal was detected. Besides, the detrimental impact of solvent water has also been identified, which is believed to induce the cycling degradation of α-MoO_3 and electrodes in dilute electrolytes exhibit much more severe mass loss (Figure 5c). This indicates an electrochemical dissolution by solvent water, rather than the common concern of chemical corrosion, which has also been observed in other electrodes.[37,51,58] Accordingly, improving

© 2024 The Author(s). Advanced Functional Materials published by Wiley-VCH GmbH

RIGHTSLINK

16163028, 2024, 40, Downloaded from https://onlinelibrary.wiley.com/doi/10.1002/adfm.202405401 by Karlsruher Institut F., Wiley Online Library on [05/11/2024]. See the Terms and Conditions (https://onlinelibrary.wiley.com/terms-and-conditions) on Wiley Online Library for rules of use; OA articles are governed by the applicable Creative Commons License

strategies like electrolyte engineering tuning the (water)solvation structure (discussed in later sections) and additional protection layer[59] facilitating proton desolvation have all been proven effective in enhancing the cycling stability of α-MoO_3 electrodes. Interestingly, a recent advance has also revealed an alternative "desolvation-free" charge transfer process of proton insertion in $H_{1.75}MoO_3$ bronzes (achieved from α-MoO_3).[60] This conclusion has been drawn from the measured low activation energy (0.02 eV). Subsequently, the inserted H^+ is transported via an interconnected hydrogen bonding network, depicted as the Grotthuss mechanism (however, there are deviations from that in bulk water, discussed in Section 5.4).

h-MoO_3/Hexagonal Molybdates: *h*-MoO_3 or hexagonal molybdates present unique tunnel structures associated with large intracrystalline space. Combined with the excellent electrical conductivity (550-fold higher than that of α-MoO_3),[61] these materials show great promise for high-power applications. Very recently, two independent research groups have reported fast and stable proton storage performance of micrometer-scale *h*-MoO_3/hexagonal molybdates in H_2SO_4.[55,62] Compared with nanometer-sized materials, micrometer-sized materials not only decrease the side reactions due to the limited electrode-electrolyte interface, but also increase the tapping density of electrodes, boosting the volumetric energy density. The materials showcase a similar maximum capacity (≈375 mAh g^{-1}) as α-MoO_3 with prominent battery-type electrochemical features at the initial discharge and subsequently transform to intercalation pseudocapacitance with good reversible capacity ≈140 mAh g^{-1}, and an impressively high rate is achieved in single crystal with size over 200 µm.[55] The proton storage behavior of *h*-MoO_3/hexagonal molybdates is significantly distinct from that of α-MoO_3, and hydronium intercalation was first demonstrated by a series of experimental characterizations. As shown in Figure 5d, it is found that cyclability is non-sensitive to electrolyte concentration, and all electrodes reach similar stability with close values of minor mass dissolution.[55] Following that, EQCM detected reversible hydronium movements at interface and ssNMR (Figure 5e) revealed intensified crystal water signals in material lattice, thus validating the bulk insertion of hydronium in hexagonal molybdates. The structural chemistry of hydronium intercalation into hexagonal molybdates was then analyzed using synchrotron-based *operando* XRD (Figure 5f). Notable distinctions in structure evolution are easily observed in 4.4/1.0 M H_2SO_4, suggesting the intercalation of hydroniums at different solvation extents. Despite, similar sophisticated reaction path is still identified in both electrolytes, comprising (1) two sets of two-phase reactions, (2) a minute solid-solution reaction in between and (3) a subsequent solid-solution reaction on discharge.

Tungsten Oxides and Hydrates: As typical representatives of type II hydrogen bronzes, various tungsten oxides and hydrates have been intensively studied. In the field of electrochemical proton storage, related reports can be divided into two groups. The first group focuses on (*i*) γ-WO_3, the distorted cubic oxide comprising all vertices-linked [WO_6] octahedra (Figure 4a) and corresponding layered $WO_3{\cdot}nH_2O$ (n = 1, 2) where additional crystal water is situated in the interlayer of [WO_6] octahedral frameworks (Figure 4b). As shown in Figure 4c, the other group centers on (*ii*) hydrous hexagonal tungsten oxides, or more specifically tungstates, which feature the tunnel cations. Within this material class, the distinctive [WO_6] hexa-ring structure presents ample space for readily accommodating various foreign molecules and ions.

γ-WO_3 and $WO_3{\cdot}nH_2O$: Proton insertion in γ-WO_3 is associated with a theoretical capacity of 416 C g^{-1}, grounded in a maximum of one unit electron transfer. The introduction of lattice water ($WO_3{\cdot}nH_2O$, n = 1, 2) was found to lower the theoretical capacities, however, it plays a significant role in improving electrochemical performances in tungsten oxides. For instance, Augustyn and co-workers revealed an interesting electrochemical transition from battery-type energy storage behavior in anhydrous WO_3 to pseudocapacitive redox behaviors in hydrated phase ($WO_3{\cdot}2H_2O$).[63] Furthermore, the transition also resulted in increased practical capacitance and much-enhanced kinetics with superior rate performances. Later research pointed out that the confined interlayer water not only facilitates the rapid electrochemical proton intercalation, but also stabilizes the structure by isolating the structural transformations within 2D.[64]

h-WO_3/Hexagonal Tungstates: Thanks to the enriched intracrystalline space, the tunnel-structured hexagonal tungsten analogue possesses a high surface area, and there are also intrinsic water channels inside the tunnels. These features therefore make the *h*-WO_3 an excellent electrode for intercalation pseudocapacitance. For example, fast proton storage was demonstrated in a hierarchical nanostructured hydrous *h*-WO_3 electrode, achieving a high capacitance retention of 80% at a high scan rate of 100 mV s^{-1} and stable cycling over 50,000 cycles.[65] In 2018, Ji and co-workers studied the proton insertion mechanism in the electrode of hexagonal $WO_3{\cdot}0.6H_2O$.[9] Mainly benefitting the real-time electrode mass monitoring technique of EQCM, the authors concluded the $WO_3{\cdot}0.6H_2O$ intakes extra crystal water from electrolytes during initial cycling, as indicated by the overall mass gains from cycles 1–5 of CV tests (Figure 5g). Furthermore, the authors calculated out apparent values for interacting molecules as 18.2 g mol^{-1} e (in cathodic scan) and 17.9 g mol^{-1} e (in anodic scan) based on the mass variation during the electrochemical process (Figure 5h). These values closely align with the molecular weights of H_3O^+ and H_2O (18 g mol^{-1}). This marks the first assertion of hydronium intercalation in inorganic materials, which is a reasonable conclusion supported by a recent experiment demonstration in similar tunneled analogues.[55] However, it is important to note that EQCM is a surface-limited technique, which may carry potential risks of over-interpretation, and similar mass phenomena observed in α-MoO_3 (Figure 5a) have been shown to yield opposite conclusions.[17] Therefore, more comprehensive analyses are necessary to study the ion-intercalation process. In addition, although tungsten oxides and hydrates usually exhibit considerable cycling stability, their applications are challenged by their limited capacities (<100 mAh g^{-1}), and further material modifications should be considered regarding this issue.

Vanadium Oxides: Composing of [VO_6] octahedral unit, the bi-layered V_2O_5 represents a series of materials with large and tunable interlayer spacings, making them ideal hosts for various cations intercalation.[66] However, regarding to electrochemical proton storage, vanadium oxide electrodes are challenged by their intrinsic dissolution in acidic electrolytes, and correlated proton intercalation is only reported in mild acidic environments, like Lweis acid electrolytes (as concomitant reactions)[67]

© 2024 The Author(s). Advanced Functional Materials published by Wiley-VCH GmbH

RIGHTSLINK

16163028, 2024, 40, Downloaded from https://onlinelibrary.wiley.com/doi/10.1002/adfm.202405401 by Karlsruher Institut F., Wiley Online Library on [05/11/2024]. See the Terms and Conditions (https://onlinelibrary.wiley.com/terms-and-conditions) on Wiley Online Library for rules of use; OA articles are governed by the applicable Creative Commons License

16163028, 2024, 40, Downloaded from https://onlinelibrary.wiley.com/doi/10.1002/adfm.202405401 by Karlsruher Institut F., Wiley Online Library on [05/11/2024]. See the Terms and Conditions (https://onlinelibrary.wiley.com/terms-and-conditions) on Wiley Online Library for rules of use; OA articles are governed by the applicable Creative Commons License

or ultra-dilute acids. Specifically, an ammonium-intercalated V_2O_5 ($(NH_4)_{0.5}V_2O_5$) electrode has been shown to display the optimal electrochemical performance in 0.001 M H_2SO_4, in sharp contrast to the significant dissolution observed in 1 M H_2SO_4.[68] In another case, Zhao et al. achieved reversible proton insertion/extraction in V_2O_5 using a Lewis acid electrolyte (2 M $Al(OTf)_3$, pH = 2). The proton insertion was confirmed by the XRD results of charged electrodes, which fit well with $H_{1.43}V_2O_5$. Although the concentration of proton is much lower than that of Al^{3+} in the electrolyte, the proton insertion prevails, delivering a high capacity of 186 mAh g^{-1}.[69]

Titanium Oxides: Titanium oxides are much less known for electrochromic properties as compared to the above three groups of materials. There are many different structures of titanium oxides. Despite the existence of dedicated bronze phase, current reports on proton insertion mainly correlate to other structures like anatase,[70,71] rutile, and brookite.[72] Balland and co-workers studied the electrochemical protonation processes of nanostructured amorphous TiO_2 in a neutral buffered solution, and a combination of electrical double-layer capacitive and faradaic electrochemical proton storage behaviour was identified.[73] Subsequent work by the same group reveals that the crystallinity of TiO_2 (anatase or amorphous) has little effect on proton storage performance, and both TiO_2 display similar reversible capacities of approximately 150 mAh g^{-1}.[71] The correlated mechanisms are reported by Geng et al.[70] through DFT investigations, it is disclosed hydronium desolvation at the surface of anatase, enabling naked proton insertion with a strain-free characteristic. Nevertheless, Anatase TiO_2 is also found to often associate with inferior cycling stability, with rapid capacity fading over several cycles, possibly due to severe hydrogen evolution reaction (HER) at low potentials and corresponding electrode peel-off by bubble accumulations.[70]Additionally, hydrogen titanates have also been found active for electrochemical protonation, and Augustyn group reported that $H_2Ti_3O_7$ exhibited a high capacity of c.a. 80 mAh g^{-1} in H_2SO_4 electrolytes.[74]

Other Metal Oxides: As discussed in the previous section, proton-insertion oxides are typically associated with color changes with hydrogen loading. Therefore, these materials are also referred as bronzes and are found electrochromic applications. There are several other metal oxides that also have the ability to store protons, but they do not show characteristics as the discussed materials. Such as the well-known hydrous ruthenium oxides ($RuO_2{\cdot}nH_2O$) associating with proton surface redox, and manganese oxides (MnO_2) mainly involving concomitant reactions with protons. Hence, we herein categorize these oxides into a separate group, which can be termed as generalized hydrogen bronzes.

Ruthenium Oxide and Hydrates: RuO_2 is a classic material renowned for its surface redox reaction mechanism, and its supercapacitance feature is characterized by a rectangular-like CV profile. Similar to γ-WO_3, the proton storage properties of RuO_2 are highly dependent on its hydration level. An early report in 1995 compared the electrochemical performance of RuO_2 with various hydration levels.[39] It was found that the moderately hydrated $RuO_2{\cdot}0.5H_2O$ demonstrates a high specific capacitance of 720 F g^{-1}, which is much higher than that of anhydrous RuO_2 (19.2 F g^{-1}). Later work in 2002 further studied the atomic structure of $RuO_2{\cdot}nH_2O$ using atomic pair density function analysis by X-ray scattering.[75] $RuO_2{\cdot}nH_2O$ is a mixed proton-electron conductor, which is found a composite of anhydrous rutile-like RuO_2 nanocrystals dispersed by boundaries of structural water associated with Ru-O. Metallic conduction is supported by the nanocrystalline RuO_2 core, while proton conduction is facilitated by the structure water along the grain boundaries. A close correlation between the capacitance of $RuO_2{\cdot}nH_2O$ and its structural water content has then been discovered, and $RuO_2{\cdot}0.58H_2O$ exhibited a maximum capacitance of 850 F g^{-1}. A following study in 2019 reveals further the fundaments using neutron scattering.[76] It is disclosed the proton conduction proceeds via the typical Grotthuss mechanism, facilitated by the hydrogen-bond chain of rich surface hydroxyl groups and the correlated hydrogen-bonded water molecules. However, $RuO_2{\cdot}nH_2O$ demonstrates limited capacity for battery applications, due to the limited reaction depth only at the surface region.

Manganese Oxides: Manganese oxides have gained considerable attention for supercapacitor and battery research due to their low cost, abundant reserves, and environmental friendliness. Although MnO_2 has a high theoretical capacity of 308 mAh g^{-1} (based on one-electron transfer), its inferior electrical and ionic conductivity results in a low practical capacity.[77] MnO_2-based materials have been widely reported for Zn-ion batteries, accompanied with various reaction mechanisms, and the insertion/extraction of proton is mostly reported as concomitant reactions with metal-cations in mild aqueous electrolytes. For example, Sun et al. reported a subsequent insertion/extraction process of H^+ and Zn^{2+} in electrodeposited ϵ-MnO_2 cathode for MnO_2//Zn batteries.[5] A two-region mixed-ion insertion mechanism was disclosed for ϵ-MnO_2 cathode. The high-potential region, contributing ≈40% discharging capacity, is assigned to H^+ insertion, and can maintain a high utilization rate at high current densities. While the low-potential region (≈60% capacity) is related to the insertion of Zn ions, which suffers from considerable capacity loss at high current densities. Galvanostatic intermittent titration technique (GITT) and EIS results further revealed a much faster diffusion kinetics for the proton-insertion process compared with Zn ion. Such H^+/Zn^{2+} co-intercalation has also been shown to prevail in many other polymorphs of MnO_2, such as α-MnO_2[78] and δ-MnO_2.[79] Furthermore, an alternative conversion reaction between MnO_2 and MnOOH is also disclosed, which can be largely responsive for the charge contribution.

2.3.3. Organic Materials

With increasing concerns about raw mineral resources and environmental disruption, there is an urgent need to develop renewable electrode materials for energy storage applications. Compared with metal-based redox materials, organic electrode materials are mainly composed of H, C, N, O, and S, which have high elemental abundance and are relatively low cost. In addition, organic compounds can be prepared by artificial synthesis or from biomass, providing unique accessibility and sustainability. Importantly, several molecular engineering strategies provide opportunities to modify their chemical and physical properties, tailoring the key factors including redox potential,

© 2024 The Author(s). Advanced Functional Materials published by Wiley-VCH GmbH
RIGHTSLINK

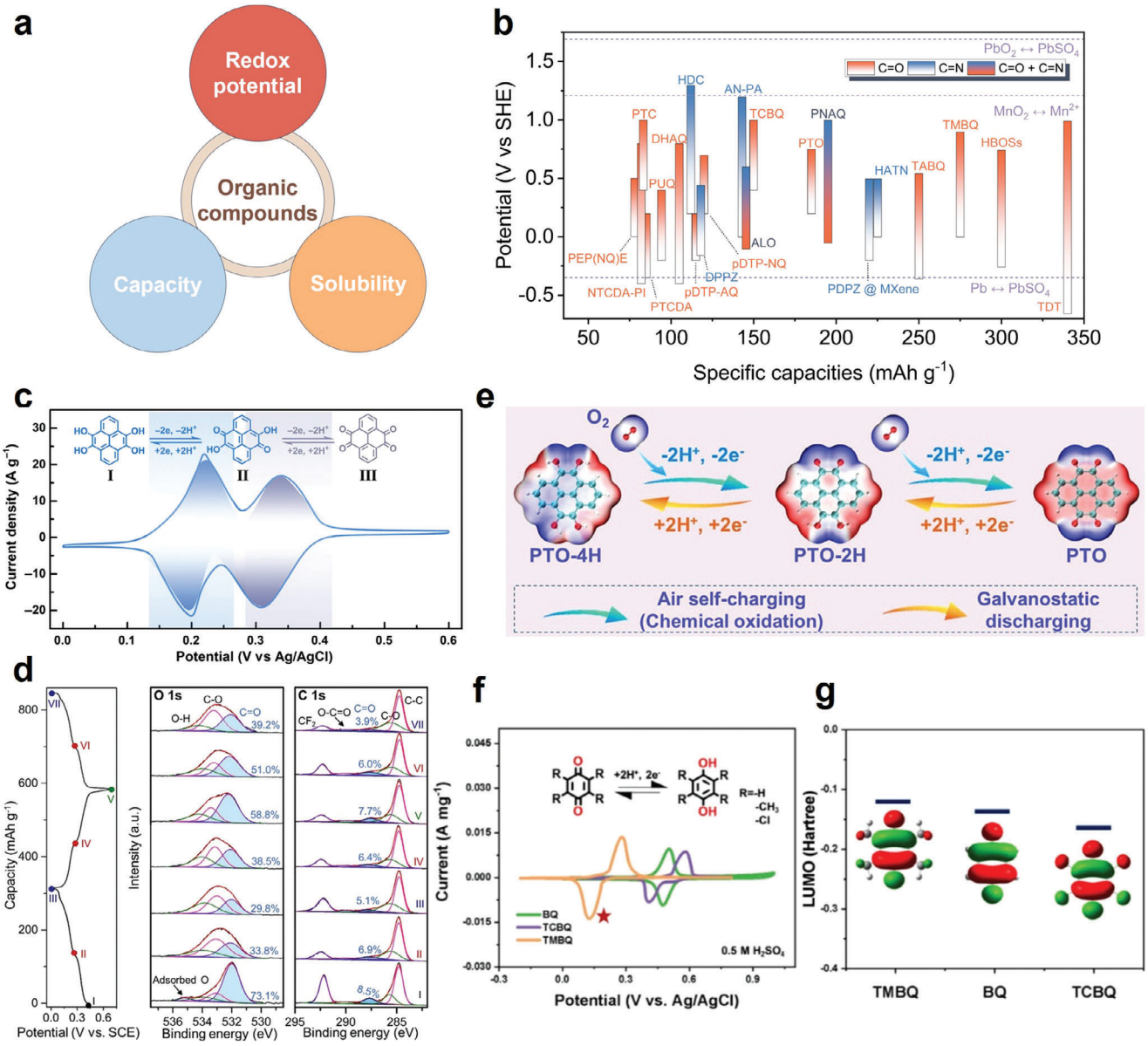

Figure 6. a) Key factors of organic electrodes. b) Summary of working potentials and specific capacities (at 1 A g^{-1}) of representative organic electrodes for aqueous proton batteries.[20,40,41,49,83,86–99] c) CV curve of PTO at 50 mV s^{-1}. Reproduced with permission.[100] d) GCD curves (left) and the corresponding *ex-situ* XPS O 1s and C 1s results of PTO electrodes at different states of charge. Reproduced with permission.[84] e) Schematic illustration of the air self-charging process of PTO. Reproduced with permission.[85] f) CV curves at 1 mV s^{-1} and g) LUMO energy levels of three quinone compounds with different substituent groups. Reproduced with permission.[40]

capacity, and solubility of organic compounds for different application requirements (**Figure 6**a). For example, (*i*) the redox potentials of organic compounds can be effectively adjusted by introducing substituent groups with different electronegativities or by altering the relative positions of the substituent groups; (*ii*) the theoretical capacity of organic compounds can be enhanced by increasing the relative amount of active sites or by reducing the non-electroactive part of molecules; (*iii*) the solubility can be improved by modulating the polarities of organic molecules or by polymerizations. Overall, organic materials show considerable affordability, sustainability, and designability compared with traditional inorganic materials, making them attractive candidates for next-generation energy storage technologies.

The organic electrode materials can be classified into n-type, p-type, and bipolar-type based on the change of charge-state during the GCD process (as shown in Equations 1–4).[80] n-type organic electrodes (M_n), including quinone and imine compounds, can be reduced to a negatively charged state first by accepting electrons, following by coordinating with the cation (i.e. proton) and forming $(M_n)H_x$. Conversely, p-type organic materials (M_p, such as imide compounds) can be oxidized to a positively charged state first, which can be neutralized by the anions (A^-, e.g.

© 2024 The Author(s). Advanced Functional Materials published by Wiley-VCH GmbH

16163028, 2024, 40, Downloaded from https://onlinelibrary.wiley.com/doi/10.1002/adfm.202405401 by Karlsruher Institut F., Wiley Online Library on [05/11/2024]. See the Terms and Conditions (https://onlinelibrary.wiley.com/terms-and-conditions) on Wiley Online Library for rules of use; OA articles are governed by the applicable Creative Commons License

Cl^- and SO_4^{2-}) in the electrolyte. Bipolar-type organic molecules (M_b) show the features of both n-type and p-type cases, and can be either reduced or oxidized. Generally, most p-type organic materials are redox inactive as proton anodes.[31] In contrast, n-type organic materials, which rely on redox centers of carbonyl groups (C=O) or imine groups (C=N), demonstrate considerable electrochemical activity with high capacity (Figure 6b). The O and N heteroatoms intrinsically show considerable electronegativity due to their lone-pair electrons, allowing the uptake/removal of cation charge carriers during cycling (C=O ↔ C-OH and C=N ↔ C–NH).

$$n\text{–type} \quad M_n + xe^- + xH^+ \leftrightarrow (M_n)H_x \tag{1}$$

$$p\text{–type} \quad M_p - xe^- + xA^- \leftrightarrow (M_p)A_x \tag{2}$$

$$\text{Bipolar} - \text{type} \quad M_b + xe^- + xH^+ \leftrightarrow (M_b)H_x \tag{3}$$

$$M_b - xe^- + xA^- \leftrightarrow (M_b)A_x \tag{4}$$

Carbonyl-Containing-Compounds: Quinone and its derivatives have abundant carbonyl groups and PTO is one of the representative compounds that have been reported for aqueous metal-ion batteries with high capacity.[81,82] Guo et al. first introduced pyrene-4,5,9,10-tetraone (PTO) anode for proton batteries.[83] As shown in Figure 6c, PTO shows two pairs of symmetric peaks in CV measurements, which is related to a two-step proton insertion process, delivering a high reversible capacity of 208 mAh g^{-1} and a high capacity retention of 85 mAh g^{-1} at 600 C. When matching with MnO_2/Mn^{2+} cathode redox pair, the PTO//MnO_2 full-cell performs excellent cycling stability of over 5000 cycles, combining with good low-temperature performance at −70 °C. Our group further studied the electrochemical behaviors of PTO in detail.[84] Evolutions of functional groups of PTO during cycling were tracked by *ex-situ* XPS, in which O 1s and C 1s spectra in Figure 6d reveal a reversible quinone-hydroquinone conversion during cycling. In addition, the superiority of proton charge carriers over metal-ion charge carriers was compared by using EIS, where proton charge carriers show the lowest charge transfer resistance and electrolyte resistance, indicating a more facile ion insertion process. When matching with a low-potential redox pair, PTO can also serve as cathode. For example, a Pb//PTO proton full-cell has been introduced by Yue et al.[85] Taking advantage of the air-driven oxidation process of hydroquinone (Figure 6e), self-charging was achieved for the first time in proton batteries. The fully discharged battery can recover a high specific capacity of 236 mAh g^{-1} and an open-circuit voltage (OCV) of 0.93 V after self-oxidation for 12 h.

Small-molecule quinones are usually facile to synthesis, and have also been developed as electrode materials for proton batteries.[98] Chen and co-workers studied the electrochemical behaviors of benzoquinone (BQ) and its derivatives (with tetramethyl- and tetrachloro- groups) for proton batteries.[40] All three molecules undergo reversible quinone-hydroquinone conversion during electrochemical functioning. However, the type of substituent groups can significantly impact their redox potentials as illustrated in Figure 6f,g, where tetramethylbenzoquinone (TMBQ) exhibits the lowest reduction potential due to its higher lowest unoccupied molecular orbital (LUMO) energy. A high specific capacity of 300 mAh g^{-1} at 1 C was achieved for TMBQ electrode. Apart from the type of substituent groups, their positions were also reported to efficiently influence the redox potentials of active sites.[101,102] In addition, small molecule quinones are challenged by the solubility issues in acidic electrolytes, which can be improved by polymerization strategy.[96]

Imine-Containing-Compounds: Imine-containing organic compounds are also widely developed as proton electrodes due to their high redox activity. For example, Lu group developed a novel organic cathode material (2,5-dichloro-1,4-phenylene bis(ethylsulfonylamide), HDC) based on N redox centers for proton storage as shown in **Figure 7a**.[95] Taking advantage of the rational design of molecular structures, that is, through bonding foreign substituents (chloro- and sulfonyl-groups) with strong electron-withdrawing effects, HDC achieves the highest protonation potential (0.9 V vs Ag/AgCl) among reported organic proton cathodes (Figure 7b). Ex-situ Fourier transform infrared spectroscopy (FTIR) in Figure 7c features a reversible conversion between C=N and C–NH energy storage mechanism for HDC molecules, delivering a high capacity of 115 mAh g^{-1}. In another work, Ma et al. introduced a nitrogen-riched diquinoxalino[2,3-a:2′, 3′-c]phenazine (HATN) electrode for aqueous proton batteries.[103] Figure 7d highlights the six C=N moieties possessing more negative molecular electrostatic potential (MESP), thereby serving as active sites for proton uptake. HATN undergoes a three-step six-electron proton insertion reaction pathway (Figure 7e), delivering a high specific capacity of 266 mAh g^{-1}. The narrow energy gap (3.7 eV, Figure 7f) of HATN indicates its good electrical conductivity, resulting in excellent rate performance (97 mAh g^{-1} at 50 A g^{-1}). HATN also demonstrates considerable proton storage performance with mild acidic $ZnSO_4$ electrolyte,[104] indicating its wide application potential. Later, Shi and coworkers introduced poly(diquinoxalino-phenazine) (PDQPZ)[105] and a phenazine-based polymer (PPZ)[106] as proton anodes. Benefiting from the abundant imine active sites and the polymerized structure, both compounds demonstrate practical specific capacities of over 200 mAh g^{-1} at 1 A g^{-1} and exhibit much-enhanced cycling life (over 10,000 cycles) compared to their corresponding monomers. These characteristics fulfill the requirements for both high capacity and high stability simultaneously.

Modification Strategies: The development of organic electrodes is challenged by their intrinsic low electrical conductivity and electrochemical dissolution, leading to inferior rate and cycling performances. Several modification strategies have been developed to solve these issues, including (*i*) hybridizing organic compounds with other materials; (*ii*) introducing extended conjugation structures; and (*iii*) constructing intermolecular H-bond networks.

Nanocarbon materials (e.g. graphene,[40,107] and carbon nanotubes[108]) boast large surface area, and excellent conductivity, making them promising hosts of organic compounds. The conductive porous network serves not only to encapsulate active materials, mitigating material dissolution, but also to facilitate the electron transfer of organic electrodes. For instance, Zhang group proposed a benzo[b]naphtho[2′,3′:5,6][1,4]dithiino[2,3-i]thianthrene-5,7,9,14,16,18-hexone (BNDTH)/reduced graphene oxide (rGO) electrode via a solvent exchange method.[107] Density-functional theory (DFT) calculations revealed a strong

© 2024 The Author(s). Advanced Functional Materials published by Wiley-VCH GmbH

RIGHTSLINK
16163028, 2024, 40, Downloaded from https://onlinelibrary.wiley.com/doi/10.1002/adfm.202405401 by Karlsruher Institut F., Wiley Online Library on [05/11/2024]. See the Terms and Conditions (https://onlinelibrary.wiley.com/terms-and-conditions) on Wiley Online Library for rules of use; OA articles are governed by the applicable Creative Commons License

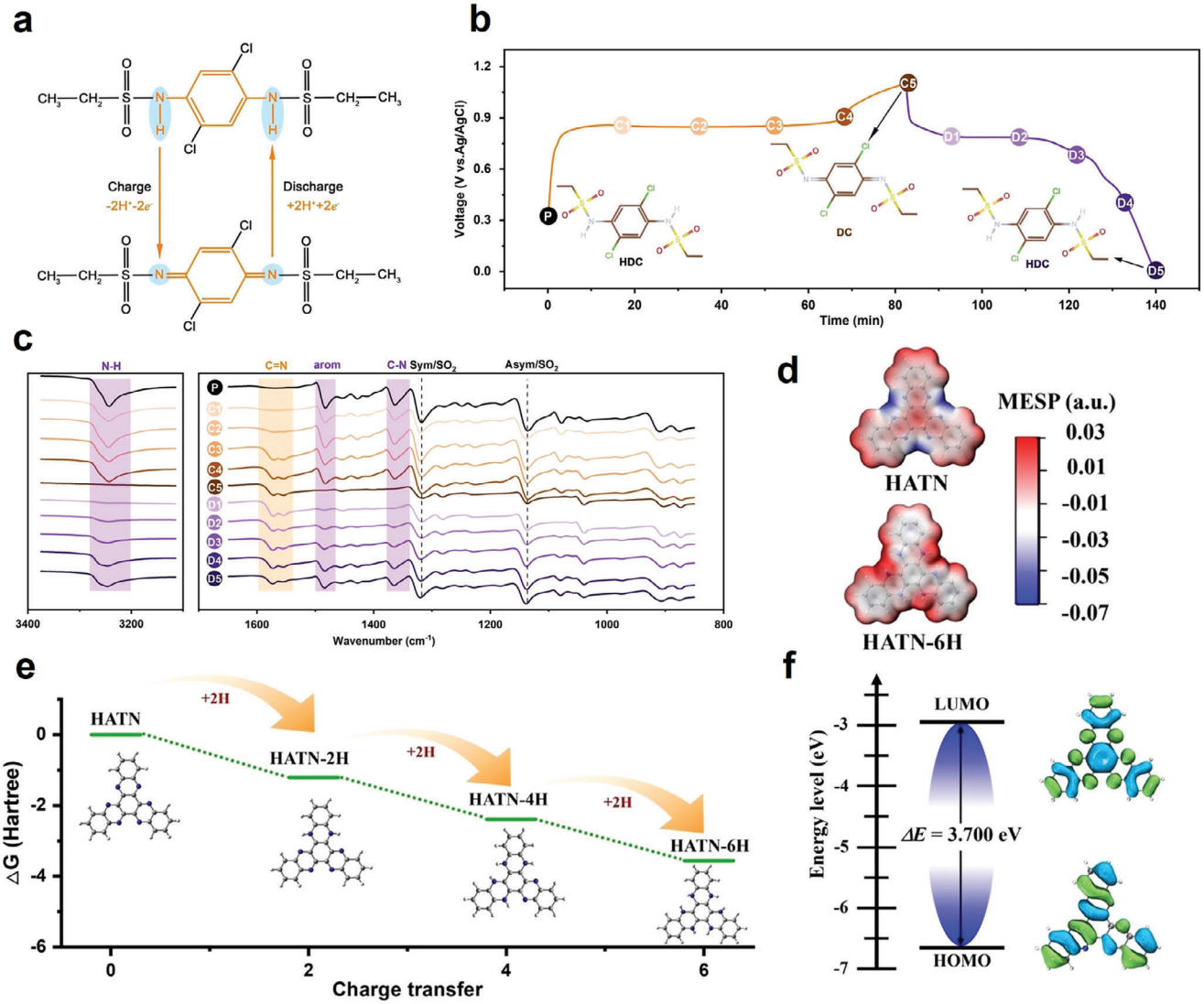

Figure 7. Energy storage mechanisms of imine-group-containing organic compounds. a) Reactions of HDC cathode in proton storage. b) GCD curve of HDC and c) the corresponding ex-situ FTIR spectra of HDC at different states of charge. Reproduced with permission.[95] d) Calculated MESP distribution, e) proton insertion pathway, and f) energy levels of HATN molecule. Reproduced with permission.[103]

π-π interaction between BNDTH and rGO substrate, enhancing interspecies charge transfer. Consequently, the BNDTH/rGO composite demonstrated a high specific capacity of 296 mAh g^{-1}, achieving nearly full utilization of active groups. Other templates or substrates including MXene[92] and zeolite-templated carbon[15] have been explored for loading organic compounds in aqueous proton batteries, however, there remains a notable absence of comparative studies among these substrates.

The rate performance of organic electrodes largely depends on the transfer manner of electrons and ions. Typically, the conductive moieties of organic compounds are the π-conjugated units. Introducing extended conjugation can boost the π-electron delocalization over the molecule, therefore facilitating electron migration and further improving the conductivity of organic compounds. For example, Sun group developed an organic dimer compound (2,3,7,8-tetraamino-5,10-dihydrophenazine-1,4,6,9-tetraone, TDT) for electrochemical proton storage.[99] The localized orbital locator-π (LOL-π) map of TDT features high-degree conjugation throughout the structure, resulting in significantly enhanced electron transfer. As a result, TDT demonstrated semiconductor-level electrical conductivity, achieving excellent rate performance with minimal conductive agent usage (10 wt%). On the other hand, constructing intermolecular H-bond networks can facilitate the proton transfer, enabling Grotthuss-type proton conduction with a lower energy barrier.[109] Recently, Liu group reported H-bond organic superstructures (HBOSs) electrode for proton insertion in zinc-organic batteries.[20] Proton charge carriers can efficiently combine with C=O active sites through the abundant intermolecular H-bonds in HBOSs with low energy barriers of 0.10-0.23 eV, achieving high rate performance (135 mAh g^{-1} at 150 A g^{-1}). The utilization of extended conjugation structures and H-bond chemistry are efficient strategies for

© 2024 The Author(s). Advanced Functional Materials published by Wiley-VCH GmbH

16163028, 2024, 40, Downloaded from https://onlinelibrary.wiley.com/doi/10.1002/adfm.202405401 by Karlsruher Institut F., Wiley Online Library on [05/11/2024]. See the Terms and Conditions (https://onlinelibrary.wiley.com/terms-and-conditions) on Wiley Online Library for rules of use; OA articles are governed by the applicable Creative Commons License

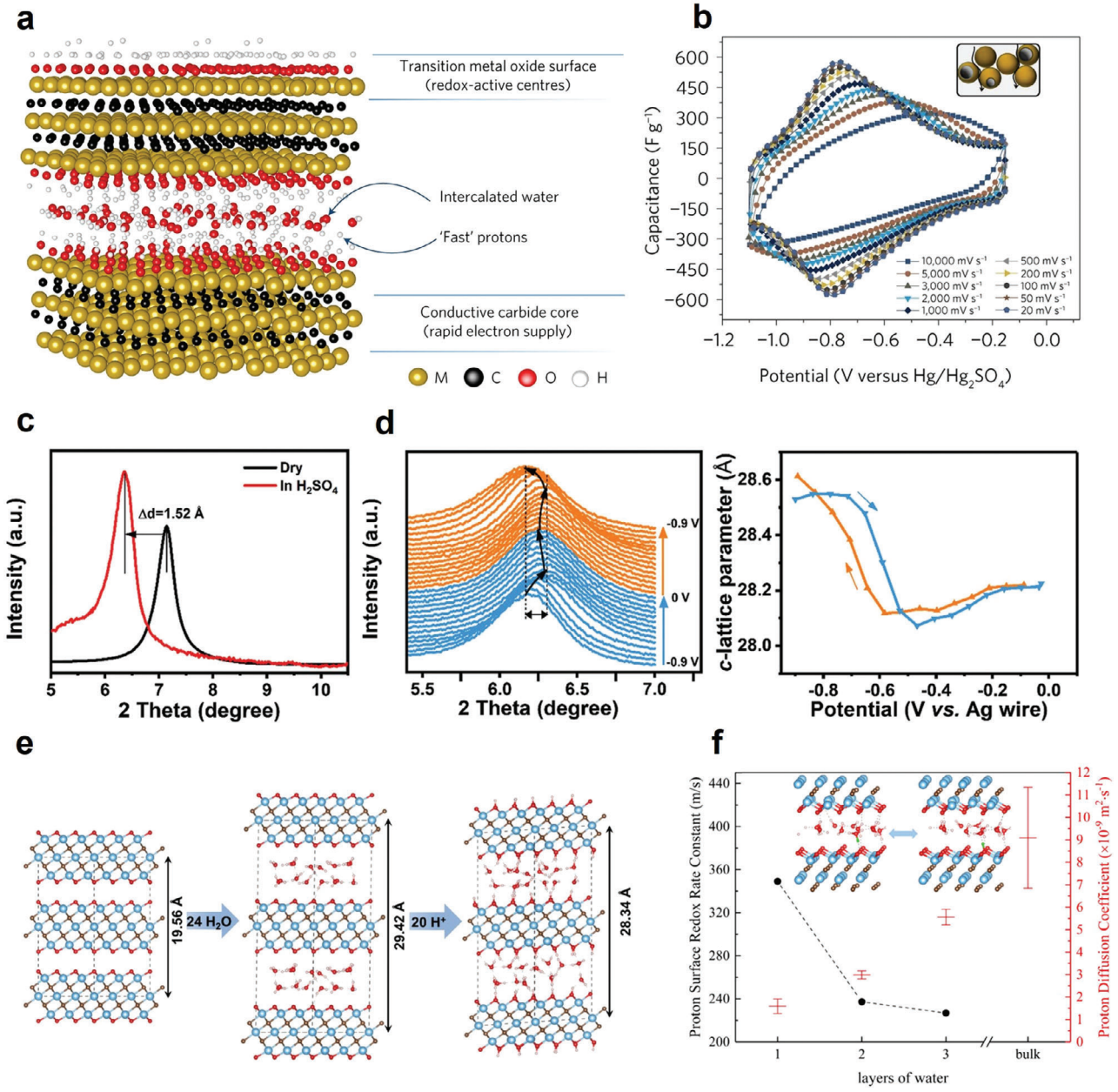

Figure 8. Electrochemical performances and mechanism studies of MXene in aqueous proton batteries. a) Schematic illustration of MXene structure. b) CV profiles of $Ti_3C_2T_x$ electrode in 3 M H_2SO_4 electrolyte at various scan rates from 20 mV s^{-1} to 10000 mV s^{-1}. Reproduced with permission.[111] c) XRD patterns of $Ti_3C_2T_x$ in a dry state and immersed in 1 M H_2SO_4. (d) *In-situ* XRD patterns of $Ti_3C_2T_x$ in 1 M H_2SO_4 electrolyte during a reversible electrochemical cycle (cycle 3; left) and the corresponding *c*-lattice parameter change (right). e) Simulation of H_2O and H^+ intercalation into $Ti_3C_2O_2$ supercells. Reproduced with permission.[113] f) Summaries of proton redox and transport in MXene-confined water. The surface redox rate is much higher in the highly confined one-layer water, while proton mobility increases with the water-layer number. Reproduced with permission.[19]

designing robust organic electrodes from their internal structure.

2.3.4. MXenes

MXenes, a new cluster of 2D materials, were first invented in 2011 by chemical etching of transition metal carbides, resulting in a general chemical formula of $M_{n+1}X_nT_x$ (M for transition metal; X for C or N; T for surface function groups).[110] **Figure 8a** displays the representative MXene of $Ti_3C_2T_x$ which shows a layered structure:[111] a conductive inner transition metal carbide layer guarantees fast electron supply to redox active sites; a surface with rich terminal groups (resembling transition metal oxide) provides abundant active sites for electrochemical reaction; an interlayer with pre-intercalated water molecules enables fast ion transportation. $Ti_3C_2T_x$ MXenes can allow intercalations of a wide variety of cations (including multivalent cations)

© 2024 The Author(s). Advanced Functional Materials published by Wiley-VCH GmbH

RIGHTSLINK

16163028, 2024, 40, Downloaded from https://onlinelibrary.wiley.com/doi/10.1002/adfm.202405401 by Karlsruher Institut F., Wiley Online Library on [05/11/2024]. See the Terms and Conditions (https://onlinelibrary.wiley.com/terms-and-conditions) on Wiley Online Library for rules of use; OA articles are governed by the applicable Creative Commons License

displaying rectangular-shape CV profiles,[112] reminiscent of that of electrical double-layer capacitance. Regarding proton-ions, an additional broad redox peak can be observed in H_2SO_4 attributed to fast surface redox storage (pseudocapacitive) mechanisms, as shown in Figure 8b. Benefiting from that, MXene electrodes achieve the highest capacitance with proton-ions, which can retain a specific value of 210 F g^{-1} in H_2SO_4 even at an extremely high scan rate of 10 V s^{-1}.

The correlated charge storage mechanisms of proton-ions intercalation were then investigated. Figure 8c,d show the XRD investigations by Mu et al. Immersing a dry $Ti_3C_2T_x$ electrode in H_2SO_4 induced a significant increase in interlayer spacing up to 1.52 Å (3.04 Å expansion in *c* parameter), attributed to the intercalation of water molecules. In comparison, the continuous peak shifts observed in reversible processes (e.g., cycle 3) are notably smaller, corresponding to a much-restrained *c* parameter change within 0.5 Å. Such continuous peak evolution without phase change indicates a solid-solution intercalation of proton-ions, which is similar to other cations but more complicated. DFT calculations were then performed and disclosed a two-step pseudo-intercalation (Figure 8e). A following study by Sun et al. analyzed the mechanism further in O-terminated Ti_3C_2, benefitting first-principle molecular dynamics (FPMD) simulations.[19] It is revealed the proton surface redox reversibly occurs between the interfacial water molecules and surface -O terminals, which is intermitted by the more frequent in-water proton transfer events. The solid-state proton transportation is found to follow the same Grotthuss mechanism in the 2D-like confined water (independent from the thickness) as in the 3D bulk water. Given the rapid surface redox and in-water transfer for the intercalated protons, it is implied the intercalating step is likely one of the bottlenecks for the ionic transport.

2.3.5. Electrolytic Electrodes

Most reported proton electrodes function at relatively low redox potentials even near the HER limit, owing to the thermodynamics of protonation reactions. The limited cathode choices significantly restrict the development of proton full-cells. In this case, electrolytic reactions that are supported by electrolytes have been alternatively introduced to expand the electrode selection pool. The reported electrolysis-based electrodes include: (*i*) Manganese electrolysis reaction. MnO_2/Mn^{2+} redox reaction is the most commonly adopted cathode for electrolyte proton batteries, due to the high potential and facile preparation.[37,40,83] (*ii*) Lead-based electrolysis reactions. The conversion reactions of both sides for lead-acid batteries (cathode: $PbO_2/PbSO_4$[16]; anode: $PbSO_4/Pb$[41,85]) have been introduced into proton batteries as counter-reactions, based on their low cost and commercially available features. (*iii*) Gas-based electrolysis reaction. Hydrogen evolution reactions (HER)/hydrogen oxidation reactions (HOR) and oxygen evolution reactions (OER)/oxygen reduction reactions (ORR) conversion reactions have been utilized as counter reactions with the help of bifunctional catalysts such as Pt/C.[114] and $Pt/IrRuO_2$.[43] (*iv*) Metal deposition reaction. The electrochemical plating/striping of Zn[2] and Al[115] metals emerged as the counter reactions for proton batteries in mild Lweis acid electrolytes. (*v*) Halide electrolysis reaction. Redox conversion between polyhalide ions, including Br_3^-/Br^-[116] and I_3^-/I^-[117] are promising counter-reaction choices for protonic electrodes due to their attractive potential, multi-valent nature, and fast conversion kinetics. More details regarding these electrolytic conversion electrodes are discussed later.

3. Electrolytes

Electrolytes are crucial to the operation of proton batteries, facilitating the conduction of proton-ions and establishing a connection between the two electrodes. The existing forms of electrolytes can endow the proton full-cells with unique physical and mechanical properties. Given the unique characteristics of proton electrode materials, the electrolytes in proton batteries often serve as the primary source of proton-ions of the whole system. Consequently, acids are naturally selected as the optimal electrolytes. This section delves into the classification of these acid electrolytes, explores the challenges associated with their utilization, and outlines innovative strategies aimed at enhancing their performance.

3.1. Classifications

As depicted in **Figure 9a**, the electrolytes can be classified according to the source of proton-ions. This classification aligns with the definitions and categories of acids, namely Arrhenius acid, Brønsted acid, and Lewis acid.

Arrhenius Acid: Arrhenius acid, often referred to as aqueous acid, is the most widely studied category and therefore holds particular significance in the realm of proton battery research. Among different aqueous acids, sulfuric acid often acts as the default electrolyte and almost all explored proton electrode materials have undergone electrochemical evaluations in sulfuric acids, including the early report of $RuO_x{\cdot}nH_2O$,[39] and α-MoO_3[118] in the 1990s. It is worth noting that previous investigations typically employ low-concentration sulfuric acid (<1.0 M) possibly out of chemical corrosion concerns. However, recent observations in several proton intercalation materials highlight that concentrated acids can yield superior electrochemical performances, attributed to enhanced electrolyte conductivity,[111] low-temperature performance, and/or reduced materials electrochemical dissolution (to be discussed later).[17] Various other aqueous acids are also reported as electrolytes for proton batteries, including HCl,[119] CH_3COOH,[120] HBF_4,[97] and H_3PO_4.[24] Notably, H_3PO_4 gains prevalence because of the stable anion and relatively less chemical corrosivity.[24] Furthermore, hybrid solutions based on aqueous acids are also adopted, particularly in electrolytic proton batteries, and a typical example is a mixture of H_2SO_4 and $MnSO_4$.[37]

Brønsted Acid: Brønsted acids refer to entities that contribute protons to the Brønsted base.[122] This concept extends beyond the scope of Arrhenius acid, and proves beneficial in characterizing electrolytes with non-aqueous solvents and solvent-free protic ionic liquids. For instance, a non-aqueous acetonitrile solvent has been adopted in the Brønsted acids. This involves incorporating acid solutes (e.g. H_3PO_4[36]) and ionic liquid solutes (e.g. 1-methyl-1,2,4-triaolebis(trifluoromethylsulfonyl)imide).[123] Specifically, Ji group introduced a non-aqueous H_3PO_4 electrolyte to improve the cycling

© 2024 The Author(s). Advanced Functional Materials published by Wiley-VCH GmbH

RIGHTSLINK

16163028, 2024, 40, Downloaded from https://onlinelibrary.wiley.com/doi/10.1002/adfm.202405401 by Karlsruher Institut F., Wiley Online Library on [05/11/2024]. See the Terms and Conditions (https://onlinelibrary.wiley.com/terms-and-conditions) on Wiley Online Library for rules of use; OA articles are governed by the applicable Creative Commons License

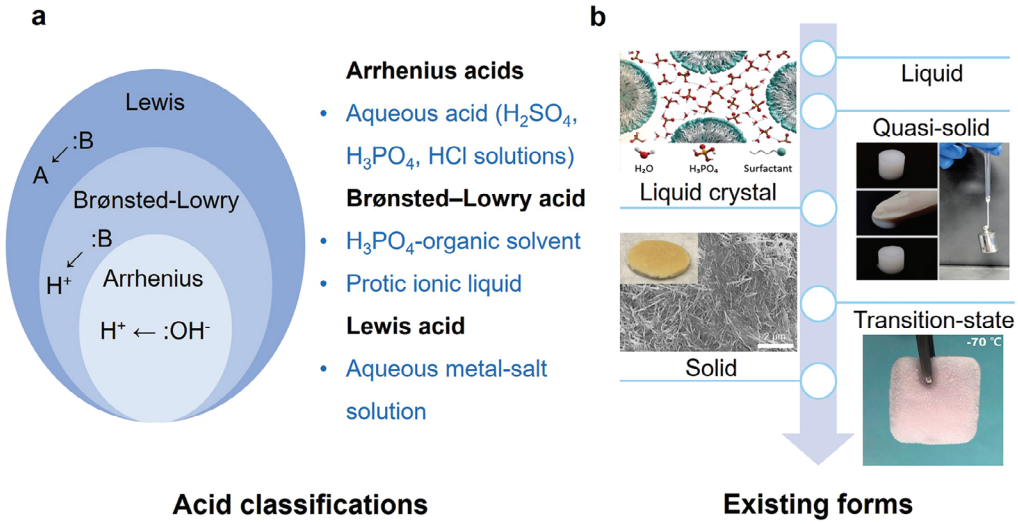

Figure 9. Classification of electrolytes for proton batteries, a) based on acid types and b) based on existing forms. Reproduced with permission.[23,25,56,121]

stability of proton electrode.[36] Concentrated H_3PO_4 (98%) was dissolved in acetonitrile solvent with the addition of stoichiometric amount of P_2O_5 to eliminate residual water. This non-aqueous electrolyte system demonstrated considerable compatibility with various proton electrode materials, eliminating the side reaction (i.e. OER) and mitigating the electrochemical dissolution of electrode material due to the absence of water molecules. Additionally, the innovation of a solvent-free protic liquid, polyphosphoric acid has also been reported by Liao et al.[26] This electrolyte system showcased considerable thermal and electrochemical stability, achieving a wide working temperature range (> 400°C) and a wide electrochemical stability window (ESW, >2.5 V).

Lewis Acid: A Lewis acid is defined as a species that accepts a pair of electrons from another entity,[124] which broadens the classification of acids to encompass proton-free species. Notably, some Lewis acids have been featured in reports focusing on electrochemical proton storage. $ZnCl_2$ is a common Lewis acid with medium acidity and very high solubility, Ma et al. have accordingly designed a superconcentrated Lewis acid electrolyte (32 M $ZnCl_2$ and 1 M P_2O_5 in H_2O).[125] Employing the electrolyte, anhydrous fast proton transport is enabled in the dense oxide-ion array of α-MoO_3, and overall a stable Zn//α-MoO_3 battery has been demonstrated. In addition, various organic electrodes are also reported for reversible proton storage with Zn-salt-based Lewis acid electrolytes ($Zn(OTf)_2$[20] and $ZnSO_4$[98]). The lower activation energy and fast kinetics making proton coordination is prior to Zn^{2+} into active sites. Lewis acids based on Al^{3+} are associated with higher acidity, and $Al(OTf)_3$[69] has been shown to link proton intercalation materials with Al anode, expanding the energy storage applications.

On the other hand, the electrolytes can also be classified based on their physical states. As illustrated in Figure 9b, there are two fundamental states: liquid-phase electrolytes and solid-state electrolytes. Additionally, there also exist liquid crystal electrolytes, transition-state electrolytes, and quasi-solid (hydrogel) electrolytes. Given that the predominant acid electrolytes in proton batteries are found in the liquid phase, the following discussion focuses solely on the other electrolytes developed in proton batteries.

Solid-State Electrolytes: Different from a liquid, a solid holds a definite shape and volume and the constituent particles are closely packed together either with or without long-range ordering. For example, Li and co-workers have introduced a new family of proton electrolytes: acid-in-clay electrolyte (AiCE), which is achieved by integrating fast proton carriers in a natural phyllosilicate clay network, resulting in fluid-impervious membranes.[23] The proton conductive networks in AiCE support top-ranked proton conductivities at various wide temperatures (−82 °C− 25 °C), wide electrochemical stability window (3.35 V), and reduced reactivity. AiCE also demonstrated excellent ion-selectivity by restricting the ion cross-over between cathode and anode, achieving significantly improved cycling stability of MoO_3//CuFe-PBA full-cell. A new organic-based solid electrolyte has also been discovered, which is a glassy-state coordination polymer (CP) of $[Zn_3(H_2PO_4)_6(H_2O)_3]$(1,2,3-benzotriazole) with anhydrous single-ion proton conductivity.[126] Melt-quenching treatment of CP not only delivers an isotropic disordered domain with enhanced H^+ conduction, but also generates an immersive electrode-electrolyte interface. The resulting all-solid-state proton battery showcased a wide operating temperature range from 25 to 110 °C.

Quasi-Solid Electrolytes: Quasi-solid electrolytes mainly refer to electrolytes composed of hydrogel. A hydrogel is a biphasic material, comprising 3D networks of hydrophilic polymers and interstitial fluid (primarily composed of water).[127] Thanks to the chemical and (or) physical cross-linking of individual polymer chains, hydrogels are generally capable of swelling in water and retaining a significant amount of water while preserving their solid structure.[128] In the realm of proton batteries, several quasi-solid hydrogel electrolytes have been reported recently. In 2022, Shen et al. devised a hydrogel electrolyte based on polyvinyl alcohol (PVA) and H_2SO_4 (1 M), and subsequently demonstrated a flexible metal-free quasi-solid battery with an organic cathode and activated carbon anode.[95]

© 2024 The Author(s). Advanced Functional Materials published by Wiley-VCH GmbH

RIGHTSLINK
16163028, 2024, 40, Downloaded from https://onlinelibrary.wiley.com/doi/10.1002/adfm.202405401 by Karlsruher Institut F., Wiley Online Library on [05/11/2024]. See the Terms and Conditions (https://onlinelibrary.wiley.com/terms-and-conditions) on Wiley Online Library for rules of use; OA articles are governed by the applicable Creative Commons License

In the same year, Sun et al. fabricated an anti-freezing hydrogel electrolyte by random copolymerization of acrylamide (AM) and zwitterionic monomer, [(methacryloyloxy)ethyl]dimethyl-(3-sulfopropyl)ammonium hydroxide (SBMA), with ethylene glycol (EG) and H_2SO_4 (1 M).[121] Further investigations into the mechanism attributed the high proton conductivity to proton hopping migration on the ionic groups of the polymer chains and Grotthuss proton translation, with Grotthuss translation found to be predominant in the glassy state of the polymer chains. The resulting electrolytes were then combined with two activated carbon electrodes to create solid supercapacitors, that exhibited decent electrochemical performance at −50 °C. Benefiting from the considerable tensile properties of the hydrogel electrolyte, the full-cell demonstrates excellent mechanical fatigue resistance with insignificant capacity loss in the stress-strain experiments. In 2023, another freezing-tolerant hydrogel with double-network was reported by Dong et al.[129] The authors incorporated sulfonated poly(ether-ether-ketone) (SPEEK) and an ethylene glycol/water solvent within the poly(vinyl alcohol) hydrogel network, and consequently enhanced mechanical properties and low-temperature tolerance (−50 °C) were achieved. Benefitting the hydrogel electrolyte, a quasi-solid proton battery (α-MoO_3//NiFe-PBA) demonstrated decent performance such as stable cycling, high rate and low-temperature operation under −20 °C.

Liquid Crystal Electrolytes: Liquid crystals (LCs) represent an intermediate state of matter between crystalline solids, distinguished by a regular periodic arrangement of atoms or molecules, and isotropic liquids, which lack any form of order. LCs display varying degrees of orientational and/or translational order in specific spatial directions.[130] Very recently, a phosphoric acid surfactant lyotropic liquid crystalline (PSL) electrolyte has been reported by Alshareef group.[56] The PSL electrolyte was prepared by dissolving polyoxyethylene lauryl ether surfactant in the H_3PO_4. The robust hydrogen bonding between the components in PSL electrolyte significantly suppresses the activity of free water molecules, improving the electrochemical stability. Thanks to the PSL electrolyte with a widened ESW, a three-proton insertion mechanism has been discovered in α-MoO_3 for the first time.

Transition-State Electrolytes: There are also some electrolytes that present different physical states with temperature variations. These have been categorized as transition-state electrolytes herein, and mainly refer to a novel class of "aqueous" electrolytes in the solid "ice" form. Despite that, there presents a common phenomenon of water/ice phase transition at 0 °C, the electrochemical behaviors of ice have rarely been investigated. In 2019, the ice phase was discovered to provide efficient ionic transport channels, enabling the creation of ionic conducting ice (ICIs, frozen from ion-containing solutions) which shows possibilities to serve as solid-state electrolyte.[131] In 2020, Wang group first introduced ICIs of $MnSO_4$ and H_2SO_4 hybrid aqueous electrolytes in proton chemistry with demonstrations of solid-state proton batteries. These batteries employed a MnO_2/Mn^{2+} electrolytic cathode and α-MoO_3[25] and PTO[83] anodes, respectively. Thanks to the fast proton transportation, robust overall ionic conductivity can be sustained at low temperatures even down to −70 °C. This facilitates the execution of representative redox processes of proton electrodes, showcasing the featured low-temperature performance of proton batteries.

3.2. Limitations

Despite the various acid categories discussed, aqueous electrolytes remain predominant among all reported electrolytes for proton batteries. Therefore, we herein emphasize the challenges encountered in these aqueous electrolytes. As shown in **Figure 10a**, the active proton ion is solvated by water molecules in aqueous solution, and there are three major side influences which are believed to primarily stem from the influence of active water molecules in electrolytes, namely *i)* material dissolution, *ii)* limited ESW, and *iii)* gassing issue.

3.2.1. Electrode Material Dissolution

There are commonly observed phenomena in various materials involvingactive mass loss during cycling, such as hydrogen-insertion oxides[17,36,55] and Prussian blue analogues,[36,51] etc. This phenomenon, known as material dissolution, is considered as the major reason for electrode and battery cycling decay. Notably, such material loss does not adhere to common sense expectations of being induced by chemical corrosion (as many materials are found sustainable even in strong acids). Instead, it is caused by electrochemical effects, which can be mainly attributed to the "attack" from the active water molecules in electrolytes, as illustrated in Figure 10a. This is supported by the following factors. (*i*) It has been revealed that various electrode materials could exhibit superior cycling performance with reduced active mass loss, when associating with concentrated (aq.) or non-aqueous acids.[17,36,51,58] (*ii*) Further, despite proton-ions existing in aqueous solution as hydroniums, $H(H_2O)_n^+$, numerous studies have disclosed that the naked proton alone inserts and migrates in the electrode lattice, and hydronium desolvation steps have been detected at the interface.[17,70,125] (*iii*) A reduction in the fraction of free water molecules or their activities has been shown to alleviate the material dissolution, leading to significantly improved cycling stability.[21,22,132]

In general, the presence of free water molecules exerts a negative impact on proton intercalation materials. One possible explanation is the tendency for solvent water to co-insert with protons into the electrode materials,[55,84] potentially driven by the high desolvation energy of hydronium.[133] However, owing to the substantial size of $H^+(H_2O)_n$ (e.g., Zundel/Eigen cations[10]) and high polarity of water molecules, they inevitably interfere the internal electric field of the material crystal. Consequently, this leads to material lattice distortion (and even layer exfoliation), which serves as a buffer layer to "track" or accommodate co-inserted water and facilitate the passage of naked protons. These manifest as hydronium desolvation and the electrochemical dissolution of material from the surface inward. On the other hand, it is noteworthy that for materials permitting direct hydronium intercalation, their cycling stability is not sensitive to the water fractions in electrolytes.[55]

3.2.2. Limited ESW

The electrochemical stability window (ESW) defines the range within which the electrolyte remains stable, without undergoing

© 2024 The Author(s). Advanced Functional Materials published by Wiley-VCH GmbH

16163028, 2024, 40, Downloaded from https://onlinelibrary.wiley.com/doi/10.1002/adfm.202405401 by Karlsruher Institut F., Wiley Online Library on [05/11/2024]. See the Terms and Conditions (https://onlinelibrary.wiley.com/terms-and-conditions) on Wiley Online Library for rules of use; OA articles are governed by the applicable Creative Commons License

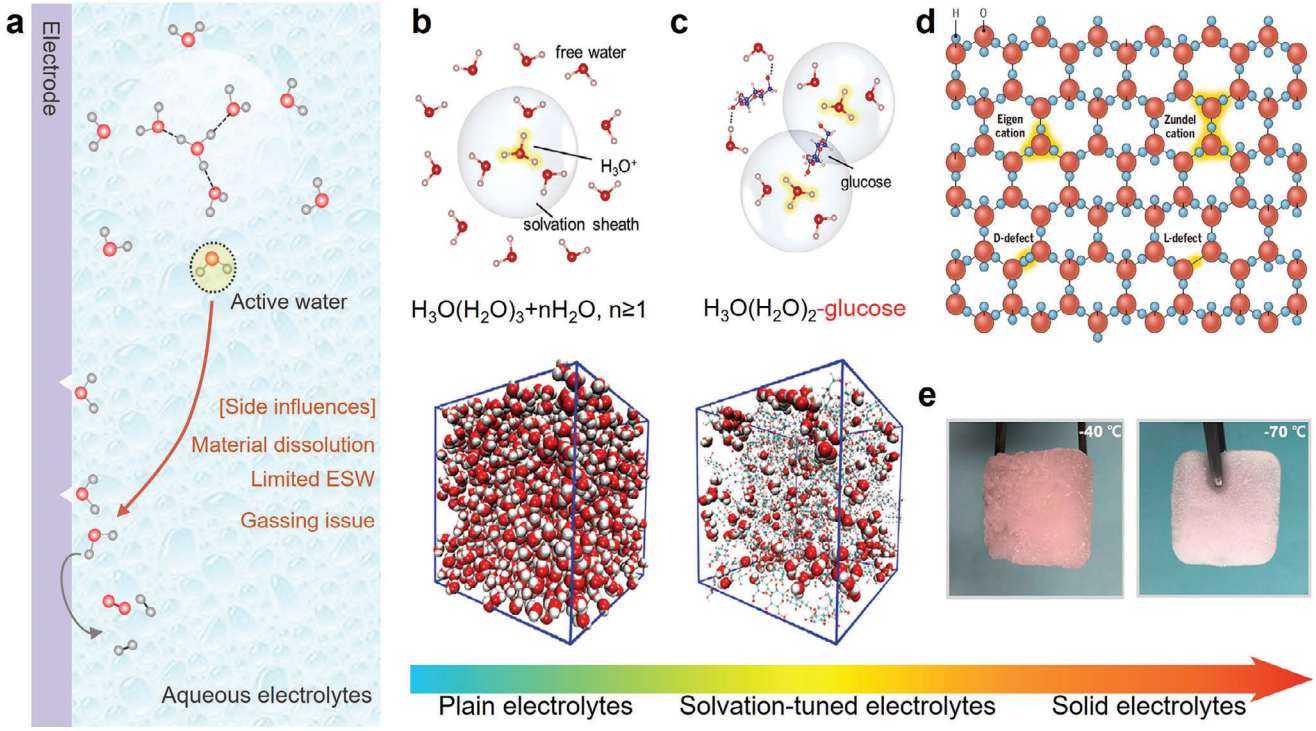

Figure 10. Challenges of electrolytes for proton batteries and improving strategies. a) Schemes illustrating the proton solvation in aqueous electrolytes and corresponding side influences raised. Improving strategies of b,c) tuning water solvation structure in (liquid) electrolyte, and d,e) developing solid-state electrolytes. d) Scheme of proton-water configuration in ice, and e) optical photo of ionic conducting ice. Reproduced with permission.[21,25,134]

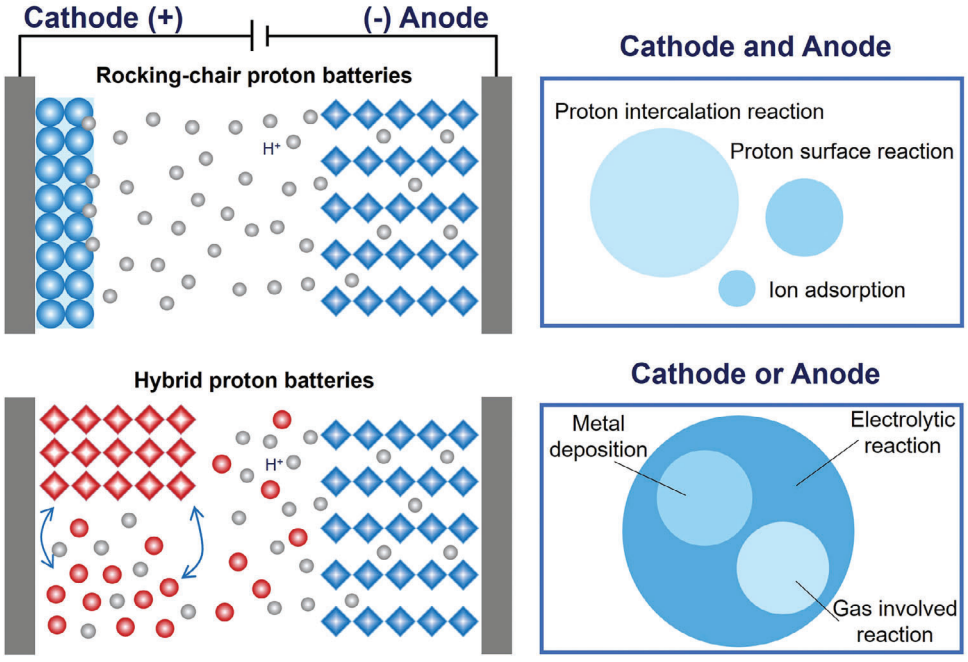

Figure 11. Schematic diagram and reaction classification for rocking-chair proton batteries (top) and hybrid proton batteries (bottom).

© 2024 The Author(s). Advanced Functional Materials published by Wiley-VCH GmbH

16163028, 2024, 40, Downloaded from https://onlinelibrary.wiley.com/doi/10.1002/adfm.202405401 by Karlsruher Institut F., Wiley Online Library on [05/11/2024]. See the Terms and Conditions (https://onlinelibrary.wiley.com/terms-and-conditions) on Wiley Online Library for rules of use; OA articles are governed by the applicable Creative Commons License

Table 1. Summary of recent designs of aqueous proton full-cells.

Anode//Cathode	Electrolytes	Voltage [V]	Median discharge voltage [V]	Temp. [°C]	Specific capacity	Rate	Cycling performance	Refs.
Rocking-chair type proton full-cell								
h-WO_3//CuFe-TBA	2 M H_2SO_4	0.4–1.6	0.9	RT	50 mAh g^{-1} at 0.6 A g^{-1} (based on cathode)	NA	37 mAh g^{-1} (74%) after 1000 cycles at 0.6 A g^{-1}	[18]
α-MoO_3//CuFe-TBA	1 M H_3PO_4 in MeCN	0–1.5	0.6	RT	48 mAh g^{-1}	NA	≈21 mAh g^{-1} (≈44%) after 100 cycles	[36]
α-MoO_3//ZnFe-TBA	1 M H_3PO_4 in MeCN	0.38–1.3	0.7	RT	≈45 mAh g^{-1}	NA	≈36 mAh g^{-1} (≈80%) after 80 cycles	
α-MoO_3//CuFe-TBA	9.5 M H_3PO_4	0–1.6	1.0	RT	46 mAh g^{-1} at 5 A g^{-1}	30 mAh g^{-1} at 100 A g^{-1}	≈41 mAh g^{-1} (≈85%) after 1000 cycles at 2 A g^{-1}	[24]
				−78	≈28 mAh g^{-1} at 0.025 A g^{-1}	14 mAh g^{-1} at 0.4 A g^{-1}	≈28 mAh g^{-1} (≈100%) after 450 cycles at 0.025 A g^{-1}	
α-MoO_3//VFe-PBA	4.2 M H_2SO_4 + glucose	0–1.6	0.75	RT	62 mAh g^{-1} at 5 A g^{-1}	NA	≈50 mAh g^{-1} (≈77%) after 50 cycles at 5 A g^{-1}	[21]
α-MoO_3//VFe-PBA	4.2 M H_2SO_4 + glycerol	0–1.6	0.7	RT	51 mAh g^{-1} at 5 A g^{-1}	NA	40 mAh g^{-1} (79%) after 1000 cycles at 5 A g^{-1}	[132]
				−50	65 mAh g^{-1} at 0.1 A g^{-1}	20 mAh g^{-1} at 1 A g^{-1}	≈50 mAh g^{-1} (≈100%) after 100 cycles at 0.4 A g^{-1}	
α-MoO_3//VFe-PBA	4.2 M H_2SO_4 + PEG 400	0–1.6	0.7	RT	210 mAh g^{-1} at 5 A g^{-1} (based on anode)	NA	161 mAh g^{-1} 77% after 2000 cycles at 5 A g^{-1}	[22]
				−50	135 mAh g^{-1} at 0.25 A g^{-1}	NA	124 mAh g^{-1} (92%) after 150 cycles at 0.25 A g^{-1}	
α-MoO_3//NiFe-PBA	1 M HCl + 20 M $ZnCl_2$	0–1.2	0.8	RT	62.6 mAh g^{-1} at 0.5 A g^{-1}	15.7 mAh g^{-1} at 8 A g^{-1}	≈32 mAh g^{-1} (76.1%) after 400 cycles at 1 A g^{-1}	[119]
α-MoO_3//CuFe-TBA	H_3PO_4-based "acid -in-clay" (solid)	0–1.5	0.65	RT	32 mAh g^{-1} at 0.05 A g^{-1}	10.5 mAh g^{-1} at 16 A g^{-1}	≈20 mAh g^{-1} (≈75%) after 20000 cycles at 1 A g^{-1}	[23]
				−35	27.5 mAh g^{-1} at 0.05 A g^{-1}	≈19 mAh g^{-1} at 0.5 A g^{-1}	≈25 mAh g^{-1} (93%) after 500 cycles at 0.05 A g^{-1}	
α-MoO_3//$LiVPO_4F$	Polyphosphoric acid	0–1.3	0.9	RT	40 mAh g^{-1} at 0.047 A g^{-1}	NA	≈40 mAh g^{-1} (≈100%) after 1000 cycles at 0.047 A g^{-1}	[26]
				100	85 mAh g^{-1} at 0.047 A g^{-1}	27.2 mAh g^{-1} at 9.3 A g^{-1}	≈46 mAh g^{-1} (≈74%) after 400 cycles at 1.86 A g^{-1}	
h-MoO_3//CoFe-PBA	0.5 M H_2SO_4	0–1.6	1.0	RT	95 F g^{-1} at 2 mV s^{-1}	71 F g^{-1} at 50 mV s^{-1}	83% after 10000 cycles at 10 A g^{-1}	[62]
$Ti_3C_2T_x$//NiFe-PBA	4.5 M acetic acid	0–1.2	0.5	RT	36 mAh g^{-1} at 0.5 A g^{-1}	11 mAh g^{-1} at 5 A g^{-1}	≈31 mAh g^{-1} (≈83%) after 700 cycles at 1 A g^{-1}	[120]
PTO//VFe-PBA	4.2 M H_2SO_4	0–1.2	0.65	RT	85 mAh g^{-1} at 0.05 A g^{-1}	28 mAh g^{-1} at 37 A g^{-1}	78 mAh g^{-1} (80%) after 2000 cycles at 5 A g^{-1}	[84]
DPPZ//InFe-PBA	0.05 M H_2SO_4	0–1.5	0.7	RT	37 mAh g^{-1} at 1 A g^{-1}	30.1 mAh g^{-1} at 10 A g^{-1}	≈24 mAh g^{-1} (76.1%) after 3000 cycles at 6 A g^{-1}	[49]
α-MoO_3//CuFe-TBA	H_3PO_4 in polyoxyethylene lauryl ether surfactant	0–1.85	1	RT	≈71 mAh g^{-1} at 1 A g^{-1}	≈16 mAh g^{-1} at 100 A g^{-1}	≈36 mAh g^{-1} (87%) after 50000 cycles at 10 A g^{-1}	[56]

(*Continued*)

© 2024 The Author(s). Advanced Functional Materials published by Wiley-VCH GmbH

16163028, 2024, 40, Downloaded from https://onlinelibrary.wiley.com/doi/10.1002/adfm.202405401 by Karlsruher Institut F., Wiley Online Library on [05/11/2024]. See the Terms and Conditions (https://onlinelibrary.wiley.com/terms-and-conditions) on Wiley Online Library for rules of use; OA articles are governed by the applicable Creative Commons License

Table 1. (Continued)

Anode//Cathode	Electrolytes	Voltage [V]	Median discharge voltage [V]	Temp. [°C]	Specific capacity	Rate	Cycling performance	Refs.
α-MoO_3//CuFe-TBA	$[Zn_3(H_2PO_4)_6(H_2O)_3]$(1,2,3-benzotriazole) glass (solid)	0–0.9	0.15	110	≈30 mAh g^{-1} at 0.01 A g^{-1}	≈5 mAh g^{-1} at 0.5 A g^{-1}	76% after 1000 cycles at 0.1 A g^{-1}	[126]
Rocking-chair type all-organic proton full-cell								
PNAQ//PNAQ	4 M H_2SO_4	0.1–1.2	0.5	RT	118.7 mAh g^{-1} at 0.12 A g^{-1} (based on cathode)	77 mAh g^{-1} at 12 A g^{-1}	≈70 mAh g^{-1} (70%) after 500 cycles at 6 A g^{-1}	[96]
				−70	≈67 mAh g^{-1} at 0.12 A g^{-1} (based on cathode)	55.1 mAh g^{-1} at 2.4 A g^{-1}	≈53 mAh g^{-1} (≈100%) after 200 cycles at 1.2 A g^{-1}	
AQ//TCBQ	0.5 M H_2SO_4	0–1.4	0.6	RT	≈60 mAh g^{-1} at 0.045 A g^{-1}	≈18 mAh g^{-1} at 4.5 A g^{-1}	≈69% after 500 cycles at 0.225 A g^{-1}	[15]
DHN-rGO//DHAQ	PVA-H_2SO_4-sol gel	0–1.2	0.55	RT	83 mAh g^{-1} at 1 A g^{-1}	42 mAh g^{-1} at 10 A g^{-1}	≈38 mAh g^{-1} (71%) after 1000 cycles at 5 A g^{-1}	[102]
TPAD-COF//AQ	1.2 M H_2SO_4	0–1.4	0.35	RT	111 mAh g^{-1} at 0.5 A g^{-1}	≈36 mAh g^{-1} at 6 A g^{-1}	≈56 mAh g^{-1} (74%) after 1000 cycles at 2 A g^{-1}	[149]
				−20	≈70 mAh g^{-1} at 0.5 A g^{-1}	≈15 mAh g^{-1} at 6 A g^{-1}	≈30 mAh g^{-1} (≈100%) after 1000 cycles at 2 A g^{-1}	
pDTP-AQ//pDTP-NQ	1 M H_2SO_4	0–0.9	0.4	RT	78 mAh g^{-1} at 0.5 A g^{-1}	39 mAh g^{-1} at 20 A g^{-1}	≈42 mAh g^{-1} (56%) after 2000 cycles at 1 A g^{-1}	[87]
PUQ//PTC	0.5 M H_2SO_4	0–1.2	0.55	RT	78.1 mAh g^{-1} at 0.5 A g^{-1} (based on one electrode)	50.8 mAh g^{-1} at 25 A g^{-1}	≈50 mAh g^{-1} (80%) after 1000 cycles at 2 A g^{-1}	[88]
pEP(NQ)E//pEP(QH_2)E	0.5 M H_2SO_4	0.2–0.6	0.35	RT	≈60 mAh g^{-1} at 0.165 A g^{-1} (based on anode)	20 mAh g^{-1} at 5.5 A g^{-1}	51 mAh g^{-1} (85%) after 500 cycles at 0.165 A g^{-1}	[90]
	3.3 M H_2SO_4	0.1–0.6	0.3	−24	≈52 mAh g^{-1} at 0.165 A g^{-1} (based on anode)	40 mAh g^{-1} at 3 A g^{-1}	≈51 mAh g^{-1} (98%) after 500 cycles at 0.165 A g^{-1}	
P-AS//AN-PA	2 M HCl	0–1.1	0.4	RT	80 mAh g^{-1} at 1 A g^{-1} (based on anode)	51 mAh g^{-1} at 10 A g^{-1}	≈64 mAh g^{-1} (86%) after 1000 cycles at 2 A g^{-1}	[93]
				−25	≈68 mAh g^{-1} at 2 A g^{-1} (based on anode)	NA	≈57 mAh g^{-1} (84%) after 1000 cycles at 2 A g^{-1}	
Poly(NQ-EPE)//poly(QzH_2-EPE)	MeTriHTFSI protic ionic liquid	0.5–0.9	0.75	RT	≈60 mAh g^{-1} at 0.3 A g^{-1} (based on anode)	NA	≈50 mAh g^{-1} (≈83%) after 500 cycles at 0.3 A g^{-1}	[123]
Hybrid-type electrolytic proton full-cell								
α-MoO_3//MnO_2 @ carbon felt	2 M H_2SO_4 + 2 M $MnSO_4$	0.85–1.55	1.05	RT	209.6 mAh g^{-1} at 1 A g^{-1} (based on anode)	103 mAh g^{-1} at 60 A g^{-1}	≈150 mAh g^{-1} (81%) after 300 cycles at 4 A g^{-1}	[25]
				−70	171.8 mAh g^{-1} at 0.1 A g^{-1} (based on anode)	≈120 mAh g^{-1} at 0.5 A g^{-1}	≈165 mAh g^{-1} (≈100%) after 100 cycles at 0.2 A g^{-1}	
α-MoO_3//MnO_2 @ carbon felt	2 M H_2SO_4 + 2 M $MnSO_4$ colloid electrolyte	0.8–1.6	1.1	RT	≈200 mAh g^{-1} at 3 A g^{-1} (based on anode)	NA	≈50 mAh g^{-1} (≈25%) after 10000 cycles at 3 A g^{-1}	[37]
Al-MoO_3//MnO_2 @ carbon foil	2 M $AlCl_3$ // 2 M $MnSO_4$ + H_2SO_4	1.0–1.8	1.35	RT	145 mAh g^{-1} at 0.17 A g^{-1} (based on anode)	60.4 mAh g^{-1} at 13.3 A g^{-1}	≈130 mAh g^{-1} (91.3%) after 1000 cycles at 3.3 A g^{-1}	[167]
α-MoO_3 (core) @ TiO_2 (shell)//MnO_2 @ carbon cloth	1 M H_2SO_4 + 1 M $MnSO_4$	0.85–1.6	1.0	RT	200.8 mAh g^{-1} at 1 A g^{-1} (based on anode)	116.3 mAh g^{-1} at 20 A g^{-1}	160.7 mAh g^{-1} (80%) after 500 cycles at 10 A g^{-1}	[59]

(*Continued*)

© 2024 The Author(s). Advanced Functional Materials published by Wiley-VCH GmbH

16163028, 2024, 40, Downloaded from https://onlinelibrary.wiley.com/doi/10.1002/adfm.202405401 by Karlsruher Institut F., Wiley Online Library on [05/11/2024]. See the Terms and Conditions (https://onlinelibrary.wiley.com/terms-and-conditions) on Wiley Online Library for rules of use; OA articles are governed by the applicable Creative Commons License

Table 1. (Continued)

Anode//Cathode	Electrolytes	Voltage [V]	Median discharge voltage [V]	Temp. [°C]	Specific capacity	Rate	Cycling performance	Refs.
TMBQ @ rGO foam//MnO2 @ carbon felt-CNT	0.5 M H_2SO_4 + 1 M $MnSO_4$	0.3–1.3	0.8	RT	320 mAh g^{-1} at ≈0.33 A g^{-1} (based on anode)	148 mAh g^{-1} at 32.6 A g^{-1}	≈200 mAh g^{-1} (77%) after 4000 cycles at 1.63 A g^{-1}	[40]
PTO//MnO_2 @ carbon felt	2 M H_2SO_4 + 2 M $MnSO_4$ colloid electrolyte	0.3–1.3	0.85	RT	≈225 mAh g^{-1} at 0.5 A g^{-1} (based on anode)	NA	≈105 mAh g^{-1} (≈47%) after 21200 cycles at 0.5 A g^{-1}	[37]
PTO//MnO_2 @ carbon felt	2 M H_2SO_4 + 2 M $MnSO_4$	0.3–1.3	0.8	RT	210 mAh g^{-1} at 0.04 A g^{-1} (based on anode)	66 mAh g^{-1} at 100 A g^{-1}	≈105 mAh g^{-1} (≈60%) after 5000 cycles at 0.5 A g^{-1}	[83]
				−70	110 mAh g^{-1} at 0.04 A g^{-1} (based on anode)	89 mAh g^{-1} at 0.5 A g^{-1}	≈100 mAh g^{-1} (> 99%) after 100 cycles at 0.2 A g^{-1}	
ALO//MnO_2 @ carbon felt	2 M HBF_4 + 2 M $Mn(BF_4)_2$	0.4–1.5	1.15	RT	145.5 mAh g^{-1} at 1 A g^{-1} (based on anode)	≈130 mAh g^{-1} at 25 A g^{-1}	≈100 mAh g^{-1} (≈67%) after 300 cycles at 5 A g^{-1}	[97]
				−60	≈130 mAh g^{-1} at 0.125 A g^{-1}	100 mAh g^{-1} at 1.5 A g^{-1}	≈105 mAh g^{-1} (≈100%) after 500 cycles at 1 A g^{-1}	
DHAQ//MnO_2 @ carbon felt	1 M H_2SO_4 + 0.5 M $MnSO_4$	0.2–1.6	1.15	RT	≈150 mAh g^{-1} at 0.63 A g^{-1} (based on anode)	≈105 mAh g^{-1} at 1.13 A g^{-1}	65 mAh g^{-1} (≈60%) after 2600 cycles at 1.13 A g^{-1}	[89]
NTCDA-PI//MnO_2 @ carbon felt	2 M H_2SO_4 + 2 M $MnSO_4$	0.5–1.7	1.3	RT	77 mAh g^{-1} at 1 A g^{-1} (based on anode)	27.7 mAh g^{-1} at 100 A g^{-1}	≈45 mAh g^{-1} (67.9%) after 5000 cycles at 5 A g^{-1}	[91]
HATN//MnO_2 @ carbon cloth	0.05 M H_2SO_4 + 0.2 M $MnSO_4$	0.4–1.4	1.0	RT	260 mAh g^{-1} at 0.1 A g^{-1} (based on anode)	145 mAh g^{-1} at 5 A g^{-1}	190 mAh g^{-1} (92.7%) after 500 cycles at 1 A g^{-1}	[94]
HATN//MnO_2 @ carbon felt	2 M H_2SO_4 + 2 M $MnSO_4$	0.55–1.35	1.05	RT	266 mAh g^{-1} at 0.5 A g^{-1} (based on anode)	97 mAh g^{-1} at 50 A g^{-1}	≈150 mAh g^{-1} (≈57%) after 7000 cycles at 5 A g^{-1}	[103]
Pb//TCBQ @ rGO foam	5 M H_2SO_4	0.6–1.4	1.05	RT	208 mAh g^{-1} at 0.2 A g^{-1} (based on cathode)	84 mAh g^{-1} at 100 A g^{-1}	106 mAh g^{-1} (≈62%) after 3000 cycles at 10 A g^{-1}	[41]
				−70	87 mAh g^{-1} at 0.1 A g^{-1} (based on cathode)	≈20 mAh g^{-1} at 5 A g^{-1}	≈50 mAh g^{-1} (≈97%) after 500 cycles at 0.5 A g^{-1}	
Active carbon// HDC	PVA-H_2SO_4-sol gel	−0.3–0.75	0.2	RT	50 mAh g^{-1} at 0.1 A g^{-1}	32 mAh g^{-1} at 1 A g^{-1}	≈36 mAh g^{-1} (98.9%) after 600 cycles at 0.5 A g^{-1}	[95]
Hybrid-type electrolytic proton-gas full-cells								
H_2//TCBQ	5 M H_2SO_4	0.1–1	0.65	RT	≈175 mAh g^{-1} at 2 A g^{-1} (based on cathode)	≈72 mAh g^{-1} at 100 A g^{-1}	154.9 mAh g^{-1} (≈100%) after 30 000 cycles at 50 A g^{-1}	[114]
H_2//CuFe-TBA	9 M H_3PO_4	0.5–1.2	0.85	RT	52 mAh g^{-1} at 0.5 A g^{-1} (based on cathode)	35.9 mAh g^{-1} at 48 A g^{-1}	≈23 mAh g^{-1} (62%) after 350 000 cycles at 48 A g^{-1}	[136]

(*Continued*)

© 2024 The Author(s). Advanced Functional Materials published by Wiley-VCH GmbH

16163028, 2024, 40, Downloaded from https://onlinelibrary.wiley.com/doi/10.1002/adfm.202405401 by Karlsruher Institut F., Wiley Online Library on [05/11/2024]. See the Terms and Conditions (https://onlinelibrary.wiley.com/terms-and-conditions) on Wiley Online Library for rules of use; OA articles are governed by the applicable Creative Commons License

Table 1. (Continued)

Anode//Cathode	Electrolytes	Voltage [V]	Median discharge voltage [V]	Temp. [°C]	Specific capacity	Rate	Cycling performance	Refs.
				−60	≈40 mAh g^{-1} at 0.05 A g^{-1} (based on cathode)	≈18 mAh g^{-1} at 1 A g^{-1}	≈32.5 mAh g^{-1} (≈96%) after 1150 cycles at 0.25 A g^{-1}	
H_2//Active carbon	9 M H_3PO_4	0–1.2	0.5	RT	295 F g^{-1} at 1 A g^{-1} (based on cathode)	141 F g^{-1} at 30 A g^{-1}	≈135 F g^{-1} (87.5%) after 50 000 cycles at 20 g^{-1}	[168]
				−20	139 F g^{-1} at 1 A g^{-1}	≈90 F g^{-1} at 10 A g^{-1}	≈117 F g^{-1} (100%) after 10 000 cycles at 4 g^{-1}	
Hybrid-type proton-metal full-cells								
Zn// α-MoO_3	32 M $ZnCl_2$ + 1 M P_2O_5	0.45–1.1	0.95	RT	≈290 mAh g^{-1} at 1 A g^{-1} (based on cathode)	≈180 mAh g^{-1} at 16 A g^{-1}	≈270 mAh g^{-1} (98%) after 1000 cycles at 2 A g^{-1}	[125]
Zn//HBOSs	3 M $Zn(OTf)_2$	0.5–1.5	0.8	RT	298 mAh g^{-1} at 2 A g^{-1} (based on cathode)	135 mAh g^{-1} at 150 A g^{-1}	≈180 mAh g^{-1} (92.3%) after 50000 cycles at 2 A g^{-1}	[20]
Zn//TABQ	1 M $ZnSO_4$	0.4–1.3	0.85	RT	303 mAh g^{-1} at 0.1 A g^{-1} (based on cathode)	213 mAh g^{-1} at 5 A g^{-1}	≈200 mAh g^{-1} (≈83%) after 1000 cycles at 5 A g^{-1}	[98]
Zn//HATN	2 M $ZnSO_4$	0.3–1.1	0.5	RT	405 mAh g^{-1} at 0.1 A g^{-1} (based on cathode)	123 mAh g^{-1} at 20 A g^{-1}	≈140 mAh g^{-1} (93.3%) after 5000 cycles at 5 A g^{-1}	[104]
Al//V_2O_5	2 M $Al(OTf)_3$	0.25–1.7	0.9	RT	186 mAh g^{-1} at 0.04 A g^{-1} (based on cathode)	NA	120 mAh g^{-1} (64.5%) after 50 cycles at 0.04 A g^{-1}	[69]

decomposition or undesirable side reactions. The ESW is one key factor in accommodating redox couples of suitable electrode potentials and determining the voltage- and energy-output of electrochemical devices. Constrained by the water decomposition limit of 1.23 V, the ESW for common aqueous electrolytes (salt-in-water solutions) is typically restricted to less than 2 V.[2] In the context of proton batteries where relatively concentrated aqueous acids are often utilized, the ESW can be somewhat higher such as reaching 2.6 V for 4.2 M H_2SO_4.[21] Despite the advantage over many other aqueous energy storage, there are still gaps compared to the non-aqueous systems, and expanding the ESW of proton electrolytes can make a difference. A good example is the discovery of additional redox pair of α-MoO_3, benefitting an expanded ESW by a liquid crystal electrolyte.[56]

3.2.3. Gassing Issue

Gas evolution reactions, i.e., hydrogen evolution reaction (HER) and oxygen evolution reaction (OER), can be easily triggered because of the narrow ESW of current main-stream aqueous acid electrolytes. The gas evolutions also lead to gassing problems, which potentially cause expansion in the sealed cell, pack, and device, thereby raising significant safety concerns. Particularly, HER represents a significant competitive side effect ($H^+ \leftrightarrow H\cdot \leftrightarrow H_2$) in proton intercalation reactions, typically occurring at low electrode potential near HER limit.[17] While recent observations have identified noticeable bubble generation at the surface of a proton cathode operating at high electrode potentials.[23] These observations further amplify the aforementioned concerns.

3.3. Improvement Strategies

As discussed in the aforementioned paragraphs, the solvent water in electrolytes significantly contributes to these challenges. Therefore, the key to improvements is centered on tuning the role of water molecules in bulk electrolytes, such as modifying the water solvation structure in electrolytes and/or altering the physical state of the electrolytes, as illustrated in Figure 10b–e.

Reducing the water fraction in electrolytes is a common strategy to modulate the ion-water solvation structure, thereby mitigating these discussed challenges and enhancing overall electrochemical performances. The simplest way is to increase the concentration of acid electrolytes. For example, concentrated H_2SO_4 (>4 M) electrolyte delivers much-enhanced cycling stability of MoO_3 electrodes with ≈75% capacity retention over 200 cycles, superior to diluted ones (≈40% capacity retention with <2 M H_2SO_4).[17] However, this also raises corrosion concerns to other battery components. Competing solvation agents have then been developed as alternative strategies to regulate the ion-water solvation structure. A "water-in-sugar" electrolyte has been proposed by Zhao group, achieving extended ESW and improving the cycling performance of proton anodes.[21] Spectroscopies and molecular dynamics (MD) simulations reveal that water molecules are locked-up by sugar additives via hydrogen bonding and therefore reduce the fraction of free water molecules and their activities (Figure 10b,c). However, the adaptability of

© 2024 The Author(s). Advanced Functional Materials published by Wiley-VCH GmbH
RIGHTSLINK

16163028, 2024, 40, Downloaded from https://onlinelibrary.wiley.com/doi/10.1002/adfm.202405401 by Karlsruher Institut F., Wiley Online Library on [05/11/2024]. See the Terms and Conditions (https://onlinelibrary.wiley.com/terms-and-conditions) on Wiley Online Library for rules of use; OA articles are governed by the applicable Creative Commons License

16163028, 2024, 40, Downloaded from https://onlinelibrary.wiley.com/doi/10.1002/adfm.202405401 by Karlsruher Institut F., Wiley Online Library on [05/11/2024]. See the Terms and Conditions (https://onlinelibrary.wiley.com/terms-and-conditions) on Wiley Online Library for rules of use; OA articles are governed by the applicable Creative Commons License

such solid additives can be limited by their solubility, later development of water-immiscible competing solvation agents such as polyethylene glycol,[22] glycerol,[132] and polyoxyethylene lauryl ether[56] (a surfactant) have been successively introduced, demonstrating better tunability regarding water content. Other strategies including replacing non-aqueous solvent[36] and even directly applying solvent-free protic liquid as proton electrolytes were also introduced to eliminate the negative influence of free water molecules.[26]

Modifying the physical states of the electrolyte is a highly effective measure from a different perspective, leading to variations in proton-molecule coordination[56,121] (Figure 10d) and therefore alleviating the aforementioned challenges. Similar to the situations in aqueous solutions, protons showcase high mobility in ice through Grotthuss-type conduction along the hydrogen-bond network of an ice crystal, which enables decent electrochemical performances at non-liquid states.[135] Proton electrodes (α-MoO_3[25] and PTO[83]) demonstrate considerable cycling stability with negligible capacity decay in the "transition-state solid" (ice) electrolytes, due to the reduced water activity in the system. Additionally, it is noteworthy that adopting solid-state electrolytes proves particularly effective in mitigating the gassing problem. An "acid-in-clay" electrolyte has been demonstrated to significantly alleviate intrinsic gas evolutions on both sides of proton electrodes.[23]

4. Full-Cell Proton Batteries

As outlined in the very beginning, proton batteries refer to the energy storage systems where proton/hydronium ions serve as the ion-charge carrier(s) to initiate and facilitate electrode reactions.[10] Early techniques can be traced back to the classic lead-acid batteries, which have continued to evolve and maintain widespread application till now. Recent advancements in faradaic electrodes and electrolytes have propelled the development of electrochemical proton storage systems. Various proton full-cells or devices have been constructed to showcase their application potential, although commercialization from laboratory demonstrations remains a significant challenge. Following the introductions of electrodes and electrolytes, developments for the fabrication of correlated full-cells and devices are discussed herein. First, the classifications of proton batteries are briefly outlined, encompassing proton rocking-chair batteries/supercapacitors and hybrid proton batteries. Additionally, the corresponding cell configurations and their limitations are also addressed.

4.1. Classifications and Cell-Configurations

In the current literature, proton batteries are primarily classified into two categories: proton rocking-chair batteries/supercapacitors and hybrid proton batteries (or electrolytic proton batteries), based on the origin of their redox reactions, as shown in **Figure 11**. In proton rocking-chair designs, both electrodes depend on proton-accessible reactions/interactions for charge compensation, such as proton intercalation reactions, proton surface (pseudocapacitive) reactions, and ion adsorption (notably, counter anions may also participate). These batteries effectively leverage the fast kinetics feature of proton conduction. However, they are challenged by the limited energy output due to the specific capacity mismatch (more active material loading) and limited potential difference (lower voltage output) between two electrodes. This further triggers the adoption of electrolytic reactions as the counter-reactions to overcome these issues. In the case of hybrid proton batteries, at least one electrode undergoes a redox reaction that accommodates proton-rich environments but does not rely on proton-specific reactions. Hybrid proton batteries that integrate Mn-based and Pb-based conversion reactions have been successively developed with superior performances. Moreover, other specific electrolytic reactions, such as metal deposition/dissolution and gas evolution/consumption (Figure 11) also emerged as electrode reactions, corresponding to proton-metal batteries[103,125] and proton-gas batteries[114,136] respectively. Representative designs of proton batteries and their correlated electrochemical performances are summarized in **Table 1**.

Throughout the currently reported proton batteries, the majority normally adopt the cell configurations for their electrode evaluations for simplicity reasons, such as the demonstrative cells in beaker type, Swagelok type and coin-cell type. The physical characteristics of electrodes and electrolytes play a pivotal role in determining the battery configurations, and the adoption of gas-involved electrodes and quasi-solid (hydrogel) electrolytes facilitates the utilization of gas-sealing reactors[114,136] and the fabrication of flexible cells,[92] respectively. Moreover, scaled-up proton batteries have also been reported with the fabrications of pouch cells[23] and cylindrical cells,[42] and one possibility for addressing detrimental gassing issues has been investigated using a solid-state electrolyte in a pouch cell.[23]

4.2. Proton Rocking-Chair Batteries/Supercapacitors

Rocking-chair-type batteries, the main form of ubiquitous lithium-ion batteries, are characterized by the reversible movement of charge carriers between the anodes and cathodes during charging and discharging. In the context of proton batteries, Grotthuss proton conduction supports rapid movement of charge carriers between the two electrodes, thereby enabling fast charging of batteries and enhanced power density. The electrodes typically undergo intercalation/deintercalation reactions, involving the insertion/extraction of ions into/from the electrode materials without significant structural or compositional change.[137] Additionally, electrodes based on proton surface reactions and adsorptions are also employed, as indicated in Figure 11. The corresponding full cells can therefore sometimes exhibit as (pseudo-) supercapacitors, while these cells are also referred to as batteries herein for simplicity.

A rocking-chair proton battery can be fabricated by pairing two aforementioned protonic electrodes, provided there are applicable electrode potential gaps. For instance, possessing relatively high electrode potentials and good capacities, PBA materials are popular choices as protonic cathodes and have been coupled with various anode materials such as organic compounds[84] and transition metal oxides,[18,132] etc. Ji group first discovered the diffusion-free Grotthuss topochemistry in PBA materials, and demonstrated a proof-of-concept rocking-chair proton

© 2024 The Author(s). Advanced Functional Materials published by Wiley-VCH GmbH
RIGHTSLINK

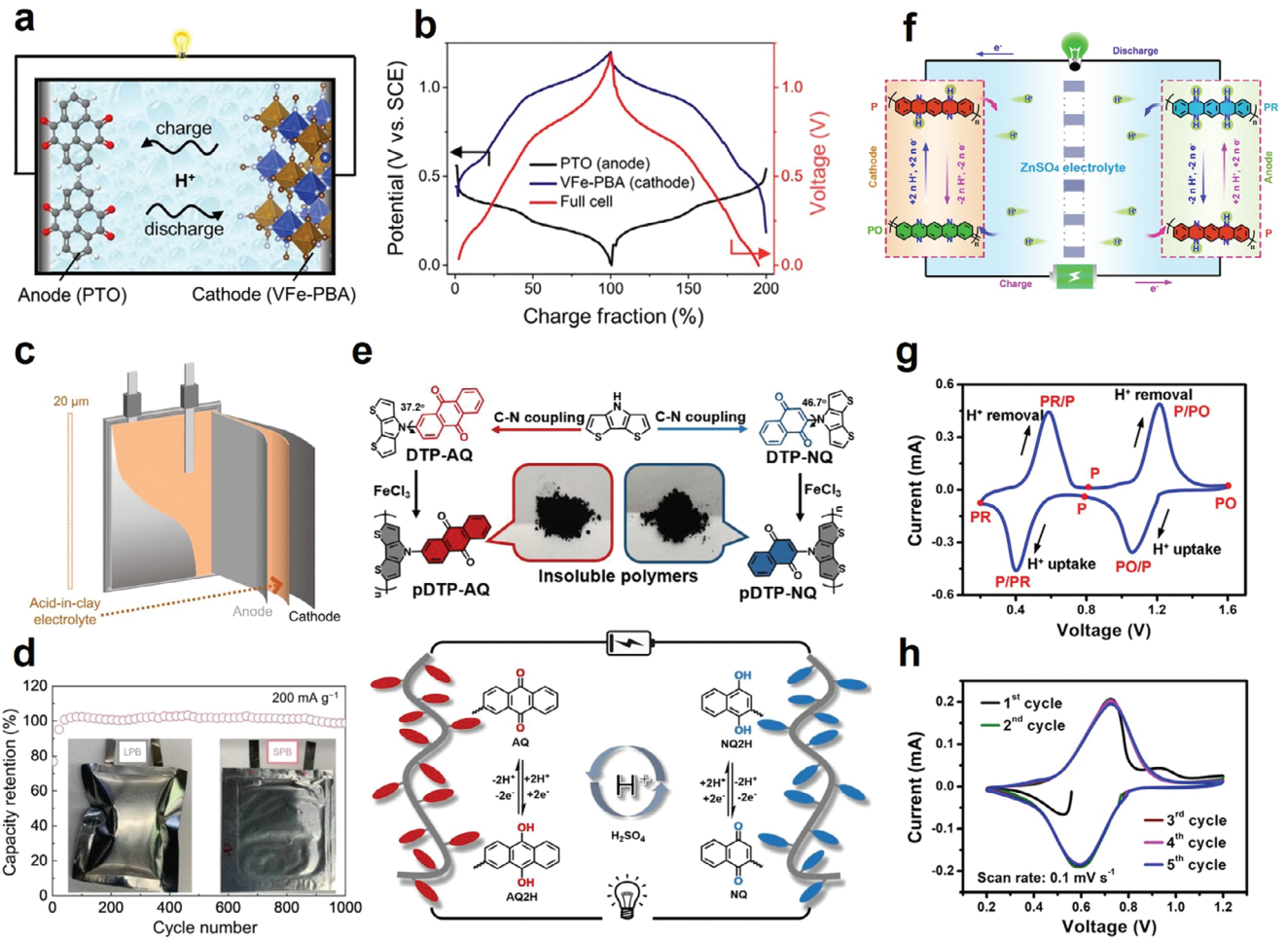

Figure 12. Illustration of proton rocking-chair batteries. a) Schematic diagram and b) voltage profiles of PTO//VFe-PBA full-cell. Reproduced with permission.[84] c) Schematic diagram of acid-in-clay electrolyte and d) cycling performance of MoO_3//CuFe-TBA pouch-cell using acid-in-clay electrolyte at 0.2 A g^{-1}, inset photographs highlight the inhabitation effect of gassing issue. Reproduced with permission.[23] e) Schematic diagram of the design and energy storage mechanism of pDTP-AQ//pDTP-NQ all-organic proton full-cell. Reproduced with permission.[87] f) Schematic diagram of PO//PO symmetric all-organic proton full-cell and CV profile of g) PO half-cell and h) PO//PO full-cell respectively. Reproduced with permission.[139]

battery based on WO_3 and CuFe-TBA in 2 M H_2SO_4.[18] Su et al. introduced a rocking-chair battery employing PTO anode and VFe-PBA cathode in 4.2 M H_2SO_4 (**Figure 12a**).[84] Figure 12b demonstrates the GCD profile of the full-cell in a voltage window of 0–1.2 V, showing two plateaus at 0.2 V and 0.8 V respectively. PTO//VFe-PBA cell presents a high capacity of ≈85 mAh g^{-1} at 0.05 A g^{-1}. Due to the unique Grotthuss proton conduction in both electrolyte and electrode, the full-cell exhibits high-rate performance, and 33% capacity is retained at a high current density of 37 A g^{-1}, achieving fast charging in seconds. An α-MoO_3//CuFe-TBA full-cell was further demonstrated by Ji group with pouch cell configurations. A less chemically corrosive acid (H_3PO_4) was employed at a higher concentration of 9.5 M, supporting stable cycling performance at both room temperature and ultralow temperature of −78 °C.[24]

Cycling stability poses a significant challenge in full-cell configurations. Unlike half-cells where charge compensation is unlimited, in full-cells with fixed proton inventory, any insufficient charge compensation resulting from imperfect electrochemical reactions such as side reactions or materials dissolution will accumulate over time, leading to rapid capacity fading.[138] In this context, it is crucial to address these issues in full-cell configurations to enhance cycling stability. Various electrolyte regulation strategies including H-bond disrupting electrolytes,[132] molecular crowding electrolytes,[22] and water-in-salt electrolytes[119] have been identified to significantly enhance the cycling performance of aqueous proton batteries compared with plain aqueous acid electrolytes. These enhancements are attributed to the altering of water solvation structure and reduction of free water that are beneficial for individual electrode stability. In particular, the molecular crowding electrolyte demonstrated the ability to improve the cyclability of α-MoO_3//VFe-PBA proton full-cell to over 2000 cycles. In another instance, Li and co-workers showcased a stable α-MoO_3//CuFe-TBA device utilizing the acid-in-clay electrolyte.[23] Thanks to the unique mechanical properties of solid acid-in-clay electrolytes, the pouch-cell can be assembled into a thin-film form, featuring a micrometer-level electrolyte thickness as depicted in Figure 12c. The

© 2024 The Author(s). Advanced Functional Materials published by Wiley-VCH GmbH

16163028, 2024, 40, Downloaded from https://onlinelibrary.wiley.com/doi/10.1002/adfm.202405401 by Karlsruher Institut F., Wiley Online Library on [05/11/2024]. See the Terms and Conditions (https://onlinelibrary.wiley.com/terms-and-conditions) on Wiley Online Library for rules of use; OA articles are governed by the applicable Creative Commons License

as-assembled full-cell shows excellent cycling performance at both room temperature and low temperature. In comparison to traditional acid electrolytes, the acid-in-clay electrolyte possesses an expanded ESW and imposes less corrosion to battery components. As highlighted in Figure 12d, this results in significantly suppressed gassing issues during battery cycling with acid-in-clay electrolytes, contributing to high safety in practical applications.

All-Organic Proton Rocking-Chair Batteries: Exploring rocking-chair batteries utilizing organic materials for both cathode and anode emerges as a research hotspot, offering a promising avenue for the development of cost-effective, metal-free energy storage systems. This concept can be actualized by incorporating two proton-active organic electrodes with distinct potential differences. Zhao et al. proposed an all-organic aqueous proton battery using two organic monomer electrodes, which are 2,6-dihydroxynaphalene (DNH) cathode and 2,6-dihydroxyanthraquione (DHAQ) anode.[102] The as-assembled cell delivered a high output voltage of 0.85 V, achieving considerable cycling stability (71% capacity retention) over 1000 cycles. Organic polymers have also been introduced for full-cell applications, allowing the redox potentials of polymer-based electrodes to be tuned by incorporating different pendants with different energies. Tang group established an all-polymer proton battery by grafting poly(dithieno[3,2-b:2′,3′-d]pyrrole (pDTP) backbones with redox-active pendants (anthraquinone, AQ; naphthoquinone, NQ) at different energy levels, as shown in Figure 12e.[87] The two pendants exhibit fast redox behaviors facilitated by intermolecular electron transfer via the π-conjugated polymer backbone. The assembled polymer-type full-cell demonstrates excellent rate performances (50% capacity retention at 20 A g^{-1}) and considerable cycling performance (56% capacity retention over 2000 cycles).

It is noteworthy that certain electrode materials possess more than one redox pair at different potentials, allowing them to theoretically serve as both cathode and anode simultaneously. Batteries assembled with such materials are termed as symmetric batteries. From a commercial perspective, symmetric batteries are appealing due to a simplified fabrication process and reduced manufacturing costs resulting from the usage of only one type of electrode.[140] Organic materials with multiple redox pairs and substantial energy gaps for proton (de)intercalation are promising candidates for symmetric proton batteries. Tie et al. introduced a poly(2,9-dihydroquinoxalino[2,3-b]phenazine) (PO) molecule for a symmetric all-organic proton battery.[139] As shown in Figure 12f,g, in a mild $ZnSO_4$ electrolyte, PO undergoes a two-step, two-electron proton uptake/removal reaction, displaying a significant potential difference due to the large energy gap between PO and its protonation products. The PO//PO full-cell achieves an output voltage of ≈0.7 V (Figure 12h) and superior cycling stability (94% capacity retention over 500 cycles). The full-cell was also evaluated in a pouch-cell setup, demonstrating excellent cycling stability for up to 200 cycles.

Rocking-chair-type proton full-cells, relying on proton shuttling between the electrodes, are anticipated to best leverage the fast conduction feature of proton charge carriers to achieve high-rate performance. It is important to consider the N/P ratio (mass ratio of negative electrode over positive electrode) to balance the charge compensation between the electrodes. Sometimes, high mass loading of one electrode is necessary, if the counter electrode adopted exhibits a higher specific capacity, e.g., the N/P ratio of α-MoO_3//VFe-PBA can be around 1:2. Moreover, in rocking-chair configurations, the cathode materials need to hold proton before being assembled into full cells. However, many reported electrode materials (e.g. PBAs) do not inherently contain protons, making them unable to directly pair with proton-deficient anodes in full-cells.[7] A preactivation treatment via either chemical[18] or electrochemical[22] process is therefore necessary to introduce protons into cathode materials. All-organic proton batteries offer unique advantages of sustainability and low cost due to their metal-free composition. However, these batteries face challenges such as low volumetric capacity, resulting from the low tap density and the extensive use of conductive agents in organic electrodes. Additionally, the energy gaps between organic electrodes are much narrower compared to those in metal-containing inorganic electrodes, leading to limited output voltages and energy densities.

4.3. Hybrid Proton Batteries

In the hybrid designs of proton batteries, there is normally one electrode involving proton (de)intercalation, paired with another electrode associated with non-proton-specific reactions. These non-proton-specific reactions are typically based on electrolytic redox pairs (e.g. $PbSO_4$/Pb,[41,85] PbO_2/Pb,[16] and Mn^{2+}/MnO_2[25,37,40,83] conversions). Consequently, the term hybrid proton batteries is also known as electrolytic proton batteries, and in some special cases, both electrodes rely on electrolytic reactions as seen in the famous lead-acid batteries. These electrolytic reactions usually take place at fixed electrode potentials, either much lower or higher than those of protonic electrodes (e.g. 1.23 V vs SHE for MnO_2/Mn^{2+}[37] and -0.35V vs SHE for $PbSO_4$/Pb,[41] while average 0.84 V vs SHE for CuFe-PBA[18]), leading to significantly elevated output voltage in full-cells. Considering the mediocre operation potential range of organic electrodes (e.g. −0.2 – 0.5 V vs SHE), matching organic electrodes with electrolytic redox pairs has vital significance in elevating the output voltage of organic compound-based proton batteries. Furthermore, as no dedicated electrode material preparation is required nor there is no cycling material loss, the electrolytic proton batteries show great promise in terms of operation and sustainability. Various electrolytic proton batteries have been developed.

4.3.1. Manganese Electrolysis Based

MnO_2/ Mn^{2+} conversion reactions, have been applied as the most commonly used counter redox pairs for organic materials due to their high operation potentials.[40,83,89,91,97,103] For example, Guo et al. matched PTO anode with MnO_2/ Mn^{2+} redox pairs to build a hybrid-type proton full-cell (**Figure 13a**).[83] A hybrid electrolyte of 2.0 M H_2SO_4 and 2.0 M $MnSO_4$ was employed to provide both proton and Mn^{2+} ions for battery reactions (Mn^{2+} + $6H_2O$ ↔ MnO_2 + $4H_3O^+$ + $2e^-$; PTO + $2e^-$ + $2H_3O^+$ ↔ PTO-2H + $2H_2O$). The PTO//MnO_2 full-cell exhibits an average output voltage of ≈0.8 V as shown in Figure 13b, higher than that of the rocking-chair cell of PTO//VFe-PBA (0.6 V), thanks to the high redox

© 2024 The Author(s). Advanced Functional Materials published by Wiley-VCH GmbH
RIGHTSLINK
16163028, 2024, 40, Downloaded from https://onlinelibrary.wiley.com/doi/10.1002/adfm.202405401 by Karlsruher Institut F., Wiley Online Library on [05/11/2024]. See the Terms and Conditions (https://onlinelibrary.wiley.com/terms-and-conditions) on Wiley Online Library for rules of use; OA articles are governed by the applicable Creative Commons License

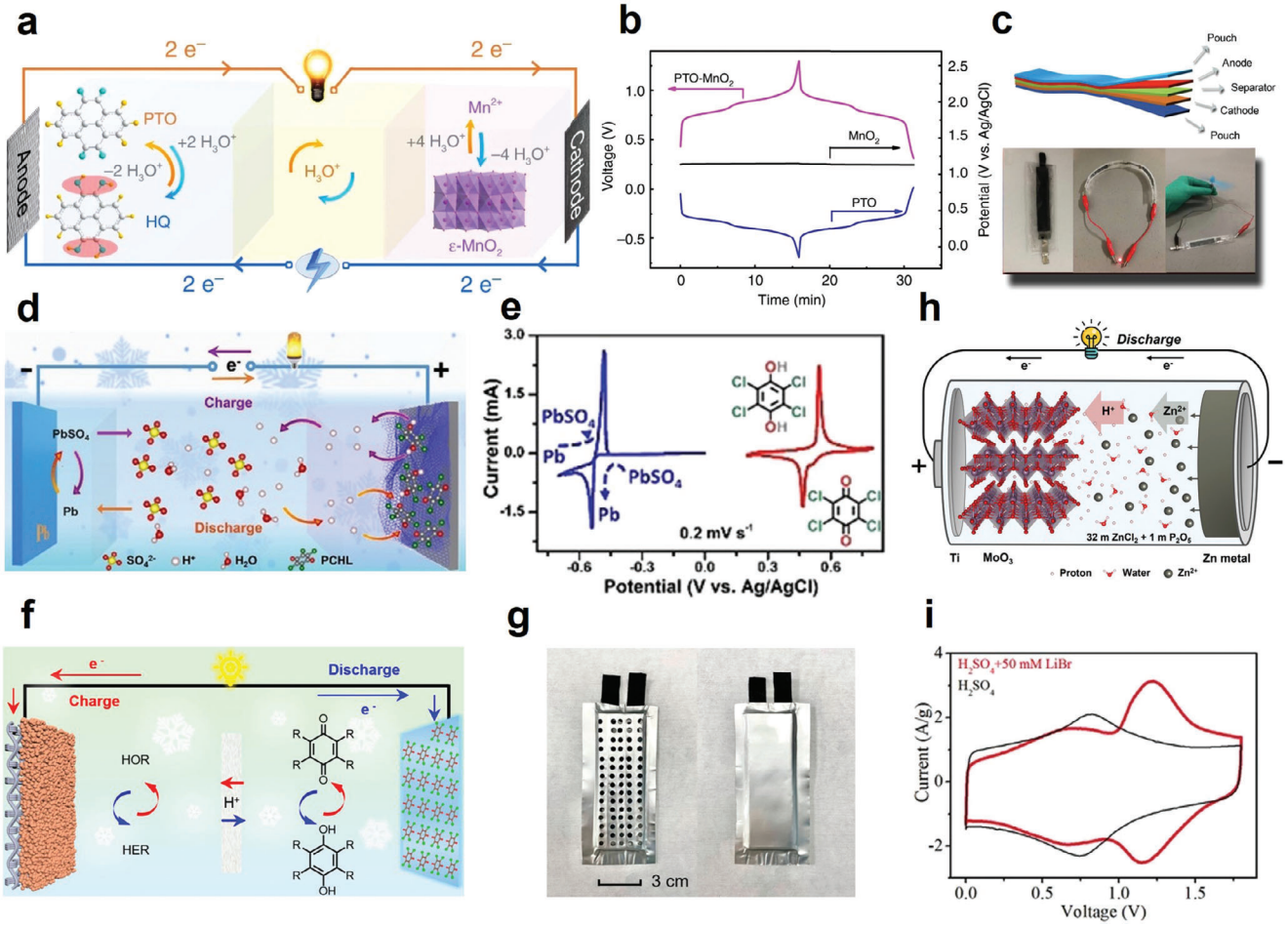

Figure 13. Illustrations of hybrid-type proton full-cells. a) Working mechanisms and b) voltage profiles of PTO//MnO_2 full-cell. c) Illustration (top) and photographs (bottom) of a flexible belt-shaped PTO//MnO_2 full-cell device. Reproduced with permission.[83] d) Working mechanisms of Pb//TCBQ proton full-cell and e) CV profiles of Pb anode and TCBQ cathodes in 5 M H_2SO_4 electrolyte. Reproduced with permission.[41] f) Schematic illustration and g) photographs of H_2//TCBQ proton full-cell. Reproduced with permission.[114] h) Schematic illustration of Zn//α-MoO_3 full-cell. Reproduced with permission.[125] i) The CV curves of $Ti_3C_2T_x$//rGO supercapacitor in H_2SO_4 electrolyte with or without Br_3^-/Br^- redox additive. Reproduced with permission.[116]

potential of MnO_2/Mn^{2+} redox pairs. The authors further demonstrated a flexible belt-shaped device with stable cycling stability over 1000 cycles (Figure 13c). In theory, in the charging process of MnO_2-based batteries, Mn^{2+} in the electrolyte oxidizes into MnO_2 and deposits on the substrate, while the resulted MnO_2 deposition reversibly dissolves into the electrolyte in the discharging process. However, the Coulombic efficiency of manganese electrolysis is often not that high in practice. Particularly, deposited MnO_2 tends to detach from the substrate in concentrated acids, leading to insufficient charge compensation and rapid capacity fading.[37] To address this issue, it has become a normal routine to adopt MnO_2 pre-deposited substrates as cathodes.[40] Alternatively, a recent development involves the use of a MnO_2-containing colloid-in-acid electrolyte, which can provide sufficient charge compensation. With this approach, prolonged and stable battery operation over 489 days was achieved with a bare cathode substrate without MnO_2 pre-deposition.[37] This makes it feasible to build cathode-free batteries, simplifying the battery assembling process. In addition, taking advantage of the high theoretical specific capacity of Mn redox couples (107 Ah L^{-1} for 2.0 M $MnSO_4$ electrolyte[37]), the first Ampere-hour-level proton battery device has been demonstrated in the Mn-based system,[40] showcasing high practical prospects.

4.3.2. Lead Electrolysis Based

Lead electrolysis of $PbO_2/PbSO_4$ ($PbO_2 + 2e^- + SO_4^{2-} + 4H^+ \leftrightarrow PbSO_4 + 2H_2O$) and $PbSO_4/Pb$ ($PbSO_4 + 2e^- \leftrightarrow Pb + SO_4^{2-}$) have been extensively developed and are commercially available from lead acid batteries, making them readily accessible for designing novel aqueous proton batteries. So far, electrolytic reactions based on $PbO_2/PbSO_4$[16] and $PbSO_4/Pb$[41] redox pairs have been applied as high electrode-potential cathode and low-potential anode for electrolytic proton batteries, respectively. Liang et al. first realized high-capacity faradaic proton storage in an organic quinone compound of PTO (≈400 mAh g^{-1}),

© 2024 The Author(s). Advanced Functional Materials published by Wiley-VCH GmbH

RIGHTSLINK

16163028, 2024, 40, Downloaded from https://onlinelibrary.wiley.com/doi/10.1002/adfm.202405401 by Karlsruher Institut F., Wiley Online Library on [05/11/2024]. See the Terms and Conditions (https://onlinelibrary.wiley.com/terms-and-conditions) on Wiley Online Library for rules of use; OA articles are governed by the applicable Creative Commons License

and then demonstrated a battery with the electrolytic cathode of $PbO_2/PbSO_4$.[16] Benefitting the compact coin-cell configuration, the PTO//PbO_2 electrolytic battery presents excellent rate performances of ≈81% capacity retention up to 20 C and sustains stable cycling over 1500 cycles at 2 C. Niu group proposed a Pb//tetrachlorobenzoquinone (TCBQ) battery for ultralow temperature applications.[41] The low-potential conversion reaction between Pb and $PbSO_4$ was paired with TCBQ cathode, delivering a high full-cell voltage output of over 1 V, as shown in Figure 13d,e. Thanks to the adopted electrolytes of high-concentration sulfuric acid (5 M H_2SO_4), there is a significant reduction or even disruption of hydrogen bonds between water molecules. This enables the anti-freezing feature of electrolytes, leading to excellent low-temperature rate performance and cycling stability at −70 °C.

4.3.3. Gas Involved Redox Pairs

Gas-involved electrolytic reactions have also been adopted in fabricating proton battery devices, such as HER/HOR and OER/ORR. In 2018, Chen et al. reported a manganese-hydrogen battery toward grid-scale energy storage.[42] The authors adopted a manganese electrolytic cathode and a hydrogen anode (HER/HOR) catalyzed by Pt/C. Thanks to the large potential difference of both electrodes and reversible reaction mechanisms, the proof-of-concept battery delivered stable output voltage exceeding 1.2 V and exhibited sustainable cycling over 10 000 cycles as well as decent rate capability up to 100 mA cm^{-2}. Moreover, the authors successfully demonstrated a scale-up device (customized cylindrical cell, loading charge up to 15 mAh), highlighting the potential for practical applications. The gaseous HER/HOR electrode has been further adopted in other designs. Thotiyl and co-workers demonstrate a H_2//BQ flow-cell with BQ-contained cathode electrolyte.[141] The battery demonstrated a high specific capacity of ≈ 350 mAh g^{-1} and good cycling stability over 200 cycles. TCBQ have also been applied as an organic cathode for pairing with H_2 anode as shown in Figure 13f, the H_2//TCBQ battery achieves an output voltage of approximately 0.7 V along with excellent cycling stability over 0.1 million cycles.[114] A scale-up pouch cell was fabricated with an extended capacity (12 mAh, Figure 13g), which maintains a high capacity of 11 mAh over 500 cycles. Noteworthy, however, the hydrogen catalytic anode at this stage requires external H_2 supply to facilitate efficient HOR, thus increasing the complexity of the battery setup. An electrolytic electrode based on OER/ORR has also been reported, and a customized membrane electrode assembly (MEA) was fabricated with OER/ORR cathode and the counter anode of activated carbon (ion adsorption).[43]

4.3.4. Metal Deposition Based

Metal anodes have attracted wide attention due to their high theoretical capacity (e.g. 820 mAh g^{-1} and 2980 mAh g^{-1} for metallic Zn and Al respectively).[142] In 2019, Archer group developed an Al//V_2O_5 aqueous battery based on Al deposition-dissolution anode reaction and proton intercalation-deintercalation reaction in V_2O_5 cathode.[69] Despite reporting inferior cycling stability (<50 cycles) due to the electrochemical dissolution of the V_2O_5 cathode, this study proved the concept of coupling Al metal deposition with a protic cathode. Much superior performance has been achieved in Zn-anode-based proton batteries. Ma et al. introduced a Zn//α-MoO_3 battery with a super-concentrated dual-ion electrolyte (32 M $ZnCl_2$ + 1 M P_2O_5) as shown in Figure 13h.[125] This electrolyte, with confined water activity, supports stable Zn stripping-plating and reversible proton intercalation-deintercalation in the MoO_3 cathode simultaneously, achieving excellent cycling stability (98.3% capacity remaining over 1000 cycles). Zn anodes are also widely coupled with organic proton electrodes,[20,98,99] as mentioned earlier, demonstrating considerable electrochemical performance. A later work from the Xia group has achieved highly reversible Sn metal deposition-dissolution in a hybrid-type proton battery.[143] The methanesulfonic acid-based anode electrolyte was found to effectively regulate the uniformity of Sn deposition and suppress the HER side reaction. When paired with TCBQ cathode with H_2SO_4 cathode electrolyte, anode-free Sn//TCBQ batteries demonstrated prolonged cycling performance, exceeding 4,000 cycles. Nevertheless, the adoption of metal deposition-dissolution reaction in aqueous media is significantly restricted by the ESW and chemical corrosion (with concentrated acid), therefore, rational electrolyte design is expected in the future to enrich the range of alternative metal anode choices.

4.3.5. Halide Electrolysis Based

Redox conversions between polyhalide ions (e.g. Br_3^-/Br^-) were also reported as the high-potential counter-reaction for protonic electrodes. Wang et al. demonstrated the utilization of Br_3^-/Br^- conversion at the rGO cathode by introducing redox additive electrolytes.[116] They constructed a $Ti_3C_2T_x$//rGO asymmetric supercapacitor with enhanced voltage and capacity. During the charging process, electrooxidation of Br^- occurs on the rGO surface and the Br_3^- products are physically adsorbed by rGO, which is featured by an additional redox peak at 1.2 V (Figure 13i). Other polyhalide conversions (e.g. Cl_3^-/Cl^- and I_3^-/I^-) were also reported as counter-reactions in aqueous battery systems,[144] particularly for aqueous zinc ion batteries. However, their applicability for aqueous proton battery systems has been less explored. In addition, the oxidized polyhalide was reported to diffuse into the electrolyte and shuttle to the anode side, leading to inferior Coulombic efficiency and self-discharging.[145] Rational design of carbonaceous cathodes[146] and ion-selective separators[145] can help to fix the polyhalide ions, enhancing the capacity and lifespan of halide electrolysis-based batteries.

5. Summary and Outlook

In this review, we systematically summarize the fundamental principles and recent progress of various categories of faradaic electrodes and electrolytes for electrochemical proton storage. The associated limitations and potential improvement strategies are also discussed. Furthermore, we categorize the currently reported battery designs into two major types based on their operating principles/configurations, and highlight the respective

© 2024 The Author(s). Advanced Functional Materials published by Wiley-VCH GmbH

RIGHTSLINK

16163028, 2024, 40, Downloaded from https://onlinelibrary.wiley.com/doi/10.1002/adfm.202405401 by Karlsruher Institut F., Wiley Online Library on [05/11/2024]. See the Terms and Conditions (https://onlinelibrary.wiley.com/terms-and-conditions) on Wiley Online Library for rules of use; OA articles are governed by the applicable Creative Commons License

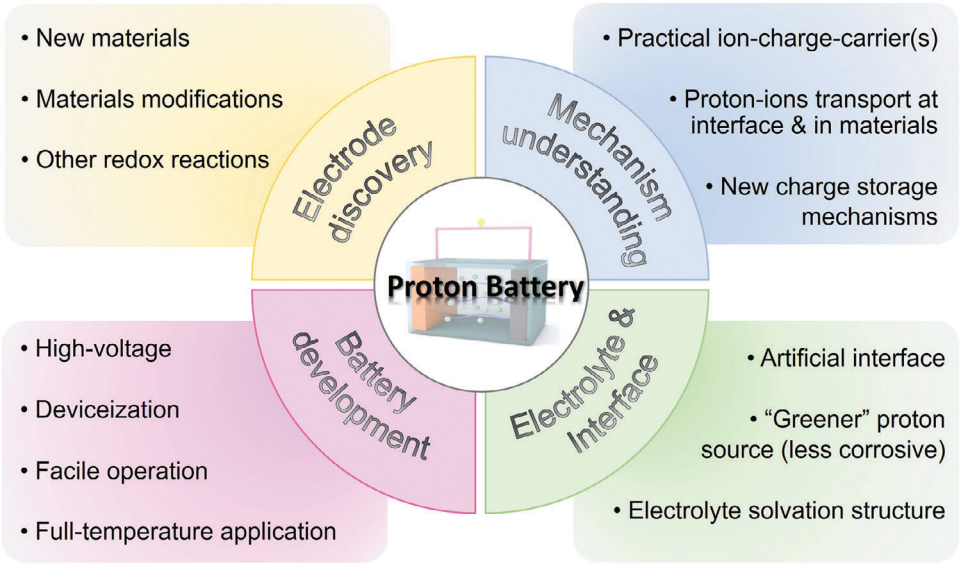

Figure 14. Solutions and outlook of aqueous proton batteries.

advances and limitations of each design. Overall, despite being in the early stages of development and having certain intrinsic limitations in energy output mainly as an aqueous energy storage technique, proton batteries possess natural advantages in terms of high-rate capability, low temperature feasibility, high safety, and low cost, etc. These features underscore their significant potential for various applications. Further advancing the field of proton batteries requires concerted efforts in developing high-performance electrodes, facile electrolytes, reliable and efficient full-cell designs, as well as deeply understanding the fundamental mechanisms (**Figure 14**). The following section provides our insights into the current challenges and/or future directions from these four key perspectives.

5.1. Electrodes

Electrodes are of the highest significance in affecting the performance of proton batteries. There are several criteria for potentially ideal candidates: (*i*) suitable working potential (located within the ESW, high potentials for cathodes and low potentials for anodes); (*ii*) compatible with acidic electrolytes; (*iii*) high reversible capacity; (*iv*) high electronic and ionic conductivity; (*v*) durable structural stability during proton insertion/extraction; (*vi*) environmental-friendly; (*vii*) low-cost. **Table 2** and **3** summarize various electrodes reported for electrochemical proton storage. Among these, α-MoO_3 stands out as a high-performance anode material due to its impressive capacity and compatibility with acidic environments. On the cathode side, PBA is notable for its high redox potential and fast ion-intercalation kinetics. The emergence of organic compounds has enriched the reservoir of electrode materials, bringing advantages such as tunability and cost-effectiveness. In addition, electrolytic electrodes provide alternative options for achieving high-voltage batteries. However, no single electrode currently meets all the desired criteria. The selection pool of suitable electrodes, particularly for cathodes, remains limited. These highlight an urgent need for the development of new electrodes and the optimization of existing electrodes to achieve high-performance proton batteries.

5.1.1. Inorganic Electrode Materials

Current choices of an inorganic anode are focused on Mo-based and W-based bronzes. While the cathode candidates are largely restricted in the family of PBAs, which is far from adequate. The significant advancements of LIBs have spurred the development of a diverse range of electrode materials. It is likely that some established electrodes could also be applied as protonic cathodes and advance high-voltage proton storage, such as the polyanion compounds like vanadium fluorophosphate.[58] The recent discovery of proton storage in copper oxalate further highlights the potential of polyanionic compounds.[150] Previous battery research has also developed effective material optimization strategies which can also be referred to. For example, defect engineering[151] and elemental doping[152] are possible to introduce extra active sites for proton insertion thus boosting capacities; Introducing artificial interface[153] (solid electrolyte interface or pre-coating layer) and pre-intercalation of heterogeneous species[154] (superlattice structure) are promising to enhance the structural stabilities. Particularly, lattice water can play an important role in protonic electrodes,[18,19,155] and regulating the lattice water is believed to offer a viable strategy to achieve high-rate performances proton electrodes. Regarding to electrodes based on electrolytic reactions, though many of them can be even "textbook reactions" like oxide deposition/depletion or metal plating/stripping, re-understanding via dedicated investigations on their specific reaction fundaments in acid-rich environments is highly recommended. A good example is the MnO_2/Mn^{2+} redox couple, which is well-known as an electrodeposition reaction depositing solids on substrates but products notable colloids in concentrated acids.[37]

© 2024 The Author(s). Advanced Functional Materials published by Wiley-VCH GmbH

RIGHTSLINK

16163028, 2024, 40, Downloaded from https://onlinelibrary.wiley.com/doi/10.1002/adfm.202405401 by Karlsruher Institut F., Wiley Online Library on [05/11/2024]. See the Terms and Conditions (https://onlinelibrary.wiley.com/terms-and-conditions) on Wiley Online Library for rules of use; OA articles are governed by the applicable Creative Commons License

Table 2. Performance summary of proton electrode materials.

Material	Electrolyte (acid-tolerance)	Conductivity[a)]	Mass loading [mg cm^{-2}]	Capacity	Cycling number/ capacity retention	Rate performance/ capacity retention	Refs.
α-MoO_3	4.4 M H_2SO_4 (high)	high	4	218 mAh g^{-1}@1000 mA g^{-1}	5000/75%	20 A g^{-1}/ 87%	[17]
h-WO_3	0.5 M H_2SO_4 (high)	middle-high	3	90 mAh g^{-1}@100 mA g^{-1}	20 000/94%	10 A g^{-1}/ 33%	[9]
TiO_2	0.5 M H_2SO_4 (middle-low)	high	1.12	117 mAh g^{-1}@17900 mA g^{-1}	15/56%	62.5A g^{-1}/ 56%	[70]
$(NH_4)_{0.5}V_2O_5$	0.001 M H_2SO_4 (low)	middle-high	1	149 mAh g^{-1}@50 mA g^{-1}	70 000/80%	2 A g^{-1}/ 57%	[68]
RuO_2	1 M H_2SO_4 (middle-low)	middle	3	156 mAh g^{-1}@100 mA g^{-1}	5000/80%	2 A g^{-1}/ 80%	[147]
MnO_2	2 M $ZnSO_4$ + 0.2 M $MnSO_4$ (low)	low	0.6	300 mAh g^{-1}@87 mA g^{-1}	10 000/100%	1.885 A g^{-1}/ 60%	[148]
CuFePBA	1 M H_2SO_4 (middle)	middle	1.5	93 mAh g^{-1}@95 mA g^{-1}	730 000/60%	380 A g^{-1}/ 50%	[18]
VFePBA	6 M H_2SO_4 (high)	middle-low	2.5	108 mAh g^{-1}@100 mA g^{-1}	25 000/92%	20 A g^{-1}/ 43%	[51]
$Ti_3C_2T_x$	3 M H_2SO_4 (middle-high)	high	1	86 mAh g^{-1}@500 mA g^{-1}	10 000/100%	100 A g^{-1}/ 86%	[116]
PTO	4.2 M H_2SO_4 (high)	middle-low	2	376 mAh g^{-1}@50 mA g^{-1}	5000/74%	50 A g^{-1}/ 27%	[84]
TCBQ	5 M H_2SO_4 (high)	low	1	216 mAh g^{-1}@100 mA g^{-1}	3000/62%	100 A g^{-1}/ 28%	[41]
HATN	2 M H_2SO_4 + 2 M $MnSO_4$ (middle)	middle-low	3	302 mAh g^{-1}@50 mA g^{-1}	3500/66%	100 A g^{-1}/ 39%	[103]
TPAD-COF	1.2 M H_2SO_4 (middle-low)	middle-low	0.5	126 mAh g^{-1}@200 mA g^{-1}	5000/84%	6 A g^{-1}/ 58%	[149]

[a)] The conductivities are evaluated based on the physical and/or electrochemical properties of electrode materials, electrolyte concentration, and the usage of conductive agents.

5.1.2. Organic Electrode Materials

Organic compounds play an important role in enriching the electrode choices for proton batteries, with certain organic electrodes showcasing impressive experimental specific capacities (e.g., >200 mAh g^{-1}), as shown in Figure 6b. However, their practical application is often hindered by low electrical conductivity, necessitating the extensive use of conductive agents (e.g., 50 wt.%). Enhancing conductivity can significantly bolster the practical utility of organic proton batteries, leading to improved volumetric and gravimetric capacities. Introducing conjugated structures by designing molecules with extended conjugation[99] or using conducting polymer backbones[87] can effectively enhance intramolecular electron transport, making it possible to reduce the dosage of conductive agents. Preparing organic compounds that are evenly distributed on (or encapsulated by) the conductive substrates is another promising method to minimize the usage of conductive agents. It is worth noting that the above-mentioned polymerization and hybridization with substrate methods can also contribute to stabilizing the organic compounds during cycling by mitigating material dissolution. Taking full advantage of the H-bond forming atoms (N, O, H, F) in organic compounds to construct intermolecular H-bond networks is another efficient strategy to facilitate proton transport and to improve reaction kinetics. Furthermore, organic compounds typically possess a relatively mediocre redox potential range (e.g. −0.2 – 0.5 V vs SHE), which often falls short of the boundaries of the ESW. Rational molecular design by regulating the functional groups can effectively tune the redox potentials of active centers, enabling expanded working potential ranges of organic electrodes and elevated output voltage of full-cells.

Besides, the following two aspects could be considered regarding the molecular design of the organic compounds to achieve ideal electrochemical performance. (*i*) Steric hindrance, reducing the steric hindrance of molecules can enhance the utilization rate of active sites by exposing more buried redox-active sites for trapping charge carriers;[156] (*ii*) Molecular polarity, considering the large molecular polarity of water in aqueous electrolytes, molecules with high symmetry (i.e. low polarity) may exhibit lower solubility in the electrolytes based on the "like-dissolves-like" rule.[157] In terms of the synthesis of organic compounds, one direction is to improve sustainability by using low-toxicity and low-cost chemical agents as well as minimizing the reaction and purification steps. These will benefit the large-scale production of aqueous proton batteries.

5.2. Electrolytes

5.2.1. Tuning Proton (de)Solvation

Among all discussed categories, aqueous (Arrhenius) acids are the most common choice, due to their direct applicability, low cost, wide availability, and easy preparation. To mitigate electrolyte decomposition and/or electrode structure degradation, various strategies for altering the proton solvation structure have been developed. These strategies reduce the electrolyte water fractions and/or suppress free water activity, thereby effectively improving electrode/battery cycling stability. Representative approaches include adopting concentrated electrolytes or composite acids, introducing solvation competing agents and/or adopting co-solvent.[17,21,22,37] All these can be readily extended to Lewis acids, facilitating proton-metal batteries; However, there is only one report so far,[125] indicating a promising direction for future research. Moreover, these electrolyte engineering strategies have also been shown to influence the hydrogen-bonding network within electrolytes,[22,132] thereby lowering

© 2024 The Author(s). Advanced Functional Materials published by Wiley-VCH GmbH

RIGHTSLINK

16163028, 2024, 40, Downloaded from https://onlinelibrary.wiley.com/doi/10.1002/adfm.202405401 by Karlsruher Institut F., Wiley Online Library on [05/11/2024]. See the Terms and Conditions (https://onlinelibrary.wiley.com/terms-and-conditions) on Wiley Online Library for rules of use; OA articles are governed by the applicable Creative Commons License

Table 3. Summary of advantages and disadvantages of different types of proton electrodes, electrolytes, and full-cell configurations.

Type	Advantages	Disadvantages
Proton electrodes		
α-MoO_3	High capacity; Low operation voltage; Compatible with concentrated acids.	Poor cycle life in diluted acids.
h-WO_3; RuO_2	Adjustable water contents.	High cost; Low capacity.
V_2O_5; MnO_2	High operation voltage; Proton and metal-ion co-insertion.	High solubility in acids.
TiO_2	Low operation voltage; Low cost; High conductivity; Fast ion insertion.	Poor cycle life; HER side reaction; Low capacity.
PBA	High operation voltage; Fast ion insertion.	Low capacity.
MXene	Fast ion insertion; Wide operation voltage.	Low capacity; Complex synthesis.
Organic compounds	High capacity; Adjustable electrochemical property; Low-cost.	Low conductivity; Dissolution in concentrated acids.
Electrolytic electrodes	Fixed operation voltage; High specific capacity.	Free-shuttle of active materials (Mn-based); Complex setup (gas-based).
Protonic electrolytes		
Diluted aqueous acids	Low cost; Compatibility for organic electrodes; High conductivity.	Narrow voltage window; Narrow temperature range.
Concentrated aqueous acids	Low water activity (good cycle life for some electrodes); Low freezing temperature.	Increased cost; Possible corrosions on battery components.
Lweis acids (e.g. $ZnCl_2$)	Low corrosion; Low cost; High safety.	Limited electrode choices.
Aqueous acids with additives (e.g. 4.2 M H_2SO_4 + PEG 400; 1 M HCl + 20 M $ZnCl_2$)	Low water activity (good cycle life for some electrodes); Wide voltage window; Low freezing temperature.	Increased cost; Low conductivity; Low viscosity.
Non-aqueous electrolytes (e.g. 1 M H_3PO_4 in MeCN)	Wide voltage window; Reduced side reaction (gassing issue); Low compatibility to organic electrodes.	Increased cost and toxicity; Increased flammability; Environmental issues; Low conductivity.
Quasi-solid/solid electrolytes	Low water activity (good cycle life for some electrodes); Low freezing temperature; Reduced side reaction (gassing issue); Functional battery design.	Increased cost; Slow ion diffusion; Complex preparation.
Aqueous proton full-cells		
Rocking-chair-type	Fast ion diffusion; Low-cost (all-organic battery).	Require capacity match between electrodes; Low volumetric energy density (all-organic battery); Low voltage (all-organic battery).
Mn-based Hybrid-type	Facile assembly; High voltage; Low temperature performance.	Self-discharging.
Pb-based hybrid-type	Commercially available; High voltage; Low temperature performance.	Require concentrated acids.
Gas-involved hybrid-type	Good cycle life; Low temperature performance.	Complex assembly; High cost.
Metal-based hybrid type	Low corrosion; Standardized coin-cell setup.	Poor cycle life.

© 2024 The Author(s). Advanced Functional Materials published by Wiley-VCH GmbH

16163028, 2024, 40, Downloaded from https://onlinelibrary.wiley.com/doi/10.1002/adfm.202405401 by Karlsruher Institut F., Wiley Online Library on [05/11/2024]. See the Terms and Conditions (https://onlinelibrary.wiley.com/terms-and-conditions) on Wiley Online Library for rules of use; OA articles are governed by the applicable Creative Commons License

Table 4. Summary of various energy storage technologies.

Battery type	Anode//cathode	Current collector [cost]	Electrolyte [cost]	Voltage [V]	Max energy density [Wh kg^{-1}]	Power density [W kg^{-1}]	status
Li-ion battery	Graphite//$LiFePO_4$	Cu (middle)	1 M $LiPF_6$ (middle)	3.2	200 (device scale)	10–400	commercialized
Lead-acid battery	Pb//PbO_2	Pb (low)	5 M H_2SO_4 (low)	2	30 (device scale)	1–300	commercialized
Ni-MH battery	MH_x//NiOOH	Ni, steel (low)	6 M KOH (low)	1.35	80 (device scale)	10–1000	commercialized
Li-ion aqueous battery[159]	Mo_6S_8// $LiNi_{0.5}Mn_{1.5}O_4$	Ti (high)	21 M LiTFSI (high)	2.5	80 (electrode scale)	NA	Lab-scale
Li-ion aqueous battery[160]	VO_2//$LiVOPO_4$	Ti (high)	20 M LiTFSI (high)	1.3	84 (electrode scale)	33–530	Lab-scale
K-ion aqueous battery[161]	PTCDI// FeMnPBA	Steel (low)	22 M KCF_3SO_3 (high)	1.1	80 (electrode scale)	41–1612	Lab-scale
Zn-ion aqueous battery[162]	Zn//$Ca_{0.25}V_2O_5{\cdot}nH_2O$	Steel (low)	1 M $ZnSO_4$ (low)	0.8	267 (electrode scale)	53–1825	Lab-scale
Zn-ion aqueous battery[163]	Zn//ZnFePBA	Steel (low)	1 M $ZnSO_4$ (low)	1.75	100 (electrode scale)	100–1700	Lab-scale
Proton battery[84]	PTO//VFePBA	Ti (high)	4.2 M H_2SO_4 (low)	0.6	46.5 (electrode scale)	10–10000	Lab-scale
Proton battery[16]	PTO//PbO_2	Ti (high)	4.4 M H_2SO_4 (low)	1.1	76 (electrode scale)	10–2000	Lab-scale

electrolyte freezing point and promoting low-temperature applications. Future studies should continue to focus on these aspects to exploit further and enhance the low-temperature battery performances. Developing solvent-free electrolytes based on protic liquids is an alternative route that is also effective with even more superior performances.[26] One representative protic liquid of poly-phosphoric acid is synthesized by the dehydration of less-corrosive and cheap phosphoric acid, and both of them are believed to deserve further developments in the future. An artificial coating layer has also been shown highly effective in enhancing electrode stability and promoting charge transfer.[59] This suggests possible benefits of a solid electrolyte interface (SEI), making it also a promising target for future rational electrolyte designs, e.g., SEI forming additive.[21]

5.2.2. Altering Electrolyte States

On the other hand, developing electrolytes with diverse physical states is also a very promising direction. In previous sections, we have discussed the current progress of new electrolytes in (quasi-)solid state or other non-common states, which expand the application scenario of proton batteries and/or promote discoveries of novel properties. However, some classic choice of solid-state proton conductors seems neglected. One notable candidate is the semi-permeable membrane derived from sulfonated tetrafluoroethylene-based fluoropolymer-copolymer, famously known as "Nafion", and a recent study shows the use of "Nafion" can effectively extend the shelf-life of electrolytic proton batteries.[38] Future works on membrane electrode assembly (MEA) systems can be expected that possibly pave the way for practical solid-state proton batteries. Moreover, Inorganic perovskite oxides (ABO_3) are also long known for their efficient proton conductivity, albeit typically at high temperatures. A recent breakthrough highlights $HSrCoO_{2.5}$ as it exhibits unusually high proton conductivity at prominent lower temperatures (40 – 140 °C),[158] suggesting its potential application in proton batteries.

5.3. Full-Cells and Applications for Proton Batteries

5.3.1. Cross-Comparisons

Table 4 compares the technical features of proton batteries and representative battery systems, e.g., lithium-ion batteries (LIBs), lead-acid batteries, and nickel-metal hydride (Ni-MH_x) batteries which are the mainstream techniques in the secondary battery market. The early established lead-acid and Ni-MH_x batteries, primarily thanks to the reduced costs and a wide operational temperature range, still hold a significant proportion of the global market. Nevertheless, their further development potential is limited, largely restricted by their low energy density and other inherent drawbacks. LIBs now dominate the commercial power source sector due to their high energy density. Despite, the scarcity of related metal resources and safety concerns exclude it from grid-scale applications. Although the safety can be effectively improved through the recent advances in aqueous metal-ion battery techniques, their energy outputs are significantly compromised, and the fabrication cost retains high if adopting highly concentrated electrolytes. The emerging aqueous zinc-ion batteries (AZIBs) show good promise in grid-scale applications with decent performances, and intensive studies across various scales are currently underway. Particularly, recent research discloses possible proton participation with even significant contributions.[57,78,125] Considering the Lewis acid nature of most correlated electrolytes, many designs of AZIBs could also be categorized into proton-metal batteries. More recent advancements in proton batteries have further amplified their high-power advantages, which are even more superior than previous aqueous batteries. This makes them excellent candidates for scalable applications that require rapid response, such as the integration and storage of intermittent renewable energies.

© 2024 The Author(s). Advanced Functional Materials published by Wiley-VCH GmbH

RIGHTSLINK

16163028, 2024, 40, Downloaded from https://onlinelibrary.wiley.com/doi/10.1002/adfm.202405401 by Karlsruher Institut F., Wiley Online Library on [05/11/2024]. See the Terms and Conditions (https://onlinelibrary.wiley.com/terms-and-conditions) on Wiley Online Library for rules of use; OA articles are governed by the applicable Creative Commons License

5.3.2. Application Considerations

There are several factors to be considered/addressed for applications of proton batteries. (*i*) Fabrication cost. Although there is no harsh process control required and the cost of electrode and electrolyte can both be low, reliable corrosion-proof current collectors (Ti substrates and carbon fabrics in lab) are necessary which raises the overall fabrication cost. To mitigate this issue, future efforts should develop high-performance electrolytes with lower/dilute concentrations[68] and mild Lewis acid electrolytes[69,98] (or even neutral buffer electrolytes[164]), or electrode(material)-less batteries based on electrolytic reactions. (*ii*) Limited energy and voltage output. As summarized in Table 1, rocking-chair type batteries typically exhibit a low median discharge voltage of <0.9 V, and the cases of all-organic proton batteries can be inferior (<0.6V). Although current electrolytic proton batteries can reach an increased median voltage ≈1.1V, it is still lower than the values of classic techniques like Ni-MH_x and lead-acid batteries. Facing this challenge, future developments should keep exploring suitable reactions/materials with high or low electrode potential (*e.g.*, MnO_4^-/Mn^{2+}, 1.51 V vs SCE). Additionally, investigating new electrolytes with more expanded ESW could lead to new redox reaction discoveries[56] and the integration of more electrodes. (*iii*) Preferred application scenario. There is no single technique that meets the requirements of every application. Instead, it is more practical to maximize the advantages of specific technique for specific applications. Except for the harvest/storage of renewables benefitting the fast kinetics, another application scenario in polar and space activities can be emphasized, thanks to the extraordinary low-temperature performances.

On the other hand, current research lacks universality, where various customized testing configurations and parameters were adopted for full-cell evaluations. This makes it difficult for cross-comparison. Hence, establishing standardized testing protocols is in urgent necessity. It is encouraged to present more key factors for battery device evaluations, such as energy densities (by mass or by volume) and self-discharging performances. Also, future work should consider attempts in constructing Ah-level device prototypes and full-cell stacks to bridge the research with real-world applications of proton batteries. Overall, there is a long journey ahead to optimize and apply proton batteries, and we anticipate more exciting research in the future.

5.4. Mechanism Understanding

5.4.1. Proton Intercalation

Since the recent renaissance of proton batteries, there has been a series of new perspectives on the fundamental aspects of proton electrochemistry. A prominent example is the discussed dispute on the proton intercalation process and the true nature of the intercalant species (naked proton or hydronium) in solid electrodes. Despite the high hydronium desolvation energy[133] and the large intracrystalline space within some materials, naked proton insertion/transportation has been found to take place in many various electrodes, including representative hydrogen bronzes (α-MoO_3 and $WO_3{\cdot}nH_2O$),[17,64,165] Prussian blue analogues,[18] MXenes,[19] etc. The knowledge well guides the following optimization strategies on electrode/electrolyte and therefore promotes the battery developments. Also, the contradictions to conventional understanding indicate unique mechanisms in proton electrochemistry, and the observed conflicts in literature suggest limitations of individual characterization techniques, thereby highlighting the necessity for comprehensive investigation. On the other hand, following preliminary clues/indications in literature,[84,86] a recent advance has provided direct experimental evidence from multiple perspectives, eventually demonstrating hydronium intercalation.[55] Impressively, fast rate and long lifespan are reached in electrodes of hexagonal molybdate (h-MoO_3) monocrystals even over 200 µm. The finding points out an alternative direction for developing solvent co-intercalation in proton batteries. The phenomena of solvent co-intercalation have already achieved significant success in facilitating the intercalation of sluggish multi-valent cations, largely due to improved kinetics resulting from reduced desolvation penalty and ion-host-interaction.[166] Given both these records, it also holds promise to develop proton-solvent co-intercalation chemistry, potentially leading to more exciting properties. Noted, however, the Grotthuss proton transfer could also present features of a desolvation-free process, as indicated by the almost temperature-independent charge transfer resistance in $H_{1.75}MoO_3$ bronzes with an estimated activation energy of ≈0.02 eV.[60]

5.4.2. Proton Conduction

Following above, another prospect could be further understanding and optimizing/benefitting proton transportation. In aqueous solutions, "Grotthuss" proton conduction (Figure 1b) proceeds with the translational events of naked proton via the hydrogen bond chains through bonded water molecules. Meanwhile characteristic intermediates like Zundel $[H_2O{\cdots}H^+{\cdots}OH_2]$ and Eigen $[H_3O^+({\cdots}OH_2)_3]$ cations are formed,[10] which in turn serves as one key criterion for this conduction. Solid-state "Grotthuss" conduction has recently been demonstrated applicable in hydrous materials (e.g., PBA, MXene, $RuO_2{\cdot}nH_2O$)[18,19,76] following the same mechanism of Eigen-Zundel-Eigen as in the bulk water. However, there are exceptions. Lin et al. revealed a non-Grotthuss Proton diffusions in $WO_3{\cdot}nH_2O$.[165] Protons are found to hop through the lattice oxygens without direct involvement of structural water. However, conflicts can be also noticed, as a fast one-dimensional diffusion in $WO_3{\cdot}H_2O$ is further calculated out to associate with an activation energy (E_a) of only 0.07 eV at dilute proton concentrations, significantly lower than the threshold for "Grotthuss" conduction (E_a < 0.4 eV.[10] Xu et al. reported a similar proton hopping mechanism in anhydrous molybdenum bronzes of $H_{1.75}MoO_3$ (electrochemically activated from α-MoO_3), while they considered it as Grotthuss conduction.[60] Their simulation results depict proton transportation through interconnected hydrogen bonding network of terminal -OH_2 groups, which is accompanied with an activation energy of 0.23 eV. These facts indicate possibly generalized Grotthuss conduction, which deserves further investigation.

The other proton conduction manner, i.e., vehicle mechanism, has also been demonstrated applicable in solid-state (hexagonal

© 2024 The Author(s). Advanced Functional Materials published by Wiley-VCH GmbH
RIGHTSLINK

16163028, 2024, 40, Downloaded from https://onlinelibrary.wiley.com/doi/10.1002/adfm.202405401 by Karlsruher Institut F., Wiley Online Library on [05/11/2024]. See the Terms and Conditions (https://onlinelibrary.wiley.com/terms-and-conditions) on Wiley Online Library for rules of use; OA articles are governed by the applicable Creative Commons License

molybdates).[55] However, there is currently little knowledge on more detailed scenarios and conflicting explanations also exist. Shown in Figure 5f, intercalations of different extent solvated hydroniums result in deviations in structure evolutions as depicted by *operando* XRD. While same structures are identified after electrode relaxations, indicating post-reaction changes. Investigations by a different group revealed an experimental ion diffusion energy barrier of 0.3 eV for the similar materials, which is notably superior than that for α-MoO_3 (0.6 eV).[62] This fast kinetics is attributed to structural water facilitated Grotthuss proton conduction by simulation. These frequently opposite understandings suggest a highly active field of research and highlight the significance of further in-depth understanding. Additionally, hydronium intercalation is reasonable in organic electrodes materials based on molecular crystals.[84,86] A current report depicts a Grotthuss proton conduction (at molecule scale) in a supramolecular self-assembly of H-bonded organic superstructures,[20] nevertheless, it remains unclear how proton/hydronium conduction proceeds (at crystal scale) in more generalized molecule crystals and/or in their unit cells.

Acknowledgements

C.Z. acknowledges the support from the Australian Research Council (IC200100023 and CE230100017). H.G. is grateful for the financial support from the Alexander von Humboldt Foundation.

Open access publishing facilitated by University of New South Wales, as part of the Wiley - University of New South Wales agreement via the Council of Australian University Librarians.

Conflict of Interest

The authors declare no conflict of interest.

Keywords

acidic electrolytes, aqueous energy storage, hydrogen bronzes, intercalation, proton-ions

Received: March 28, 2024
Revised: June 21, 2024
Published online: August 9, 2024

[1] W. Li, J. R. Dahn, D. S. Wainwright, *Science* **1994**, *264*, 1115.
[2] D. Chao, W. Zhou, F. Xie, C. Ye, H. Li, M. Jaroniec, S. Z. Qiao, *Sci. Adv.* **2020**, *6*, eaba4098.
[3] H. Ao, Y. Zhao, J. Zhou, W. Cai, X. Zhang, Y. Zhu, Y. Qian, *J. Mater. Chem. A* **2019**, *7*, 18708.
[4] J. Huang, Z. Guo, Y. Ma, D. Bin, Y. Wang, Y. Xia, *Small Methods* **2019**, *3*, 1800272.
[5] W. Sun, F. Wang, S. Hou, C. Yang, X. Fan, Z. Ma, T. Gao, F. Han, R. Hu, M. Zhu, C. Wang, *J. Am. Chem. Soc.* **2017**, *139*, 9775.
[6] P. Jiang, Z. Lei, L. Chen, X. Shao, X. Liang, J. Zhang, Y. Wang, J. Zhang, Z. Liu, J. Feng, *ACS Appl. Mater. Interfaces* **2019**, *11*, 28762.
[7] Y. Xu, X. Wu, X. Ji, *Small Struct.* **2021**, *2*, 2000113.
[8] X. Wang, Y. Xie, K. Tang, C. Wang, C. Yan, *Angew. Chem., Int. Ed.* **2018**, *57*, 11569.
[9] H. Jiang, J. J. Hong, X. Wu, T. W. Surta, Y. Qi, S. Dong, Z. Li, D. P. Leonard, J. J. Holoubek, J. C. Wong, J. J. Razink, X. Zhang, X. Ji, *J. Am. Chem. Soc.* **2018**, *140*, 11556.
[10] H. Guo, C. Zhao, *Small Methods* **2023**, 2300699.
[11] N. Yabuuchi, K. Kubota, M. Dahbi, S. Komaba, *Chem. Rev.* **2014**, *114*, 11636.
[12] Z. Su, W. Ren, H. Guo, X. Peng, X. Chen, C. Zhao, *Adv. Funct. Mater.* **2020**, *30*, 1.
[13] S. Nohara, T. Miura, C. Iwakura, H. Inoue, *Electrochemistry* **2007**, *75*, 579.
[14] M. Armand, J.-M. Tarascon, *Nature* **2008**, *451*, 652.
[15] K. Nueangnoraj, T. Tomai, H. Nishihara, T. Kyotani, I. Honma, *Carbon* **2016**, *107*, 831.
[16] Y. Liang, Y. Jing, S. Gheytani, K.-Y. Lee, P. Liu, A. Facchetti, Y. Yao, *Nat. Mater.* **2017**, *16*, 841.
[17] H. Guo, D. Goonetilleke, N. Sharma, W. Ren, Z. Su, A. Rawal, C. Zhao, *Cell Rep. Phys. Sci.* **2020**, *1*, 100225.
[18] X. Wu, J. J. Hong, W. Shin, L. Ma, T. Liu, X. Bi, Y. Yuan, Y. Qi, T. W. Surta, W. Huang, J. Neuefeind, T. Wu, P. A. Greaney, J. Lu, X. Ji, *Nat. Energy* **2019**, *4*, 123.
[19] Y. Sun, C. Zhan, P. R. C. Kent, M. Naguib, Y. Gogotsi, D. Jiang, *ACS Appl. Mater. Interfaces* **2019**, *12*, 763.
[20] Z. Song, L. Miao, L. Ruhlmann, Y. Lv, L. Li, L. Gan, M. Liu, *Angew. Chem., Int. Ed.* **2023**, *135*, e202219136.
[21] Z. Su, J. Chen, W. Ren, H. Guo, C. Jia, S. Yin, J. Ho, C. Zhao, *Small* **2021**, *17*, 2102375.
[22] S. Wu, J. Chen, Z. Su, H. Guo, T. Zhao, C. Jia, J. Stansby, J. Tang, A. Rawal, Y. Fang, J. Ho, C. Zhao, *Small* **2022**, *18*, 2202992.
[23] S. Wang, H. Jiang, Y. Dong, D. Clarkson, H. Zhu, C. M. Settens, Y. Ren, T. Nguyen, F. Han, W. Fan, *Adv. Mater.* **2022**, *34*, 2202063.
[24] H. Jiang, W. Shin, L. Ma, J. J. Hong, Z. Wei, Y. Liu, S. Zhang, X. Wu, Y. Xu, Q. Guo, *Adv. Energy Mater.* **2020**, *10*, 2000968.
[25] L. Yan, J. Huang, Z. Guo, X. Dong, Z. Wang, Y. Wang, *ACS Energy Lett.* **2020**, *5*, 685.
[26] M. Liao, X. Ji, Y. Cao, J. Xu, X. Qiu, Y. Xie, F. Wang, C. Wang, Y. Xia, *Nat. Commun.* **2022**, *13*, 6064.
[27] Z. Ma, X. M. Shi, S. I. Nishimura, S. Ko, M. Okubo, A. Yamada, *Adv. Mater.* **2022**, *34*, 2203335.
[28] W. Huang, K. Zhang, B. Yuan, L. Yang, M. Zhu, *Energy Storage Mater.* **2022**, *50*, 152.
[29] X. Wu, S. Qiu, Y. Xu, L. Ma, X. Bi, Y. Yuan, T. Wu, R. Shahbazian-Yassar, J. Lu, X. Ji, *ACS Appl. Mater. Interfaces* **2020**, *12*, 9201.
[30] X. Ji, *eScience* **2021**, *1*, 99.
[31] M. Shi, P. Das, Z. Wu, T. Liu, X. Zhang, *Adv. Mater.* **2023**, *35*, 2302199.
[32] J.-L. Yang, J.-M. Cao, X.-X. Zhao, K.-Y. Zhang, S.-H. Zheng, Z.-Y. Gu, X.-L. Wu, *EnergyChem* **2022**, *4*, 100092.
[33] J. Li, H. Yan, C. Xu, Y. Liu, X. Zhang, M. Xia, L. Zhang, J. Shu, *Nano Energy* **2021**, *89*, 106400.
[34] X. Dong, Z. Li, B. Ding, H. Dou, X. Zhang, *ChemElectroChem* **2024**, *11*, 202300569.
[35] B. Zhang, L. Wang, Y. Zhang, X. Wang, Y. Qiao, S.-G. Sun, *J. Chem. Phys.* **2023**, *158*, 054202.
[36] Y. Xu, X. Wu, H. Jiang, L. Tang, K. Y. Koga, C. Fang, J. Lu, X. Ji, *Angew. Chem., Int. Ed.* **2020**, *59*, 22007.
[37] H. Guo, L. Wan, J. Tang, S. Wu, Z. Su, N. Sharma, Y. Fang, Z. Liu, C. Zhao, *Nano Energy* **2022**, *102*, 107642.
[38] S. Wu, H. Guo, Z. Su, C. Jia, X. Zhang, S. Wang, T. Zhao, Q. Meyer, C. Zhao, *Adv. Funct. Mater.* **2024**, *34*, 2315706.
[39] J. P. Zheng, P. J. Cygan, T. R. Jow, *J. Electrochem. Soc.* **1995**, *142*, 2699.
[40] X. Yang, Y. Ni, Y. Lu, Q. Zhang, J. Hou, G. Yang, X. Liu, W. Xie, Z. Yan, Q. Zhao, J. Chen, *Angew. Chem., Int. Ed.* **2022**, *61*, e202209642.
[41] F. Yue, Z. Tie, S. Deng, S. Wang, M. Yang, Z. Niu, *Angew. Chem., Int. Ed.* **2021**, *133*, 14001.
[42] W. Chen, G. Li, A. Pei, Y. Li, L. Liao, H. Wang, J. Wan, Z. Liang, G. Chen, H. Zhang, J. Wang, Y. Cui, *Nat. Energy* **2018**, *3*, 428.
[43] S. Heidari, S. S. Mohammadi, A. S. Oberoi, J. Andrews, *Int. J. Hydrogen Energy* **2018**, *43*, 6197.

© 2024 The Author(s). Advanced Functional Materials published by Wiley-VCH GmbH

RIGHTSLINK

16163028, 2024, 40, Downloaded from https://onlinelibrary.wiley.com/doi/10.1002/adfm.202405401 by Karlsruher Institut F., Wiley Online Library on [05/11/2024]. See the Terms and Conditions (https://onlinelibrary.wiley.com/terms-and-conditions) on Wiley Online Library for rules of use; OA articles are governed by the applicable Creative Commons License

[44] X. Zhang, T. Xiong, B. He, S. Feng, X. Wang, L. Wei, L. Mai, *Energy Environ. Sci.* **2022**, *15*, 3750.
[45] W. Li, C. Han, G. Cheng, S. Chou, H. Liu, S. Dou, *Small* **2019**, *15*, 1900470.
[46] H. Yi, R. Qin, S. Ding, Y. Wang, S. Li, Q. Zhao, F. Pan, *Adv. Funct. Mater.* **2021**, *31*, 2006970.
[47] S. Ohkoshi, K. Nakagawa, K. Tomono, K. Imoto, Y. Tsunobuchi, H. Tokoro, *J. Am. Chem. Soc.* **2010**, *132*, 6620.
[48] Y. You, X.-L. Wu, Y.-X. Yin, Y.-G. Guo, *J. Mater. Chem. A* **2013**, *1*, 14061.
[49] J. Qiao, M. Qin, Y.-M. Shen, J. Cao, Z. Chen, J. Xu, *ChemComm* **2021**, *57*, 4307.
[50] T. Xu, Z. Li, D. Wang, M. Zhang, L. Ai, Z. Chen, J. Zhang, X. Zhang, L. Shen, *Adv. Funct. Mater.* **2022**, *32*, 2107720.
[51] X. Peng, H. Guo, W. Ren, Z. Su, C. Zhao, *ChemComm* **2020**, *56*, 11803.
[52] P. Colomban, *Proton Conductors: Solids, Membranes and Gels-Materials and Devices*, Cambridge University Press, Cambridge **1992**.
[53] E. M. McCarron III, D. M. Thomas, J. C. Calabrese, *Inorg. Chem.* **1987**, *26*, 370.
[54] H.-S. Kim, J. B. Cook, H. Lin, J. S. Ko, S. H. Tolbert, V. Ozolins, B. Dunn, *Nat. Mater.* **2017**, *16*, 454.
[55] H. Guo, S. Wu, W. Chen, Z. Su, Q. Wang, N. Sharma, C. Rong, S. Fleischmann, Z. Liu, C. Zhao, *Adv. Mater.* **2023**, *36*, 2307118.
[56] Y. Lei, W. Zhao, J. Yin, Y. Ma, Z. Zhao, J. Yin, Y. Khan, M. N. Hedhili, L. Chen, Q. Wang, Y. Yuan, X. Zhang, O. M. Bakr, O. F. Mohammed, H. N. Alshareef, *Nat. Commun.* **2023**, *14*, 5490.
[57] H. Zhang, W. Wu, Q. Liu, F. Yang, X. Shi, X. Liu, M. Yu, X. Lu, *Angew. Chem., Int. Ed.* **2021**, *60*, 896.
[58] M. Liao, Y. Cao, Z. Li, J. Xu, Y. Qi, Y. Xie, Y. Peng, Y. Wang, F. Wang, Y. Xia, *Angew. Chem., Int. Ed.* **2022**, *134*, e202206635.
[59] C. Wang, S. Zhao, X. Song, N. Wang, H. Peng, J. Su, S. Zeng, X. Xu, J. Yang, *Adv. Energy Mater.* **2022**, *12*, 2200157.
[60] W. Xu, K. Zhao, X. Liao, C. Sun, K. He, Y. Yuan, W. Ren, J. Li, T. Li, C. Yang, *J. Am. Chem. Soc.* **2022**, *144*, 17407.
[61] A. Chithambararaj, N. Rajeswari Yogamalar, A. C. Bose, *Cryst. Growth Des.* **2016**, *16*, 1984.
[62] T. Xu, Z. Xu, T. Yao, M. Zhang, D. Chen, X. Zhang, L. Shen, *Nat. Commun.* **2023**, *14*, 8360.
[63] J. B. Mitchell, W. C. Lo, A. Genc, J. LeBeau, V. Augustyn, *Chem. Mater.* **2017**, *29*, 3928.
[64] J. B. Mitchell, N. R. Geise, A. R. Paterson, N. C. Osti, Y. Sun, S. Fleischmann, R. Zhang, L. A. Madsen, M. F. Toney, D. Jiang, A. I. Kolesnikov, E. Mamontov, V. Augustyn, *ACS Energy Lett.* **2019**, *4*, 2805.
[65] Z. Chen, Y. Peng, F. Liu, Z. Le, J. Zhu, G. Shen, D. Zhang, M. Wen, S. Xiao, C.-P. Liu, *Nano Lett.* **2015**, *15*, 6802.
[66] A. Moretti, S. Passerini, *Adv. Energy Mater.* **2016**, *6*, 1600868.
[67] X. Liu, H. Euchner, M. Zarrabeitia, X. Gao, G. A. Elia, A. Groß, S. Passerini, *ACS Energy Lett.* **2020**, *5*, 2979.
[68] N. Lv, R. Ren, Y. Wu, Z. Xu, D. Wu, X. You, G. Zhu, Y. Zhang, S. Dong, *Electrochim. Acta* **2022**, *431*, 141097.
[69] Q. Zhao, L. Liu, J. Yin, J. Zheng, D. Zhang, J. Chen, L. A. Archer, *Angew. Chem., Int. Ed.* **2020**, *59*, 3048.
[70] C. Geng, T. Sun, Z. Wang, J.-M. Wu, Y.-J. Gu, H. Kobayashi, P. Yang, J. Hai, W. Wen, *Nano Lett.* **2021**, *21*, 7021.
[71] N. Makivic, J.-Y. Cho, K. D. Harris, J.-M. Tarascon, B. Limoges, V. Balland, *Chem. Mater.* **2021**, *33*, 3436.
[72] M. Shimizu, D. Nishida, A. Kikuchi, S. Arai, *J. Phys. Chem. C* **2023**, *127*, 17677.
[73] Y.-S. Kim, S. Kriegel, K. D. Harris, C. Costentin, B. Limoges, V. Balland, *J. Phys. Chem. C* **2017**, *121*, 10325.
[74] S. Fleischmann, Y. Sun, N. C. Osti, R. Wang, E. Mamontov, D. Jiang, V. Augustyn, *J. Mater. Chem. A* **2020**, *8*, 412.
[75] W. Dmowski, T. Egami, K. E. Swider-Lyons, C. T. Love, D. R. Rolison, *J. Phys. Chem. B* **2002**, *106*, 12677.
[76] S. F. Parker, S. J. Robertson, S. Imberti, *Mol. Phys.* **2019**, *117*, 3417.
[77] J.-G. Wang, *Supercapacitor Design and Applications* **2016**.
[78] H. Pan, Y. Shao, P. Yan, Y. Cheng, K. S. Han, Z. Nie, C. Wang, J. Yang, X. Li, P. Bhattacharya, *Nat. Energy* **2016**, *1*, 1.
[79] Y. Jin, L. Zou, L. Liu, M. H. Engelhard, R. L. Patel, Z. Nie, K. S. Han, Y. Shao, C. Wang, J. Zhu, *Adv. Mater.* **2019**, *31*, 1900567.
[80] Z. Tie, Z. Niu, *Angew. Chem., Int. Ed.* **2020**, *59*, 21293.
[81] Z. Guo, Y. Ma, X. Dong, J. Huang, Y. Wang, Y. Xia, *Angew. Chem., Int. Ed.* **2018**, *130*, 11911.
[82] T. Nokami, T. Matsuo, Y. Inatomi, N. Hojo, T. Tsukagoshi, H. Yoshizawa, A. Shimizu, H. Kuramoto, K. Komae, H. Tsuyama, *J. Am. Chem. Soc.* **2012**, *134*, 19694.
[83] Z. Guo, J. Huang, X. Dong, Y. Xia, L. Yan, Z. Wang, Y. Wang, *Nat. Commun.* **2020**, *11*.
[84] Z. Su, J. Tang, J. Chen, H. Guo, S. Wu, S. Yin, T. Zhao, C. Jia, Q. Meyer, A. Rawal, *Small Struct.* **2023**, *4*, 2200257.
[85] F. Yue, Z. Tie, Y. Zhang, S. Bi, Y. Wang, Z. Niu, *Angew. Chem., Int. Ed.* **2022**, *61*, e202208513.
[86] X. Wang, C. Bommier, Z. Jian, Z. Li, R. S. Chandrabose, I. A. Rodríguez-Pérez, P. A. Greaney, X. Ji, *Angew. Chem., Int. Ed.* **2017**, *56*, 2909.
[87] X. Wang, J. Zhou, W. Tang, *Energy Storage Mater.* **2021**, *36*, 1.
[88] M. Zhu, L. Zhao, Q. Ran, Y. Zhang, R. Peng, G. Lu, X. Jia, D. Chao, C. Wang, *Adv. Sci.* **2022**, *9*, 2103896.
[89] J. Yu, J. Li, Z. Y. Leong, D. Li, J. Lu, Q. Wang, H. Y. Yang, *Mater. Today Energy* **2021**, *22*, 100872.
[90] C. Strietzel, M. Sterby, H. Huang, M. Strømme, R. Emanuelsson, M. Sjödin, *Angew. Chem., Int. Ed.* **2020**, *59*, 9631.
[91] W. Han, M. Li, Y. Ma, J. Yang, *Electrochim. Acta* **2022**, *403*, 139550.
[92] M. Shi, R. Wang, L. Li, N. Chen, P. Xiao, C. Yan, X. Yan, *Adv. Funct. Mater.* **2023**, *33*, 2209777.
[93] K. C. S. Lakshmi, B. Vedhanarayanan, H.-Y. Cheng, X. Ji, H.-H. Shen, T.-W. Lin, *J. Colloid Interface Sci.* **2022**, *619*, 123.
[94] Y. Dai, X. Yan, J. Zhang, C. Wu, Q. Guo, J. Luo, M. Hu, J. Yang, *Electrochim. Acta* **2023**, *442*, 141870.
[95] D. Shen, A. M. Rao, J. Zhou, B. Lu, *Angew. Chem., Int. Ed.* **2022**, *134*, e202201972.
[96] T. Sun, H. Du, S. Zheng, J. Shi, X. Yuan, L. Li, Z. Tao, *Small Methods* **2021**, *5*, 2100367.
[97] T. Sun, H. Du, S. Zheng, J. Shi, Z. Tao, *Adv. Funct. Mater.* **2021**, *31*, 2010127.
[98] Z. Lin, H.-Y. Shi, L. Lin, X. Yang, W. Wu, X. Sun, *Nat. Commun.* **2021**, *12*, 4424.
[99] L. Lin, Z. Lin, J. Zhu, K. Wang, W. Wu, T. Qiu, X. Sun, *Energy Environ. Sci.* **2023**, *16*, 89.
[100] M. Li, J. Liu, Y. Li, G. Xing, X. Yu, C. Peng, L. Chen, *CCS Chemistry* **2021**, *3*, 696.
[101] Z. Song, L. Miao, H. Duan, L. Ruhlmann, Y. Lv, D. Zhu, L. Li, L. Gan, M. Liu, *Angew. Chem., Int. Ed.* **2022**, *61*, e202208821.
[102] G. Zhao, X. Yan, Y. Dai, J. Xiong, Q. Zhao, X. Wang, H. Yu, J. Gao, N. Zhang, M. Hu, J. Yang, *Small* **2023**, *20*, 2306071.
[103] Y. Ma, Y. Wei, W. Han, Y. Tong, Aj. Song, J. Zhang, H. Li, X. Li, J. Yang, *Angew. Chem., Int. Ed.* **2023**, *62*, e202314259.
[104] Z. Tie, L. Liu, S. Deng, D. Zhao, Z. Niu, *Angew. Chem., Int. Ed.* **2020**, *132*, 4950.
[105] J. He, Y. Zhao, C. Yan, R. Jing, R. Wang, M. Shi, *Chem. Eng. J.* **2023**, *470*, 144204.
[106] R. Wang, L. Ke, H. Wang, Y. Tao, Y. Cui, P. Zhang, M. Shi, X. Yan, *Chinese Chem. Lett.* **2024**, 109920.
[107] Q. Sun, T. Sun, J. Du, K. Li, H. Xie, G. Huang, X. Zhang, *Adv. Mater.* **2023**, *35*, 2301088.

© 2024 The Author(s). Advanced Functional Materials published by Wiley-VCH GmbH

RIGHTSLINK

16163028, 2024, 40, Downloaded from https://onlinelibrary.wiley.com/doi/10.1002/adfm.202405401 by Karlsruher Institut F., Wiley Online Library on [05/11/2024]. See the Terms and Conditions (https://onlinelibrary.wiley.com/terms-and-conditions) on Wiley Online Library for rules of use; OA articles are governed by the applicable Creative Commons License

[108] M. Wang, G. Wang, C. Naisa, Y. Fu, S. M. Gali, S. Paasch, M. Wang, H. Wittkaemper, C. Papp, E. Brunner, S. Zhou, D. Beljonne, H.-P. Steinrück, R. Dong, X. Feng, *Angew. Chem., Int. Ed.* **2023**, *62*, e202310937.
[109] T. Sun, Q. Nian, X. Ren, Z. Tao, *Joule* **2023**, *7*, 2700.
[110] M. Naguib, M. Kurtoglu, V. Presser, J. Lu, J. Niu, M. Heon, L. Hultman, Y. Gogotsi, M. W. Barsoum, *Adv. Mater.* **2011**, *23*, 4248.
[111] M. R. Lukatskaya, S. Kota, Z. Lin, M.-Q. Zhao, N. Shpigel, M. D. Levi, J. Halim, P.-L. Taberna, M. W. Barsoum, P. Simon, *Nat. Energy* **2017**, *2*, 1.
[112] M. R. Lukatskaya, O. Mashtalir, C. E. Ren, Y. Dall'Agnese, P. Rozier, P. L. Taberna, M. Naguib, P. Simon, M. W. Barsoum, Y. Gogotsi, *Science* **2013**, *341*, 1502.
[113] X. Mu, D. Wang, F. Du, G. Chen, C. Wang, Y. Wei, Y. Gogotsi, Y. Gao, Y. Dall'Agnese, *Adv. Funct. Mater.* **2019**, *29*, 1902953.
[114] S. Liu, S. Jin, T. Jiang, M. Sajid, J. Xu, K. Zhang, Y. Fan, Q. Peng, X. Zheng, Z. Xie, *Nano Lett.* **2023**, *23*, 9664.
[115] M. Jiang, C. Fu, P. Meng, J. Ren, J. Wang, J. Bu, A. Dong, J. Zhang, W. Xiao, B. Sun, *Adv. Mater.* **2022**, *34*, 2102026.
[116] S. Wang, X. Zhao, X. Yan, Z. Xiao, C. Liu, Y. Zhang, X. Yang, *Angew. Chem., Int. Ed.* **2019**, *131*, 211.
[117] Y. Zou, T. Liu, Q. Du, Y. Li, H. Yi, X. Zhou, Z. Li, L. Gao, L. Zhang, X. Liang, *Nat. Commun.* **2021**, *12*, 170.
[118] F. Endres, G. Schwitzgebel, *J. Electroanal. Chem.* **1996**, *415*, 23.
[119] B. Yang, T. Qin, Y. Du, Y. Zhang, J. Wang, T. Chen, M. Ge, D. Bin, C. Ge, H. Lu, *ChemComm* **2022**, *58*, 1550.
[120] B. Gavriel, G. Bergman, M. Turgeman, A. Nimkar, Y. Elias, M. D. Levi, D. Sharon, N. Shpigel, D. Aurbach, *Mater. Today Energy* **2023**, *31*, 101189.
[121] W. Sun, Z. Xu, C. Qiao, B. Lv, L. Gai, X. Ji, H. Jiang, L. Liu, *Adv. Sci.* **2022**, *9*, 2201679.
[122] T. Akiyama, *Chem. Rev.* **2007**, *107*, 5744.
[123] H. Wang, R. Emanuelsson, C. Karlsson, P. Jannasch, M. Strømme, M. Sjodin, *ACS Appl. Mater. Interfaces* **2021**, *13*, 19099.
[124] W. B. Jensen, *Chem. Rev.* **1978**, *78*, 1.
[125] Z. Ma, X. Shi, S. Nishimura, S. Ko, M. Okubo, A. Yamada, *Adv. Mater.* **2022**, *34*, 2203335.
[126] N. Ma, S. Kosasang, A. Yoshida, S. Horike, *Chem. Sci.* **2021**, *12*, 5818.
[127] O. Wichterle, D. Lim, *Nature* **1960**, *185*, 117.
[128] M. Bahram, N. Mohseni, M. Moghtader, in *Emerging Concepts in Analysis and Applications of Hydrogels*, IntechOpen, Croatia **2016**.
[129] H. Dong, L.-L. Wang, Z.-R. Feng, J. Song, Q. Qiao, Y.-P. Wu, X.-M. Ren, *J. Mater. Chem. C* **2023**, *11*, 13113.
[130] L. M. Blinov, *Structure and Properties of Liquid Crystals*, Springer Science & Business Media, Berlin **2010**.
[131] Z. Guo, T. Wang, H. Wei, Y. Long, C. Yang, D. Wang, J. Lang, K. Huang, N. Hussain, C. Song, *Angew. Chem., Int. Ed.* **2019**, *58*, 12569.
[132] Z. Su, J. Chen, J. Stansby, C. Jia, T. Zhao, J. Tang, Y. Fang, A. Rawal, J. Ho, C. Zhao, *Small* **2022**, *18*, 2201449.
[133] W. A. Donald, R. D. Leib, M. Demireva, J. T. O'Brien, J. S. Prell, E. R. Williams, *J. Am. Chem. Soc.* **2009**, *131*, 13328.
[134] Y. Sugimoto, *Science* **2022**, *377*, 264.
[135] D. H. Lee, H. Kang, *J. Phys. Chem. B* **2021**, *125*, 8270.
[136] Z. Zhu, W. Wang, Y. Yin, Y. Meng, Z. Liu, T. Jiang, Q. Peng, J. Sun, W. Chen, *J. Am. Chem. Soc.* **2021**, *143*, 20302.
[137] C. Deng, X. Li, R. Chen, K. Ye, J. Lipton, S. A. Maclean, H. Wang, A. D. Taylor, G.-M. Weng, *Energy Storage Mater.* **2023**, *60*, 102820.
[138] M. C. Schulze, N. R. Neale, *ACS Energy Lett.* **2021**, *6*, 1082.
[139] Z. Tie, S. Deng, H. Cao, M. Yao, Z. Niu, J. Chen, *Angew. Chem., Int. Ed.* **2022**, *61*, e202115180.
[140] G. Dai, Y. He, Z. Niu, P. He, C. Zhang, Y. Zhao, X. Zhang, H. Zhou, *Angew. Chem., Int. Ed.* **2019**, *58*, 9902.
[141] N. Christudas Dargily, R. Thimmappa, Z. Manzoor Bhat, M. C. Devendrachari, A. R. Kottaichamy, M. Gautam, S. P. Shafi, M. O. Thotiyl, *J. Phys. Chem. Lett.* **2018**, *9*, 2492.
[142] Z. Pan, X. Liu, J. Yang, X. Li, Z. Liu, X. J. Loh, J. Wang, *Adv. Energy Mater.* **2021**, *11*, 2100608.
[143] Z. Yu, Q. Wang, Y. Li, F. Zhang, X. Ma, X. Zhang, Y. Wang, J. Huang, Y. Xia, *Joule* **2024**, *8*, 1063.
[144] H. Xu, W. Yang, M. Li, H. Liu, S. Gong, F. Zhao, C. Li, J. Qi, H. Wang, W. Peng, J. Liu, *Small* **2024**, *20*, 2310972.
[145] H. Yang, Y. Qiao, Z. Chang, H. Deng, P. He, H. Zhou, *Adv. Mater.* **2020**, *32*, 2004240.
[146] T. Liu, H. Wang, C. Lei, Y. Mao, H. Wang, X. He, X. Liang, *Energy Storage Mater.* **2022**, *53*, 544.
[147] H. Ma, D. Kong, Y. Xu, X. Xie, Y. Tao, Z. Xiao, W. Lv, H. D. Jang, J. Huang, Q. Yang, *Small* **2017**, *13*, 1701026.
[148] X. Guo, J. Zhou, C. Bai, X. Li, G. Fang, S. Liang, *Mater. Today Energy* **2020**, *16*, 100396.
[149] X. Yan, F. Wang, X. Su, J. Ren, M. Qi, P. Bao, W. Chen, C. Peng, L. Chen, *Adv. Mater.* **2023**, *35*, 2305037.
[150] W. Song, J. Zhang, C. Wen, H. Lu, C. Han, L. Xu, L. Mai, *J. Am. Chem. Soc.* **2024**, *146*, 4762.
[151] Y. Zhang, L. Tao, C. Xie, D. Wang, Y. Zou, R. Chen, Y. Wang, C. Jia, S. Wang, *Adv. Mater.* **2020**, *32*, 1905923.
[152] W. Lee, S. Muhammad, C. Sergey, H. Lee, J. Yoon, Y. Kang, W. Yoon, *Angew. Chem., Int. Ed.* **2020**, *59*, 2578.
[153] P. Zhai, L. Liu, X. Gu, T. Wang, Y. Gong, *Adv. Energy Mater.* **2020**, *10*, 2001257.
[154] X. Wang, Q. Weng, Y. Yang, Y. Bando, D. Golberg, *Chem. Soc. Rev.* **2016**, *45*, 4042.
[155] Y. Sun, C. Zhan, P. R. C. Kent, D. Jiang, *J. Phys. Chem. C* **2021**, *125*, 11508.
[156] Y. Shan, Y. He, N. Yang, X. Zhu, H. Liu, H. Jiang, C. Li, *Small* **2022**, *18*, 2105927.
[157] Y. Ding, C. Zhang, L. Zhang, Y. Zhou, G. Yu, *Chem. Soc. Rev.* **2018**, *47*, 69.
[158] N. Lu, Z. Zhang, Y. Wang, H.-B. Li, S. Qiao, B. Zhao, Q. He, S. Lu, C. Li, Y. Wu, *Nat. Energy* **2022**, *7*, 1208.
[159] F. Wang, L. Suo, Y. Liang, C. Yang, F. Han, T. Gao, W. Sun, C. Wang, *Adv. Energy Mater.* **2017**, *7*, 1600922.
[160] M. Shao, J. Deng, F. Zhong, Y. Cao, X. Ai, J. Qian, H. Yang, *Energy Storage Mater.* **2019**, *18*, 92.
[161] L. Jiang, Y. Lu, C. Zhao, L. Liu, J. Zhang, Q. Zhang, X. Shen, J. Zhao, X. Yu, H. Li, *Nat. Energy* **2019**, *4*, 495.
[162] C. Xia, J. Guo, P. Li, X. Zhang, H. N. Alshareef, *Angew. Chem., Int. Ed.* **2018**, *130*, 4007.
[163] L. Zhang, L. Chen, X. Zhou, Z. Liu, *Adv. Energy Mater.* **2015**, *5*, 1400930.
[164] Z. Qin, Y. Song, Y. Liu, X.-X. Liu, *Energy Storage Mater.* **2022**, *53*, 569.
[165] H. Lin, F. Zhou, C.-P. Liu, V. Ozoliņš, *J. Mater. Chem. A* **2014**, *2*, 12280.
[166] H. Guo, M. Elmanzalawy, P. Sivakumar, S. Fleischmann, *Energy Environ. Sci.* **2024**, *17*, 2100.
[167] H. Liu, X. Cai, X. Zhi, S. Di, B. Zhai, H. Li, S. Wang, L. Li, *Nanomicro Lett.* **2023**, *15*, 24.
[168] Z. Zhu, Z. Liu, Y. Yin, Y. Yuan, Y. Meng, T. Jiang, Q. Peng, W. Wang, W. Chen, *Nat. Commun.* **2022**, *13*, 2805.

© 2024 The Author(s). Advanced Functional Materials published by Wiley-VCH GmbH

RIGHTSLINK

16163028, 2024, 40, Downloaded from https://onlinelibrary.wiley.com/doi/10.1002/adfm.202405401 by Karlsruher Institut F., Wiley Online Library on [05/11/2024]. See the Terms and Conditions (https://onlinelibrary.wiley.com/terms-and-conditions) on Wiley Online Library for rules of use; OA articles are governed by the applicable Creative Commons License

Sicheng Wu received his B.Sc. (Honors) degree from the University of New South Wales (UNSW) in 2019. He is currently a Ph.D. candidate under the supervision of Prof. Chuan Zhao at UNSW. His research interests focus on electrode and electrolyte design for aqueous batteries and supercapacitors, as well as correlated mechanism study via electrochemical and physiochemical characterization techniques.

Haocheng Guo is now a research scientist at Helmholtz Institut Ulm, affiliated with Karlsruher Institut für Technologie. He earned his PhD from the University of New South Wales in Prof. Zhao's group. His research focuses on oxide-based electrodes for energy storage, where he has gained experience in various electrochemical and physiochemical characterization tehcniques. He is interested in material and chemistry for a range of energy applications, including high-energy cathode for lithium-ion batteries, and post-lithium energy storage techniques based on ions of H^+, Zn^{2+}, and Mg^{2+}, etc.

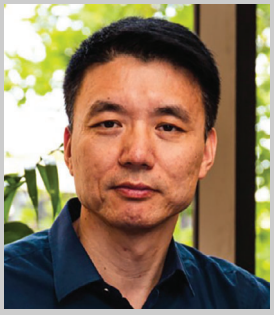

Chuan Zhao is a Professor at the School of Chemistry at the University of New South Wales (UNSW), Sydney. He is currently the Deputy Director of the Australian Research Council (ARC) Training Centre for the Global Hydrogen Economy, and the Deputy Research Chair and Flagship Program Director of the ARC Centre of Excellence on Green Electrochemical Transformation of Carbon Dioxide. He is interested in discovering novel electrochemical methodologies and nanomaterials for energy applications, including water splitting, hydrogen fuel cells, CO_2 & N_2 reduction, batteries, and sensors.

© 2024 The Author(s). Advanced Functional Materials published by Wiley-VCH GmbH

RIGHTSLINK

16163028, 2024, 40, Downloaded from https://onlinelibrary.wiley.com/doi/10.1002/adfm.202405401 by Karlsruher Institut F., Wiley Online Library on [05/11/2024]. See the Terms and Conditions (https://onlinelibrary.wiley.com/terms-and-conditions) on Wiley Online Library for rules of use; OA articles are governed by the applicable Creative Commons License